

ELECTRON PARAMAGNETIC RESONANCE INVESTIGATION OF
SEMIQUINONE INTERMEDIATE IN MITOCHONDRIAL
CYTOCHROME *BC₁* COMPLEX

by

PREETHI R. VENNAM

MICHAEL K. BOWMAN, COMMITTEE CHAIR
SHANE STREET
CAROLYN J CASSADY
LAURA BUSENLEHNER
DAVID M. KRAMER
A DISSERTATION

Submitted in partial fulfillment of the requirements
for the degree of Doctor of Philosophy
in the Department of Chemistry
in the Graduate School of
The University of Alabama

TUSCALOOSA, ALABAMA

2012

Copyright Preethi Reddy Vennam 2012
ALL RIGHTS RESERVED

ABSTRACT

The Rieske/cytochrome *b* complexes, also known as cytochrome *bc* complexes, catalyze a unique oxidant-induced reduction reaction at their quinol oxidase (Q_o) sites, in which substrate hydroquinone reduces two distinct electron transfer chains, one leading to a series of high-potential electron carriers, the second to low-potential cytochrome *b*. This reaction is a critical step in energy storage by the Q-cycle. The semiquinone intermediate in this reaction can also reduce O_2 to produce deleterious superoxide. It is yet unknown how the enzyme controls this reaction, though numerous models have been proposed. In previous work we were able to trap a Q-cycle semiquinone anion intermediate, termed SQ_o in bacterial cyt *bc_L* by rapid freeze-quenching. In this work, we apply pulsed EPR techniques to determine the location of SQ_o in mitochondrial complex and that mitochondrial SQ_o has highly unusual properties. In contrast with previous semiquinone intermediates, SQ_o is not thermodynamically stabilized, or even destabilized with respect to solution. It is localized in the Q_o pocket at a niche, which is distinct from previously described inhibitor-binding sites, but is sufficiently close to cytochrome *b_L* to allow rapid electron transfer. Both the location of the binding sites and EPR analysis show that SQ_o is not stabilized by hydrogen bonds to proteins. These results indicate that the formation of SQ_o involves “stripping” of both substrate protons during the initial oxidation to the high potential chain, as well as conformational changes of both semiquinone species and Q_o site proteins components. The resulting charged radical is kinetically trapped, rather than thermodynamically stabilized (as in most enzymatic semiquinone species), maintaining redox

energy to drive electron transfer to cytochrome b_L , while minimizing certain Q-cycle bypass reactions including oxidation of pre-reduced cytochrome b and reduction of O_2 .

DEDICATION

This work is dedicated my family and close friends who stood by me throughout the time taken to complete this masterpiece. My parents, Raji Reddy and Renuka Vennam, my sister and brother-in-law Swathi and Veplav Chintala and my extended family and friends, have always provided me with the encouragement and support one needs to become successful in all facets of life.

LIST OF ABBREVIATIONS AND SYMBOLS

β_e	Bohr magneton for electron
β_n	Bohr magneton for nucleus
A	Hyperfine coupling value
AA	Antimycin-A
CoQ_{10}	Coenzyme Q10 or
cyt	cytochrome
Fe_2S_2	Iron-Sulfur cluster
g	gyromagnetic ratio
g_e	gyromagnetic ration of free electron
g_n	gyromagnetic ration of nucleus
ISP	Iron-sulfur protein
$MNQH_2$	Menaquinol
pmf	proton motive force
PQH_2	Plastoquinol
PRE	Paramagnetic Relaxation Enhancement
Q	Quinone
QH_2	Quinol
$Q_i pocket$	Quinone reduction pocket/site
$Q_o pocket$	Quinol oxidation pocket/site
SO	Superoxide

SQ	Semiquinone
SQ_o	Semiquinone at Q_o pocket
$stig$	Stigmatellin
T_1	Longitudinal relaxation time
T_2/T_M	Transverse relaxation time

ACKNOWLEDGMENTS

First and foremost I would like to thank my research advisor Dr. Bowman, without whom I would not be able to finish this work. He has been very helpful and patient in not only teaching me the EPR theory and instrumentation, but also training as a competent scientist and critical thinker. He has always provided me with helpful tips and insights whenever I reached a stalemate in my research. I appreciate everything you have done for me, thank you Dr. Bowman.

Next I would like to thank our collaborator Dr. Kramer's lab both at WSU and MSU. I would like to thank Dr. Qiang Xu from WSU for helping me with the freeze-quench sample preparation and Dr. Nick Fisher from MSU for his insight in many things regarding *cyt bc₁* from preparation to modeling. I appreciate the assistance and camaraderie of all my labmates, especially Dr. Krzyaniak, a post-doc in our lab for helping me with the simulation program for T2 data analysis. Thank you Matt you have been a pleasure to work with. I would like to thank all my committee members for their guidance and patience.

I would like to thank my family and friends I made during my under-graduate and graduate studies, who have shaped me both personally and professionally. They all have cheered me up in my darkest times with their love and friendship.

I would also like to thank University of Alabama and National Institute of Health for providing the funds that supported me and my research.

CONTENTS

ABSTRACT.....	ii
DEDICATION.....	iv
LIST OF ABBREVIATIONS AND SYMBOLS.....	v
ACKNOWLEDGMENTS.....	vii
LIST OF TABLES.....	xii
LIST OF FIGURES.....	xiii
1. INTRODUCTION.....	1
1.1 Introduction.....	1
1.2 Background.....	2
1.2.1 The Q-cycle.....	3
1.2.2 Reiske ISP headgroup motion.....	6
1.2.3 Bypass reactions and SO production.....	7
1.3 Objective.....	11
2. PREPARATION OF SQ RADICAL INTERMEDIATE.....	15
2.1 EPR Sample preparation:.....	15
2.1.1 Extraction of cyt bc ₁ complex from <i>Saccharomyces cerevisiae</i> cells:.....	15
2.1.2 Extraction of cyt bc ₁ complex from <i>Rhodobacter capsulatus</i> cells:.....	17
2.1.3 Purification of cyt bc ₁ using ion-exchange chromatography:.....	19
2.1.4 Cyt bc ₁ concentration determination:.....	19
2.1.5 Preparation of Freeze-Quenched EPR Samples:.....	20

2.1.6	Preparation of UQ radicals in solution:	21
2.2	Preliminary EPR results:.....	22
3.	THEORY	24
3.1	The Hamiltonian Operator	24
3.1.1	Electron Zeeman Interaction.....	25
3.1.2	Nuclear Zeeman Interaction.....	28
3.1.4	Spin-Spin Coupling.....	32
3.2	Relaxation	34
3.2.1	Processes causing spin-lattice relaxation	35
3.2.2	Processes contributing to Transverse Relaxation	37
3.2.3	Dipolar relaxation enhancement	38
3.2.4	Methods of measuring distance by EPR	40
3.3	Experiments used	43
3.3.1	ESEEM experiments:.....	45
3.3.2	ENDOR experiments	49
4.	CHARACTERIZATION OF SQ INTERMEDIATE	55
4.1	EPR Experiments:.....	56
4.2	Theory:.....	57
4.3	Results:.....	59
4.3.1	CW-EPR	59
4.3.2	High field and pulsed EPR.....	60
4.3.3	Pulsed ENDOR	63
4.3.4	ESEEM	69

4.4 Discussion:	71
4.4.1 Nature of SQ ₀ and its interaction with protein:	71
5. DETERMINATION OF SQ LOCATION IN CYTOCHROME <i>BC₁</i>	74
5.1 Enhanced Spin Relaxation of SQ Generated at the Q ₀ Site.	75
5.2 Analysis of T _M data	80
5.2.1 Sensitivity of T _M Dipole to distance:	82
5.3 Determination of the Location of SQ.	84
5.3.1 Determining distance between SQ and Hemes from EPR experiemnts	84
5.3.2 Molecular Modeling of the SQ Distance Constraints	88
5.4 Discussion:	89
5.4.1 SQ binding sites within Q ₀ .	89
5.4.2 Reactions and Energetics:	93
5.5 Conclusions:	95
6. SUMMARY	97
6.1 Summary	97
6.2 Future work	98
REFERENCES	100
APPENDIX	112
Appendix A.1	112
Appendix A.2	117
Appendix A.3	119
Appendix A.4	123
Appendix A.5	124

MakeDecay function..... 124

LIST OF TABLES

Table 1. G-Values	63
Table 2. Hyperfine Coupling Values	68

LIST OF FIGURES

Figure 1.1 The q-cycle in cyt bc ₁ complex.	4
Figure 1.2 Bypass reactions.	8
Figure 1.3 Schematic of the possible reactions to oxidize quinol.....	13
Figure 2.1 Photolysis scheme making quinone radical anion in cyclohexanol.	21
Figure 2.2 X-band EPR of SQ _o and SQ in solution.	23
Figure 3.1 Electron Zeeman interactions.	26
Figure 3.2 Nuclear Zeeman interaction.	29
Figure 3.3 Hyperfine interaction for S=1/2 and I=1/2.....	29
Figure 3.4 ESEEM pulse sequence.....	46
Figure 3.5 ENDOR..	50
Figure 3.6 Mims ENDOR pulse sequence.....	54
Figure 4.1 X-Band EPR of SQ.....	59
Figure 4.2 HF-EPR of SQ.....	61
Figure 4.3 ENDOR of UQ Radical anion.	65
Figure 4.4 ENDOR of UQ neutral radical..	66
Figure 4.5 ENDOR of SQ _o in protein.	67
Figure 4.6 Four pulse ESEEM spectra.....	69
Figure 4.7 Two-pulse ESEEM spectra of SQ _o	70
Figure 5.1 T ₁ relaxation of SQ radical anion and SQ _o	76
Figure 5.2 T ₂ relaxation enhancement of SQ _o and SQ in solution.....	79

Figure 5.3 Effect of temperature and T_1 on T_2	83
Figure 5.4 Distance constraints of SQ_0 obtained from T_2 data analysis.	87
Figure 5.5 Volumetric representation of the SQ binding niches within yeast cytochrome bc_1	90
Figure 5.6 Detail of sidechain interactions between yeast cyt b (3CX5.PDB) and SQ site I.	91
Figure 5.7 Detail of sidechain interactions between yeast cyt b (3CX5.PDB) and SQ site II.	92

CHAPTER 1

INTRODUCTION

1.1 Introduction

The Rieske/*b* and related complexes, e.g., cytochrome (cyt) *bc*₁ complex, also known as ubiquinol: cyt *c* oxidoreductase, in mitochondria and related cyt *b*₆*f* in chloroplasts and other *bc*-type complexes in many bacteria are essential components of the electron transport chain in respiratory and photosynthetic systems. These complexes aid in generating an electrochemical gradient of protons across membrane, also called as proton motive force (pmf). The pmf is essential for synthesis of ATP and other bio-energetic processes. These complexes translocate protons across the membrane by oxidizing a range of different quinol (QH₂) molecules: ubiquinol (UQH₂) in mitochondria and many bacteria, plastoquinol (PQH₂) in chloroplasts and cyanobacteria, and menaquinol (MNQH₂) in many bacteria, to the corresponding quinone (Q), and they reduce a range of soluble electron carriers, including cyt *c* in mitochondria, plastocyanin or cyt *c*₆ in chloroplasts and cyanobacteria, and high-potential iron-sulfur proteins in certain bacteria. Cyt *bc*₁ plays an important role in metabolic and energetic pathways both in humans and wide range of human pathogens (1-4). In addition to the generation of pmf, cyt *bc*₁ can also form superoxide (SO) as a bypass reaction in case of cyt *bc*₁ malfunction (5). SO production within a cell can lead to a cascade of reactions, causing lipid peroxidation and protein damage (6, 7) or inappropriate cellular signaling (8). Excess SO will cause oxidative stress and eventually cell death, and has long been suggested as a factor in many pathophysiological

processes. Many diseases and degradative processes affecting humans can be directly correlated to mitochondrial dysfunction. The process of aging is integrally linked to the oxidative degradation of mitochondria and *cyt bc₁* dysfunction (9) and is indicted in certain diseases like diabetes, heart disease and cancer (10, 11). There is a need to understand the full range of reactions possible for *cyt bc₁* complex in both normal physiological and diseased conditions. There is a need to understand how *cyt bc₁* complex maintains the balance between driving pmf and SO formation in normal physiological condition and how is it disrupted in diseased conditions.

1.2 Background

The *cyt bc₁* and *bc*-type enzymes are dimeric, integral membrane proteins. Each monomer consists of anywhere from three subunits in some prokaryotes to eleven subunits in mitochondria. Each monomer of the active complex consists of three essential catalytic subunits: *cyt b*; the Rieske iron-sulfur protein (ISP); and *cyt c₁*. The *cyt bc₁* complex transports electrons through two distinct electron transport chains involving four major redox-active metal centers. The ‘low-potential chain’ consists of *cyt b* with its two hemes, heme *b_H* and heme *b_L* with relatively higher and lower redox potentials, bound within the *cyt b* protein. The ‘high-potential chain’ consists of a ‘Rieske’ iron-sulfur cluster (2Fe2S) in the Rieske ISP, and another relatively high-potential carrier: *cyt c₁* in the *cyt bc₁* complex and an assortment of other carriers in complexes from distantly-related bacteria. The *cyt bc₁* complex has two different substrate (Q/QH₂) binding sites. One is in the positive side (p-side) of the membrane and termed as ‘Q_o site’ or ‘Q_o pocket’ and the other is in negative side (n-side) of the membrane, termed as ‘Q_i site’. The Q_o pocket is located at the interface between heme *b_L* and ISP and during normal

turnover oxidizes QH_2 to Q. The other site, Q_i site on the n-side of the membrane in turn reduces Q to QH_2 , which can enter in to a subsequent cycle.

Crystal structures provide valuable information about substrate binding and are consistent with the general outlines of the Q-cycle mechanism (discussed later in this chapter). Though there are crystal structures of *cyt bc₁* published with and without various inhibitors, there is none with bound Q/ QH_2 in the Q_o pocket (12-18). Crystal structures also showed the ISP in different conformations indicating large-scale movement of the ISP head-group in the complex. However, crystal structures represent the stable states along the catalytic cycle and do not show the reactive intermediates that are vital for understanding the detailed reactions. Though the crystal structures provide an invaluable structural context in which to formulate and test mechanistic hypotheses, the details of how substrate bind, how electrons are transferred and the nature of intermediates and transition states involving the Q_o site can only be determined through biophysical measurements.

1.2.1 *The Q-cycle*

Electron flow through the *cyt bc₁* and *b₆f* complexes occurs by the ‘Q-cycle’ mechanism proposed by Peter Mitchell in 1976 and modified several times (19-22). The important structural and mechanistic features of these complexes that allow them to perform the Q-cycle are still controversial. Cape et al. have recently grouped these highly-complex Q-cycle working models to a few recurring motifs to simplify them (23). I will use one of the simplified, yet still complicated models to explain the *cyt bc₁* functioning and will refer to it as the modified Q-cycle from now.

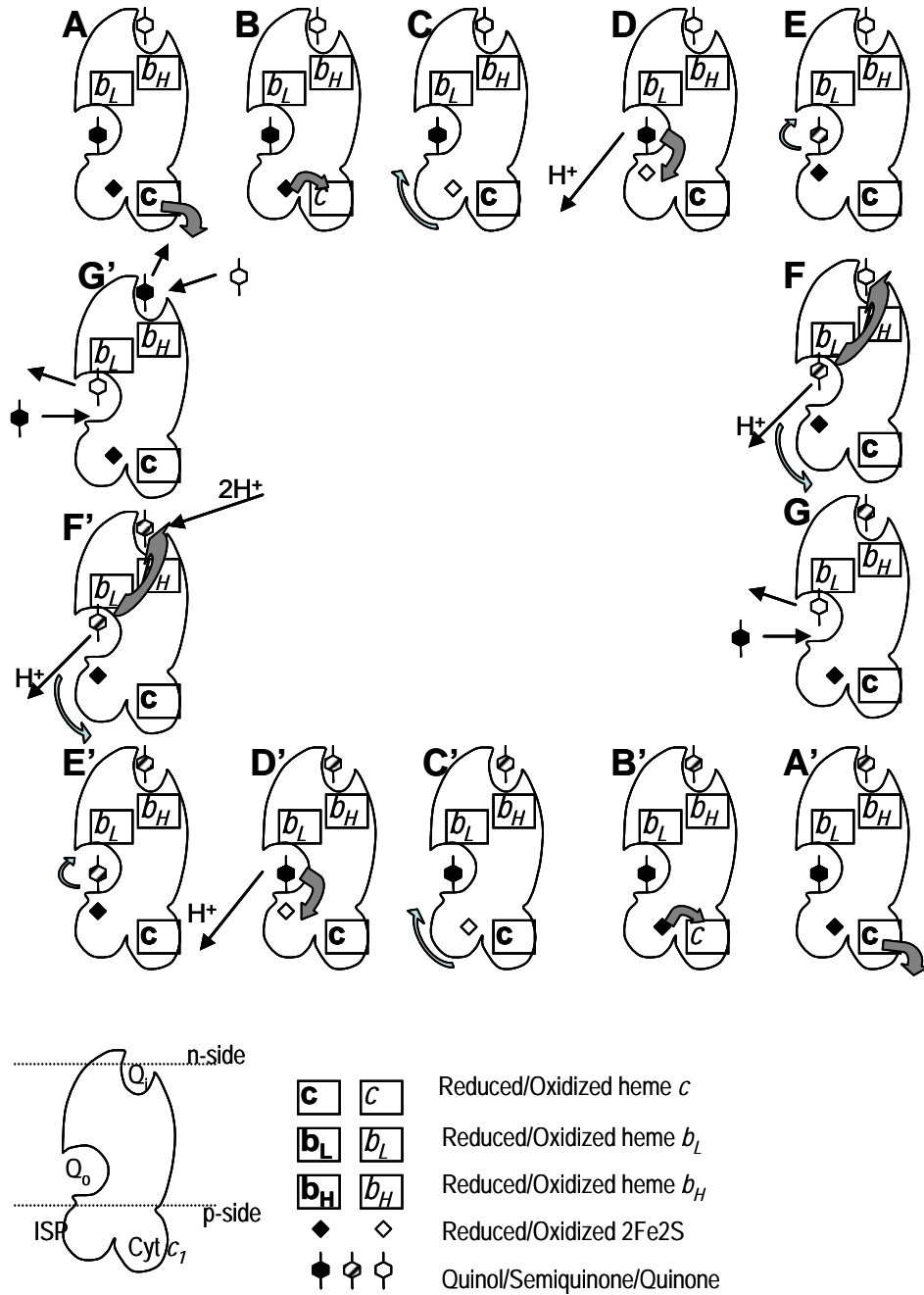


Figure 1.1 The Q-cycle in cyt *bc*₁ complex. The lower left of the figure shows a cyt *bc*₁ in schematic form with the quinone binding sites, the Rieske ISP and cyt *c*₁ labeled. The surface of the membrane is indicated by the two dashed lines. The substrates and cofactors are identified along with their redox states by the symbols at the bottom. The different states of the complex in its catalytic cycle are represented by the individual images with the redox states of the various cofactors. The different arrows show the electron and molecular motions that advance each state to its subsequent state.

The modified Q-cycle involves a bifurcated electron transport chain involving both a high-potential chain and a low-potential chain. For a better understanding of the Q-cycle mechanism, the reader is referred to figure 1.1 and can follow the different stages in the figure, as described in the text. To understand the general outlines of the modified Q-cycle, we can consider it starting with the binding of QH₂ in the Q_o pocket of cyt *bc*₁ complex with *b* hemes of the low-potential chain oxidized and the ISP and cyt *c*₁ of the high-potential chain reduced (A of figure 1.1). The cyt *c*₁ is oxidized by transferring an electron to a soluble cyt *c*. The oxidized cyt *c*₁ accepts an electron from the reduced Fe₂S₂ of ISP (B) and oxidizes Fe₂S₂ (C). The head group of ISP pivots by ~65° to bring the Fe₂S₂ group near the Q_o pocket (D).

The QH₂ bound in the distal niche, i.e., distant from heme *b*_L of the Q_o pocket transfers an electron to the Fe₂S₂ cluster and one proton across the membrane to the p-side resulting in the formation of a semiquinone (SQ) species (E). The SQ in Q_o pocket quickly moves to the ‘proximal’ niche, i.e., near heme *b*_L (F). It is still controversial whether this ‘movement’ is a physical relocation of a single SQ in the Q_o pocket or some sort of electronic transfer between two quinone species packed in to the Q_o pocket (19, 24). The ISP head group pivots back towards the cyt *c*₁ (F-G) and the unstable SQ species donates the electron to the reduced heme *b*_L of the low-potential chain, along with transferring a proton to the p-side of the membrane, leaving a Q at the Q_o pocket (G). The heme *b*_L transfers an electron to heme *b*_H, which in turn transfers the electron to a Q in the Q_i site, leaving a SQ species (G). The Q at the Q_o pocket is replaced by QH₂ to complete the first sub-cycle.

Similar reactions will occur in the second sub-cycle: oxidation of ISP cluster by transferring an electron to cyt *c*₁ (A’), formation of SQ in the Q_o pocket by transferring an

electron to the oxidized ISP (B'-E') followed by another electron transfer through the low-potential chain to the SQ at the Q_i site along with uptake of two protons from the n-side of the membrane to form QH₂ (F'-G'). At the end of second sub-cycle, the QH₂ in the Q_i site is replaced by the Q and the Q at the Q_o pocket is replaced by QH₂ to start another cycle of electron transfer. The result of the full catalytic cycle is the oxidation of two QH₂ molecules to Q at the Q_o pocket along with translocation of four protons across the membrane to the p-side. On the other side of the cyt *bc₁* complex, one Q molecule is reduced to QH₂ at the Q_i site by picking up two protons from the n-side of the membrane.

The unique feature of the Q-cycle is the 'bifurcated' electron flow through different pathways (20, 21, 25, 26). One electron from each quinol is transferred through the high-potential chain with a large thermodynamic driving force. The other electron transfers through the low-potential chain with very low thermodynamic driving force. This bifurcation enables the Q-cycle to transfer two protons per each electron transferred to the cyt *c* and other downstream enzymes. The bifurcation, in particular, is one of the major issues in the field. The ability to study the SQ trapped in the Q_o pocket would be of great help to understand the electron transport in cyt *bc₁*.

1.2.2 Reiske ISP headgroup motion

The cyt *bc₁* complexes have large conformational changes in the ISP during their catalytic cycles as inferred from crystal structures of a wide range of complexes (27, 28) including the recent cyt *b₆f* crystal structures (29, 30) and from electron paramagnetic resonance (EPR) studies of oriented, hydrated membranes in different physiologically relevant states (31-35). The effect of different inhibitors and mutations on the ISP was studied using EPR

techniques. Inhibitors such as stigmatellin (stig) block the QH₂ binding at the Q_o pocket, interact with the ISP and lock it in a single conformation in which the Fe₂S₂ cluster is near the Q_o pocket, and block the electron transport through high-potential chain. Another class of inhibitors that prevents the reduction of cyt *b* binds in the Q_o pocket in a different way, allowing the ISP headgroup to move, but blocking electron transport through the low-potential chain. Although cyt *b* and ISP reduction blockers bind in the Q_o pocket, they seem to interact with and be bound in different regions of the site. The cyt *b* reduction inhibitors bind near the heme *b_L*, occupying a niche in the Q_o pocket that is proximal to heme *b_L* and are called proximal niche inhibitors, and the ISP reduction inhibitors bind farther away and are called distal niche inhibitors. The distal niche inhibitors do not have any effect on the movement of the Fe₂S₂ head group of the ISP.

1.2.3 Bypass reactions and SO production

There are several alternative reactions to the Q-cycle with larger net driving forces, leading to short-circuiting ‘bypass’ reactions (36-39). These bypass reactions are thermodynamically more favorable but less efficient in driving the proton motive force, robbing the cell of ATP. The reactive intermediates in the Q_o site can have several fates besides the Q-cycle, including (i) reduction of the high-potential chain by both QH₂ electrons, either by direct oxidation of SQ_o or by relaying an electron from the reduced low-potential chain; (ii) SQ_o can escape from Q_o site, disproportionate to Q and QH₂; and (iii) SQ_o can react with cellular O₂ to form superoxide (SO). All these reactions decrease energy storage by decreasing proton translocation. Of all these bypass reactions SO production is more active and toxic to the cells (40).

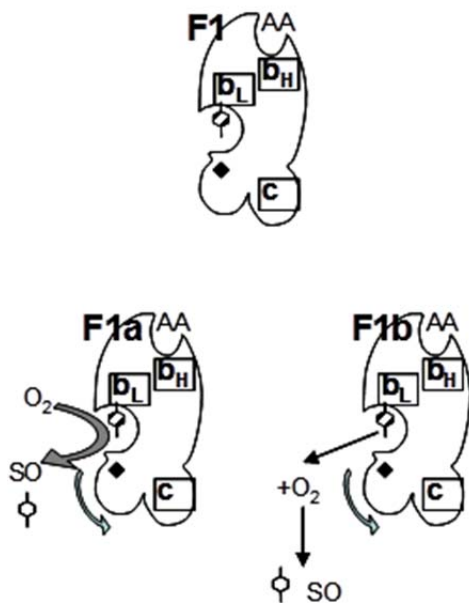


Figure 1.2 Bypass reactions. Two possible Q-cycle bypass reactions that could generate SQ

These bypass reactions will be more prominent when the Q-cycle is blocked one or the other way (figure 1.2). For example, production of SO is stimulated by the binding of inhibitors such as Antimycin-A (AA) at the Q_i site (38, 39). The inhibitor AA blocks the Q binding at the Q_i site and further the electron transport from heme b_H . The Q-cycle reactions will be normal for two turnovers of QH_2 at the Q_o pocket, but without

the oxidation of the low-potential chain, the cyt b hemes remain reduced. Subsequent QH_2 that bind at the Q_o pocket will be partially oxidized by the Fe_2S_2 of ISP to form SQ_o . The SQ_o cannot transfer the electron to the heme b , because both the hemes are reduced and cannot accept another electron. The unstable SQ_o will either react with the O_2 that enters the Q_o pocket and form a SO and Q; or the SQ_o will escape the enzyme and react with cellular O_2 to form SO and Q. In either case, more QH_2 will bind at the Q_o pocket and produce more SO and this process continues.

In the complex Q-cycle reactions there are many ways to induce SO production. One way is to inhibit the Q binding at the Q_i site as described above. Second way is by building backpressure from a large electrical potential across the membrane that prevents the electron transport in the low-potential chain (41, 42). Yet another way is the use of quinol analogues or

modified quinols that act as substrates but increase SO production (43). Mutations in the *cyt bc₁* complex can also shift the equilibrium towards SO production from Q-cycle (44, 45).

SO produced in mitochondria has long been suspected of contributing to ageing-related and other diseases. SO production within a cell can lead to a cascade of reactions, causing lipid peroxidation and protein damage or inappropriate cellular signaling even at low yields. Recent study by Loeb et al., showed that mutations in mitochondria including *cyt b* have led to decreased lifespan in plants and premature onset of ageing-related syndromes such as hair loss, curvature of the spine, osteoporosis and cardiac enlargement in animals (45-47). A causative connection between these features and the SO production has not been established yet.

Improved mechanistic understanding can improve human health through: new treatment to combat ageing processes; improved diagnosis and treatment of genetic diseases caused by *cyt bc₁*; and by the development of new antibiotics. An effort is made to understand the fundamental features universal to *cyt bc₁* complex in various kingdoms which could lead to specific drugs or antibiotics targeted to pathogens.

Forquer et al. (48) have shown that SO production and the Q-cycle share an identical or very similar transition states, suggesting that both processes likely involve the same intermediate. The “transient intermediate” observed might be SQ₀ that is rapidly consumed during normal turnover via oxidation by *cyt b_L* or by superoxide production during partially-inhibited turnover, and accumulated only when these pathways are blocked (39, 49). Of course, we cannot yet eliminate the possibility that the Q₀ site-generated SQ observed in this dissertation represents a later intermediate in the reaction pathway than the true O₂ reductant formed during uninhibited turnover (48). Cape et al. (50) have proposed that SO production by the *cyt bc₁* complex is

initiated upon SQ formation and occurs mainly within the Q_o pocket. The rate of SO production is thus likely controlled by two factors. First, the redox properties of the SQ/QH₂ couple will control the amount of SQ formed at the site, as demonstrated by the observation that substitution of UQH₂ by rhodoquinol transforms the *bc₁* into a “superoxide factory” (51). Second, the Q_o site also likely acts as a barrier to O₂ diffusion into the site, limiting the rate of SO production. In this case, changes in the permeability of O₂ into the Q_o site (i.e., its diffusion rate) should have large effects on the maximum rate of SO production, and we thus predict that some disease-related mutations of the *cyt bc₁* will affect the ability of the Q_o pocket to “shield” the reactive intermediates.

The SQ intermediate has been looked for during past 50 years but not found until recently and only in bacterial *cyt bc₁*, that use SQ during anaerobic photosynthesis where there is no O₂ to form SO. Early attempts to detect the postulated SQ_o intermediate failed to find one that was sensitive to Q_o site inhibitors (52) that block enzymatic activity. This missing link prevented understanding of the strict use of two electron transport chains and the proton pumping, which is widely thought to involve motions of SQ_o within Q_o and of the ISP subunit. Recent freeze-quench experiments (53, 54) used different strategies to trap a SQ produced in the Q_o site of *cyt bc₁* of *Rhodobacter capsulatus* based on specific inhibitors and mutations. Both blocked the low-potential chain so it could accept only 1-2 electrons, before leaving a SQ_o stranded. The *cyt bc₁* was mixed rapidly with QH₂ and frozen 7 ms later (53), long enough for 2-3 enzymatic turnovers to fill the low-potential chain and form SQ_o but not for SQ_o to react through bypass reactions (5, 55) or escape from Q_o . Electron paramagnetic resonance (EPR) analysis of the trapped SQ in these freeze-quenched samples showed it to be in or very near Q_o . Subsequently,

Zhang et al. (54) found consistent results in chromatophores of *R. capsulatus* after flash excitation of the photosynthetic reaction centers to oxidize cyt *bc₁* complex followed by freezing.

The trapped SQ can serve as a new spectroscopic probe of reactions and interactions in Q_o, but interpretation of such studies depends on where that SQ is finally trapped, while their relevance to human or even eukaryotic pathophysiology is complicated by the significant differences between bacterial cyt *bc₁* of *R. capsulatus* and mitochondrial cyt *bc₁* (56) . These considerations led us to apply rapid freeze-quench to mitochondrial cyt *bc₁* of *Saccharomyces cerevisiae* yeast and to locate the trapped SQ using paramagnetic relaxation enhancement (PRE), of the unpaired electron spin of the SQ by the cyt *b_L* and cyt *c₁* heme cofactors and to characterize the trapped SQ and its interaction with the environment using pulsed EPR techniques.

1.3 Objective

The specific aims of this study are (i) to trap the SQ intermediate in mitochondrial cyt *bc₁* in large enough amounts to be able to detect spectroscopically; (ii) to characterize the trapped SQ intermediate and its interactions with the protein and the surroundings; (iii) to determine the physical location of the SQ intermediate in the protein and (iv) to identify the substrate/quinol binding site in the protein, how the SQ binds and where it binds.

The SQ has proven to be elusive despite many attempts over the years to observe it. Two factors have made it difficult. Kinetic and thermodynamic measurements of the Q-cycle indicate that the formation of SQ at or near the transition state in the bifurcation reaction has a large E_{act} of roughly 60 kJ/mole. Thus, under most experimental conditions there is little if any SQ present

to detect. However, the SQ ought to be observable if it is kept from being consumed by both Q-cycle and bypass reactions.

In this work I describe the trapping and characterization of the SQ intermediate of the Q-cycle in mitochondrial *cyt bc₁*. Rapid freeze-quench technique was used to trap the SQ intermediate at the Q_o pocket. AA, a Q_i site inhibitor, was used to block the electron flow through the low-potential chain from heme *b* to Q at the Q_i site. The Q-cycle continues normally for 2 cycles, reducing both hemes in the low-potential chain. In the third cycle, the QH₂ bound at the Q_o site will be oxidized to SQ intermediate by the Fe₂S₂ of ISP, the SQ cannot transfer electron to heme *b*, leaving the SQ in protein. This favors the SO production, but a strict anaerobic environment was maintained, preventing the SO production. The mixture was frozen rapidly enough to avoid all other bypass reactions and leaving SQ in protein.

The trapped SQ intermediate was identified using CW-EPR spectroscopy. The substrate QH₂ could follow any of the reactions mentioned shown in figure 1.3 to form either a radical anion or a neutral radical. The trapped radical could either be stabilized in the Q_o pocket by forming strong hydrogen bonds or salt bridges with the protein, or could be trapped in an electrostatic cage and not interact with the protein, which would leave the SQ_o highly unstable. High-field EPR and pulsed EPR techniques such as Electron Nuclear Double Resonance spectroscopy (ENDOR) were used to characterize the trapped SQ intermediate, as a radical anion or a neutral radical. Another pulsed EPR technique Electron Spin Echo Envelope modulation (ESEEM) was used to identify the interactions of SQ_o intermediate with the protein and the surroundings and the stability of the radical.

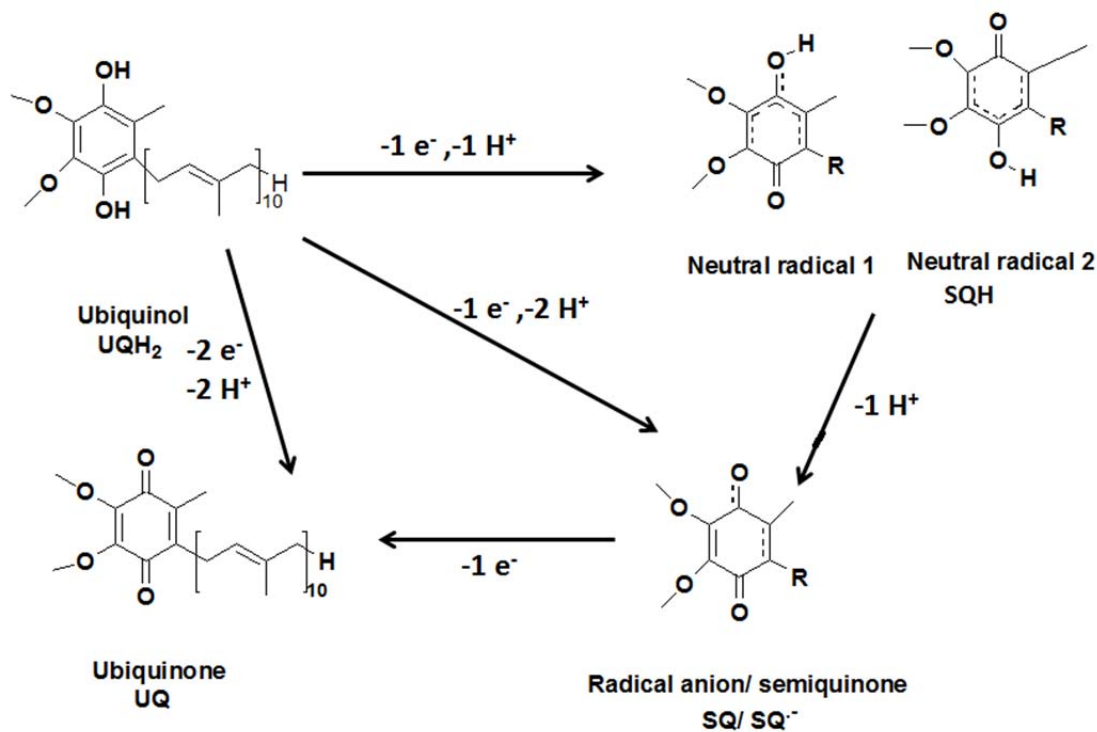


Figure 1.3 Schematic of the possible reactions to oxidize quinol. The species named as radicals are paramagnetic and can be detected using EPR.

The importance and relevance of the SQ depends on its location in *cyt bc₁*. The spin relaxation rate of a slow-relaxing spin is enhanced by magnetic interaction with a nearby fast-relaxing spin. The slow-relaxing SQ in the bacterial protein interacts with the fast-relaxing hemes in the protein and experiences paramagnetic relaxation enhancement (PRE) (53). We examined this PRE in detail in the mitochondrial *cyt bc₁* because PRE has been a useful probe for measuring distances between spins in proteins (57, 58) including the Fe₂S₂-heme *b_L* distance in *cyt bc₁* by Sarewicz et al. (59), copper ion bound to *cyt b_{6f}* (60), *cyt c* bound to *cyt c* oxidase (61), and spin-labeled metmyoglobin (62).

An attempt to identify the amino acid residues interacting with QH₂/SQ in the Q_o pocket has been started using mass spectrometric experiments. Initial progress in this ongoing effort is summarized.

CHAPTER 2

PREPARATION OF SQ RADICAL INTERMEDIATE

This chapter describes the biochemical procedures and other techniques to trap the SQ in protein. This mainly deals with the work I have done at Washington State University, Pullman, WA as part of my dissertation. This chapter provides a brief description about purification of *cyt bc₁* from yeast and bacteria, trapping the SQ intermediate in the protein using freeze-quench technique and initial characterization of trapped SQ.

2.1 EPR Sample preparation:

All reagents and chemicals, unless other mentioned, were purchased from Fisher Scientific or Sigma Aldrich. *Sacchaomyces cerevisiae* strain D273-10B was purchased from American Type Culture Collection.

2.1.1 *Extraction of cyt bc₁ complex from Saccharomyces cerevisiae cells:*

The following protocol describes the isolation of crude mitochondria from store-bought yeast (*Saccharomyces cerevisiae*), as described earlier by Ljungdahl et al. (63). It is modified from the original protocol (39). From a cell paste of 100-150 g, the typical yield is 150-200 mg mitochondrial protein. The method can be up or downscaled by at least a factor of two. The procedure requires the following isolation buffers, all are made fresh before use:

Buffer I: 100 mM tris(hydroxymethyl)aminomethane-acetate (tris-acetate), 150 mM potassium acetate, 250 mM sorbitol, 5 mM magnesium chloride, 1 mM dithiothreitol (DTT) and

1 mM phenyl methane sulfonyl fluoride (PMSF) added just before use, a pH of 8.0 was maintained.

Buffer II: 50 mM tris-acetate, 400 mM mannitol, 2 mM ethylenediamine tetraacetic acid (EDTA) and 1 mM PMSF added just before the use, a pH of 8.0 was maintained.

Buffer III: 50 mM tris-acetate, 150 mM potassium acetate, 2 mM EDTA and 1 mM PMSF added just before use, with a pH of 8.0.

Buffer IV: 50 mM tris-HCl, 1 mM magnesium sulfate and 1 mM PMSF added just before use, with a pH of 8.0.

Procedure:

1. Dry yeast of 1 Kg was washed with five liters chilled double distilled water (ddH₂O) and the cells were spun at 5,000g for 10 minutes at room temperature in tared bottles using H6000A centrifuge. The cells were recovered and the supernatant was discarded.
2. The recovered cells were washed with buffer I, and spun at 5,000g for 10 minutes and the supernatant was discarded.
3. The recovered yeast cells were resuspended in buffer I and the solution was poured in to a container with liquid nitrogen.
4. The frozen cells were broken to small chunks and blended with liquid nitrogen for 3-4 minutes, checking the level of liquid nitrogen in between.
5. The frozen yeast powder was then thawed to room temperature, suspended in buffer I and centrifuged at 3,000g for 10 minutes and the supernatant was collected, this step is repeated if necessary and the supernatants were mixed.

6. The combined supernatant was spun at 26,000g for 30 minutes and the pellet was collected for mitochondria.
7. The pellet was washed and suspended in buffer II, spun at 26,000g for 30 minutes, pellet was collected. This step is repeated again and the pellet was collected.
8. The pellet was washed and suspended in buffer III, spun at 26,000g for 30 minutes, and the pellet was collected and suspended in buffer III.
9. The resulting mitochondrial suspension was homogenized, added with equal volume of Glycerol and stored at -80 °C for later use and is termed as SMP.
10. The SMP was thawed to 4 °C washed with buffer IV, spun at 30,000g for 30 minutes, pellet was collected and this step was repeated.
11. The collected pellet was suspended in buffer IV, protein concentration was measured and adjusted as necessary using glycerol.
12. The protein is then mixed with 6mg/ml of n-dodecyl-beta-D-maltoside (β -DM) and stirred on ice for an hour in dark.
13. The mixture was then spun at 100,000g for 90 minutes in a SW28 rotor and the supernatant was collected and a gel column was run to isolate *cyt bc₁* complex.

2.1.2 Extraction of *cyt bc₁* complex from *Rhodobacter capsulatus* cells:

This work was done in Dr. Kramer's laboratory at Washington State University, Pullman.

1. The wild type *R. capsulatus* was obtained from Fevzi Daldal laboratory (University of Pennsylvania, Philadelphia, PA). These strains were inoculated in a mineral rich peptone-yeast extract, which contains 3 g/L peptone, 3 g/L yeast extract, 2 mM MgCl₂ and 2 mM CaCl₂.

2. These inoculated media was autoclaved at room temperature (23°C) with a magnetic spinner for 40 minutes, and incubated in a magnetic muffin pan for 3-4 days at room temperature and in dark.
3. The cells were collected after 3-4 days, spun at 10,000g at 4 °C for 10 minutes and the resulting pellet was collected. The pellet was resuspended in buffer I and spun at 10,000g for 10 minutes and the pellet was collected.
4. The pellet was suspended in buffer II and transferred to a French press. The cells were crushed at 1000 psi and the solution was spun for 10 minutes at 10,000g and the supernatant was collected to remove the cell debris.
5. The supernatant was then spun at 100,000g for 2 hours (28,000 rpm @ SW28 rotor) and the resulting pellet containing chromatophores were collected.
6. The resulting chromatophore suspension was homogenized, added with equal volume of glycerol and stored at -80 °C for later use.
7. The chromatophore suspension was thawed to 4 °C washed with buffer IV, spun at 30,000g for 30 minutes, pellet was collected and this step was repeated.
8. The collected pellet was suspended in buffer IV, protein concentration was measured and adjusted as necessary using glycerol.
9. The protein is then mixed with 6 mg/ml of β -DM and stirred on ice for an hour in dark.
10. The mixture was then spun at 100,000g for 90 minutes in a SW28 rotor and the supernatant was collected and a gel column was run to isolate *bc₁* complex.

2.1.3 Purification of *cyt bc₁* using ion-exchange chromatography:

A series of buffer or elution solvents were prepared which contain 50 mM tris-acetate, 1 mM MgSO₄, 0.01% β-DM and 20% glycerol at pH 8.0 with varying salt concentrations (100, 150, 200, 400 mM NaCl). Prior to loading the solubilized proteins, the column was packed under pressure with 500 mM buffer and then equilibrated with 100 mM buffer. The protein extraction was applied on to the DEAE-BioGel A column, and the gel was eluted first with 100 mM salt buffer solution for 10 minutes or until the eluted solution was colorless. The same elution process was employed with 150 mM and 200 mM salt concentration buffer solution. When the eluted solution after applying 200 mM was colorless, 400 mM salt concentration buffer was used. The *cyt bc₁* was eluted with the 400 mM salt concentration buffer and the eluted solution was collected until it becomes colorless. This part of eluate has only *cyt bc₁* and the collected eluate was tested for activity. The collected eluate was concentrated in Millipore-Amicon, or ISI Bioexpress-Vivaspin at 3,000g for 30 minutes at 4°C. The final concentration of the protein was measured and stored at -80°C.

2.1.4 *Cyt bc₁* concentration determination:

The concentration of the sample was estimated by measuring the redox-difference spectrum of *cyt b* absorbance between a fully-reduced state with excess dithionate and fully oxidized state with ferricyanide. The absorbance coefficient for wavelength pair 562-578 nm for *cyt b* was taken to be 25600 L mol⁻¹ cm⁻¹. The *cyt bc₁* was diluted as necessary in the buffer containing 50 mM MOPS, 100 mM KCl, 20 mM EDTA and 0.05% β-DM. To the diluted protein, 2 mM KCN was added followed by 1 mM ascorbic acid, then transferred into two identical cuvettes, one is labeled as sample and the other as reference. The absorbance spectrum

was measured from 540 nm - 580 nm, and this spectrum was used as base line for further calculations. A small amount of freshly prepared sodium dithionate was added to the sample cuvette to reduce the protein, and the absorbance was measured from 540 nm-580 nm. The cyt *bc₁* concentration was calculated from the difference of reduced and oxidized spectra at 562 nm and 578 nm by the following formula:

$$\text{Concentration} = \left(\frac{(\Delta A_{562} - \Delta A_{578})}{51.2} \right) \times \text{dilution factor}$$

2.1.5 Preparation of Freeze-Quenched EPR Samples:

For typical assay samples, 100 μM UQH₂ in buffer (50 mM Tris/100 mM KCl, pH 8.0) was reacted with 20 μM purified cyt *bc₁* complex in the same buffer, incubated with 30 μM AA or with AA and 30 μM stigmatellin as needed in a 1:1 ratio with a total reaction volume of 200 μl using the rapid freeze-quench apparatus (Model MPS-51; Biologic, Indianapolis, IN) as described in (64, 65) with modifications. Absorption and EPR spectra were measured before mixing to verify that the redox carriers of the cyt *bc₁* were in their oxidized states. The freeze-quench syringe drive and liquid propane bath were enclosed in a glovebox under an Argon (Ar) atmosphere with sealed electrical connections to the controller and computer. The reactants were typically incubated on ice under Ar for 2 hours before the experiment to generate anaerobic conditions. UQH₂ was diluted into buffer just before loading into the syringe reservoir. The lines leading from the syringes to the mixer and outlet were purged with 150 μl of each reactant over a time period of 50 ms, with the excess taken to waste by suction. A rapid shot of 100 μl from each syringe was routed through the mixer and outlet over a 27 ms time period into a bath of liquid propane. Freeze-quench shots were typically carried out in duplicate into the same liquid propane bath to give a total of 400 μl of frozen material. The liquid propane bath was contained in an

aluminum funnel surrounded by a secondary aluminum containment vessel suspended in liquid N₂. Samples for EPR spectroscopy were prepared by packing the freeze-quenched material through a small aperture at the bottom of the aluminum funnel using the shaft of a pre-cooled cotton swab into a 4-mm outer diameter, 4–5 cm long quartz EPR tube sitting in a second liquid propane bath. Approximately, two 150 μl EPR samples were prepared from each set of freeze-quench shots. The reproducibility of the EPR signal amplitudes between duplicate samples depended on sample packing density and the packing height within EPR tubes. Careful packing and attention to sample height allowed us to achieve good reproducibility in signal amplitudes from replicate samples, with differences between identical samples within the same preparation ranging from 5% to 10% of the total amplitude. The mixing time of the freeze-quench apparatus was calibrated as described (58) using the reaction of myoglobin with azide as a standard (50).

2.1.6 Preparation of UQ radicals in solution:

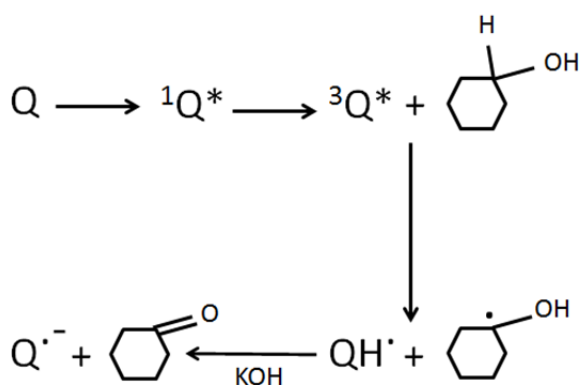


Figure 2.1 Photolysis scheme making quinone radical anion in cyclohexanol.

30 μg of Coenzyme Q10 (UQ) was dissolved in 100 μl of cyclohexanol to get 0.35 mM solution. Cyclohexanol unlike lower alcohols, is less polar and represents the hydrophobic Q_o pocket of the quinone binding site in the protein. KOH-saturated cyclohexanol was used to make the radical

anion. Radical anion in deuterated cyclohexanol was also prepared to study the effect of matrix environment. 1% Methanol was added to quinone, KOH-saturated cyclohexanol mixture to provide a more polar hydrogen bonding donor. 0.1% HCl was added to the quinone,

cyclohexanol mixture to get neutral radicals. All of the sample mixtures were transferred to EPR tubes, degassed by freeze-pump-thaw cycles to remove any air trapped in the solution, sealed and irradiated in liquid Nitrogen for 5 min using a Xenon arc lamp to produce the radicals. The irradiated samples were annealed to $-80\text{ }^{\circ}\text{C}$ for 15 sec to remove solvent (cyclohexanol) radicals that were produced during irradiation, but keeping the quinone radicals.

2.2 Preliminary EPR results:

The 77 K CW-EPR spectrum of freeze-quenched SQ is a single, nearly-symmetric line with g -factor ≈ 2.0044 and peak-to-peak line width of 1.16 mT (figure 2.2), similar to SQ from *R. capsulatus*, $g \approx 2.0054$, 1.19 mT width. We ruled out contribution from the Q_i site SQ because the experiments were performed in the presence of antimycin A (AA), which occupies this site, and also because the Q_i SQ has a distinctly narrower line width (~ 0.8 mT) than that we observed here. The Q_o site SQ signal largely disappears when stigmatellin (stig) blocks the Q_o site (figure 2.3), when UQH_2 is absent. The freeze-quench samples are reproducible and give similar cw-EPR results.

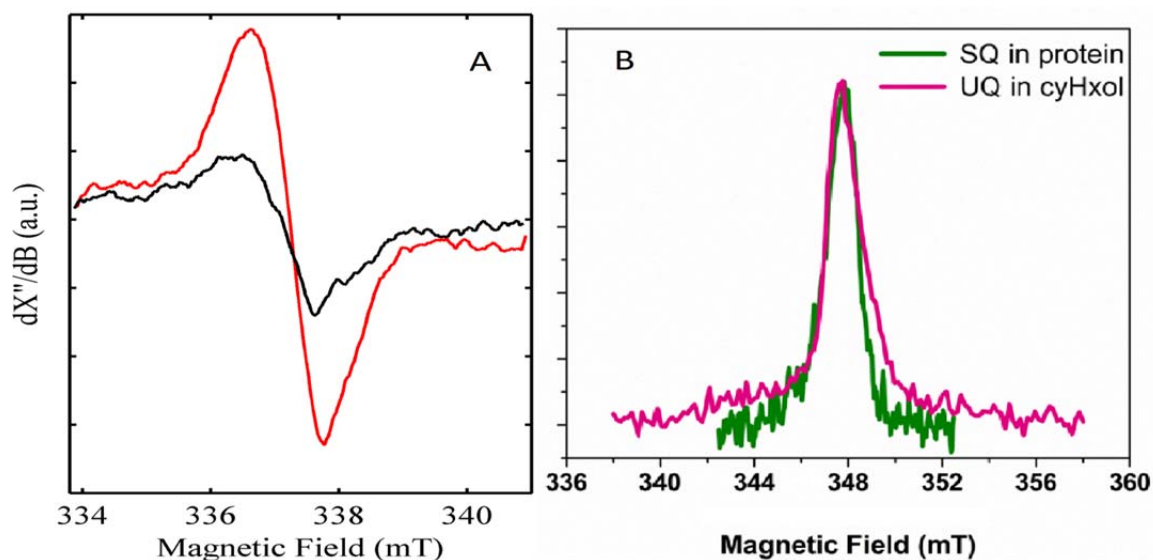


Figure 2.2 X-band EPR of SQ_0 and SQ in solution. CW-EPR spectra of SQ_0 in mitochondrial *cyt bc_1* with and without stigmatellin (A) and comparison of pulsed EPR spectrum of SQ_0 in protein and UQ radical anion in cyclohexanol (B) at X-band. Stig was slightly sub-stoichiometric in order to avoid a free radical signal present in many stig solutions.

Figure 2.2 also compares the EPR signal of SQ_0 with that of radical anion in cyclohexanol at X-band. They both have EPR signal at $g=2$ and have similar linewidths. Because it is not possible to differentiate between radical anion and neutral radical at X-band, due to poor Zeeman splitting, high-field EPR measurements would be helpful.

CHAPTER 3

THEORY

This chapter describes the theoretical basis for the EPR work that has been done. This chapter deals mainly with the EPR theory and explains several advanced EPR techniques that have been used in the work. A brief overview of the EPR theory is necessary to understand the experimental results further discussed in following chapters. The theory is kept brief for the greatest part and was taken from text books and review articles; only in special cases the original literature is cited. More detailed explanation of magnetic resonance theory can be found in many text books [Abragam et al. 1961; Carrington et al. 1967; Gringberg et al. 2004; Ernst et al. 1987; Berliner et al. 2000; Schweiger et al. 2001; Poole et al. 1971] (66-72) and will not be discussed in detail here.

3.1 The Hamiltonian Operator

The total energy of a spin system is described by the full Hamiltonian operator of the spins system in question. To simplify the formulas given here, only terms that are significant for our spin system and measurements will be retained. The terms that are of interest to this work are the electron Zeeman interaction $H^{\mathcal{F}}$, the nuclear Zeeman interaction H^{nz} , hyperfine interaction H^{hf} and spin-spin interaction $H^{spin-spin}$. The individual terms will be described in detail in the following sections.

$$\hat{H} = \sum_i \hat{H}_i^Z + \sum_j \hat{H}_j^{nZ} + \sum_{i,j} \hat{H}_{i,j}^{hf} + \sum_{(i-1)!} \hat{H}_i^{spin-spin} \dots \dots \dots \text{Equation 3.1}$$

3.1.1 Electron Zeeman Interaction

In a magnetic field B , an unpaired electron spin can orient either parallel to the applied magnetic field or anti-parallel to it. As a result the spins have two different energy levels labeled with symbols α and β , or with the quantum numbers $m_s = \pm 1/2$, to be defined. The interaction between the magnetic moment of an electron spin S and the external magnetic field is given by electron Zeeman term,

$$\hat{H}^Z = \beta_e \hat{S} \cdot \hat{g} \cdot \vec{B}_0 \dots \dots \dots \text{Equation 3.2}$$

where S is the spin vector operator, g is the gyromagnetic ratio or g -value. The energy of α and β levels for H^Z is given by replacing S by $m_s = +1/2$ and $-1/2$ respectively. Varying the magnetic field B also varies the energy-level separation as indicated in the energy level diagram figure 3.1.

Resonant absorption occurs when the energy of the applied frequency equals the energy difference between two levels.

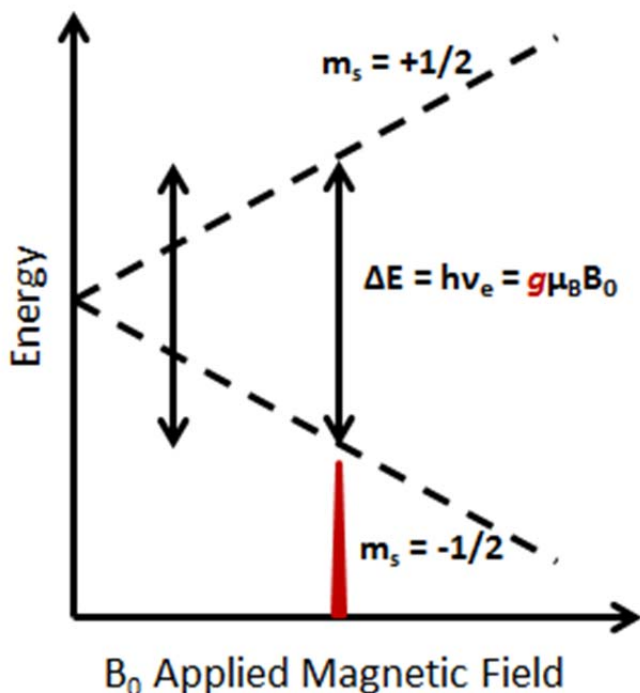


Figure 3.1 Electron Zeeman interactions.

The Zeeman splitting constant for the free electron is $g_e = 2.002319$, and is one of the most accurately known physical constants. The symbol g is utilized when electrons interact with other particles, in which case $g \neq g_e$. Deviation of the g -values from the free electron value is caused by coupling of the spin angular momentum to the orbital angular momentum (spin-orbit coupling), and is dependent on the surroundings of

the electron. The g is a tensor described by its eigenvalues g_x , g_y and g_z and has an orientation dependence that tracks the molecular axis system. For spin systems with cubic symmetry, g is isotropic, so $g_x = g_y = g_z$. Axially symmetric systems are described with two g -values $g_{||} = g_x = g_y$ and $g_{\perp} = g_z$. The most common systems like organic radicals and transition metals have rhombic local symmetry in which $g_x \neq g_y \neq g_z$, and the electron Zeeman interaction can be given as

$$\hat{H} = \beta_e (g_x B_x \hat{S}_x + g_y B_y \hat{S}_y + g_z B_z \hat{S}_z) \dots \dots \dots \text{Equation 3.3}$$

The g factors g_x , g_y and g_z are obtainable from the line positions measured with the field B along the X, Y and Z directions of the g -tensor. When B is along the Z-direction, for example,

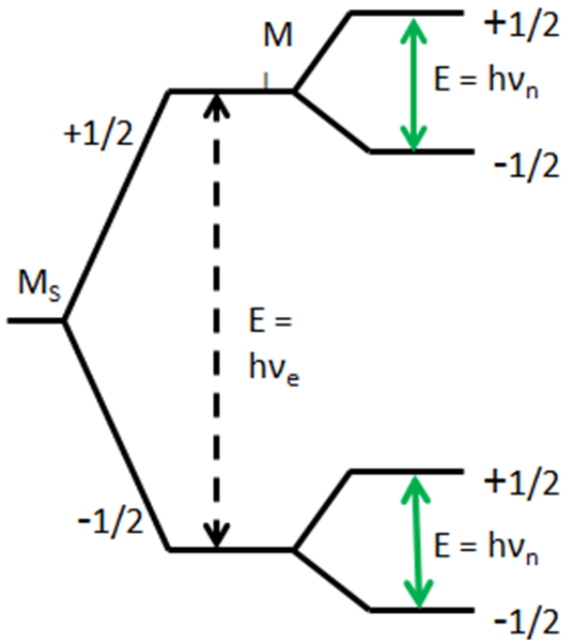


Figure 3.2 Nuclear Zeeman interaction.

3.1.3 Hyperfine Coupling

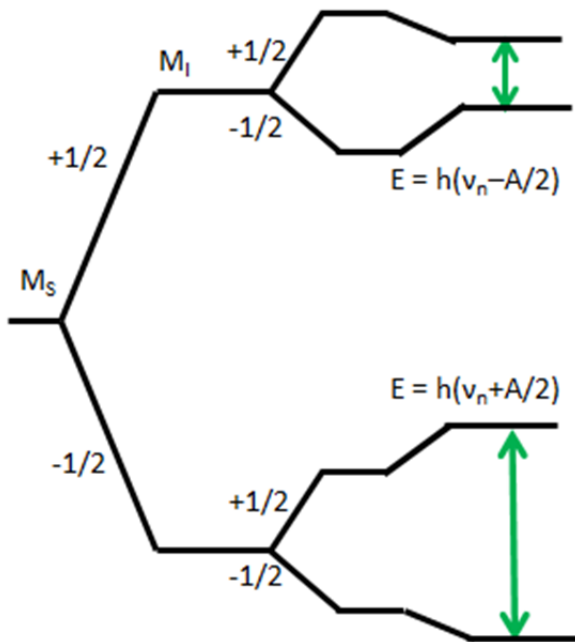


Figure 3.3 Hyperfine interaction for $S=1/2$ and $I=1/2$

The spin quantum operator I and the nuclear g-tensor g_n are properties inherent to a specific nucleus. In presence of a magnetic field, a spin system with nuclear spin $1/2$, has two energy states α and β . The nuclear hyperfine interaction splits each of the electron Zeeman levels into $(2I+1)$ levels, two levels when $I = 1/2$; the resulting set of four states are depicted in figure 3.2, along the fixed frequency transitions.

The hyperfine coupling is a result of the interaction between an unpaired electron and one or more nuclei, and the hyperfine interaction gives information about the local environment of the unpaired electron. The hyperfine interaction can be visualized as the interaction of the electron with the magnetic dipole field of the nucleus. The nuclear magnetic moment leads to a magnetic field $B_n(r)$, which is called the nuclear field. The electronic magnetic moment interacts with

nuclear field. The hyperfine interaction contributes to the total energy of each spin state and is represented as A in figure 3.3.

The hyperfine coupling consists of the isotropic part A_{iso} , which reflects the finite probability of the electron to be found at the nucleus, and of the anisotropic part A_{dip} , caused by the dipole-dipole coupling between the nuclear and electronic magnetic moments

$$\widehat{H}^{hf} = A_{iso} \cdot \widehat{S} \cdot \widehat{I} + \widehat{S} \cdot A_{dip} \cdot \widehat{I} \dots \dots \dots \text{Equation 3.6}$$

$$A_{iso} = \frac{2\mu_0}{3} g\beta_e g_n \beta_n |\varphi(0)|^2 \dots \dots \dots \text{Equation 3.7}$$

The spin-hamiltonian operator for the hydrogen atom (and other isotropic systems with one electron and one nucleus with $I = 1/2$) is obtained by

$$\widehat{H} = g\beta_e B \widehat{S}_z - g_n \beta_n B \widehat{I}_z + A_{iso} \widehat{I}_z \widehat{S}_z \dots \dots \dots \text{Equation 3.8}$$

The hyperfine term destroys the independence of the electron and nuclear spins. If more than one magnetic nucleus interact with the electron, the terms in I_{iz} are additive. Thus summing over all nuclei yields

$$\widehat{H} = g\beta_e B \widehat{S}_z - \sum_i g_{ni} \beta_n B \widehat{I}_{iz} + \sum_i A_{isoi} \widehat{S}_z \widehat{I}_{iz} \dots \dots \dots \text{Equation 3.9}$$

The dipolar part of the hyperfine coupling can be written as

$$A_{dip}(r) = -\frac{\mu_0}{4\pi} g\beta_e g_n \beta_n \left[\frac{\widehat{S} \cdot \widehat{I}}{r^3} - \frac{3(\widehat{S} \cdot r)(\widehat{I} \cdot r)}{r^5} \right] \dots \dots \dots \text{Equation 3.10}$$

Here r represents the vector joining the unpaired electron and the nucleus. The energy of the magnetic interaction between the spins varies as r^{-3} , and is independent of the sign of r .

$A_{dip}(r)$ describes an anisotropic interaction and expanding the vectors yields

$$A_{dip}(r) = -\frac{\mu_0}{4\pi} g\beta_e g_n \beta_n \left[\frac{r^2 - 3x^2}{r^5} \hat{S}_x \hat{I}_x + \frac{r^2 - 3y^2}{r^5} \hat{S}_y \hat{I}_y + \frac{r^2 - 3z^2}{r^5} \hat{S}_z \hat{I}_z - \frac{3xy}{r^5} (\hat{S}_x \hat{I}_y + \hat{S}_y \hat{I}_x) - \frac{3xz}{r^5} (\hat{S}_x \hat{I}_z + \hat{S}_z \hat{I}_x) - \frac{3yz}{r^5} (\hat{S}_y \hat{I}_z + \hat{S}_z \hat{I}_y) \right] \dots \dots \dots \text{Equation 3.11}$$

On averaging the Hamiltonian over the electron distribution (i.e., integrating over the spatial variables), this becomes a matrix quantity, having the form equation 3.12 and 3.13.

$$A_{dip}(r) = -\frac{\mu_0}{4\pi} g\beta_e g_n \beta_n \times \begin{bmatrix} \hat{S}_x & \hat{S}_y & \hat{S}_z \end{bmatrix} \cdot \begin{bmatrix} \left\langle \frac{r^2 - 3x^2}{r^5} \right\rangle & \left\langle -\frac{3xy}{r^5} \right\rangle & \left\langle -\frac{3xz}{r^5} \right\rangle \\ \left\langle -\frac{3xy}{r^5} \right\rangle & \left\langle \frac{r^2 - 3y^2}{r^5} \right\rangle & \left\langle -\frac{3yz}{r^5} \right\rangle \\ \left\langle -\frac{3xz}{r^5} \right\rangle & \left\langle -\frac{3yz}{r^5} \right\rangle & \left\langle \frac{r^2 - 3z^2}{r^5} \right\rangle \end{bmatrix} \dots \dots \text{Equation 3.12}$$

$$A_{dip} = \hat{S} \cdot T \cdot \hat{I} \dots \dots \dots \text{Equation 3.13}$$

Matrix T is symmetric about its main diagonal and is traceless.

The full spin Hamiltonian requires the addition of hyperfine term, electron Zeeman term and nuclear Zeeman term

$$\hat{H} = g\beta_e B^T \cdot \hat{S} + \hat{S}^T \cdot A \cdot \hat{I} - g_n \beta_n B^T \cdot \hat{I} \dots \dots \dots \text{Equation 3.14}$$

where, the hyperfine parameter matrix

$$A = A_{iso} U_{3 \times 3} + T \dots \dots \dots \text{Equation 3.15}$$

Two alternative parameters are useful when hyperfine anisotropy occurs.

$$a_0 = A_{iso} = \frac{(A_1 + A_2 + A_3)}{3g_e\beta_e} \dots \dots \dots \text{Equation 3.16a}$$

$$b_0 = \frac{[A_1 - (A_2 + A_3)/2]}{3g_e\beta_e} \dots \dots \dots \text{Equation 3.16b}$$

$$c_0 = \frac{(|A_2| - |A_3|)}{2g_e\beta_e} \dots \dots \dots \text{Equation 3.16c}$$

Here A_1, A_2, A_3 denotes the principal values of A , ordered such that $|A_2| - |A_3|$ is non-negative and is no larger than $|A_1| - |A_2|$ or $|A_1| - |A_3|$. The new parameters b_0 is called uniaxiality parameter and c_0 is called asymmetry or *rhombicity* parameter, are independent of a_0 and vanish if there is no anisotropy.

The SQ_0 trapped in cyt bc_1 is highly unstable and polar and usually interact with the protein surroundings to be stabilized. The hyperfine interaction would be a good probe to identify and characterize the interactions between SQ_0 and protein, and get basic knowledge about the SQ_0 surroundings in the Q_0 pocket.

3.1.4 Spin-Spin Coupling

Electron spins are magnetic dipoles and the interaction between two spins is termed dipole-dipole or dipolar interaction. This interaction depends strongly on the distance between the two spins, r , and on the orientation of vector r with respect to the applied magnetic field

$$\hat{H}^{spin-spin} = \gamma_A \gamma_B \left[\frac{\hat{S}_A \cdot \hat{S}_B}{r^3} - \frac{3(\hat{S}_A \cdot \vec{r})(\hat{S}_B \cdot \vec{r})}{r^5} \right] \dots \dots \dots \text{Equation 3.17}$$

Where γ_A and γ_B are the gyromagnetic ratios and \hat{S}_A and \hat{S}_B are the spin operators of spin A and spin B, respectively. When the scalar products in equation 3.17 are expanded and the expression converted into polar coordinates, we obtain

$$\hat{H}^{spin-spin} = \frac{g_A^{eff} g_B^{eff} \beta_e^2}{r^3} (A + B + C) \dots \dots \dots \text{Equation 3.18}$$

where,

$$A = (3\cos^2(\theta_D) - 1)S_z^A S_z^B$$

$$B = -\frac{3}{2}\sin(\theta_D) \cos(\theta_D) \exp(-i\varphi_D) (S_z^A S_+^B + S_+^A S_z^B)$$

$$C = -\frac{3}{2}\sin(\theta_D) \cos(\theta_D) \exp(+i\varphi_D) (S_z^A S_-^B + S_-^A S_z^B)$$

Where Θ_D is the angle between the r-vector and the z-axis of the magnetic field, Ψ_D is the angle between the projection of the r-vector and the xy-plane of the magnetic field and the x-axis, S_+^k and S_-^k ($k = A, B$) are the spin raising and spin lowering operators of spin k respectively, given by $S_+ = S_x + iS_y$ and $S_- = S_x - iS_y$

The terms A is important for the EPR spectrum and total energy in equation 3.1, while B and C are responsible for relaxation discussed in the next section. In many cases the high-field approximation is valid, meaning the spins are quantized along the magnetic field, so that the A term dominates

$$\hat{H}^{spin-spin} = \frac{g_A^{eff} g_B^{eff} \beta_e^2}{r^3} (3\cos^2(\theta_D) - 1) \dots \dots \dots \text{Equation 3.19}$$

In cyt bc_1 the $H^{spin-spin}$ is too small to be detected in CW spectrum, but the spin-spin dipolar interaction can be detected through their contribution to spin relaxation and provide a way to measure distance between spins.

3.2 Relaxation

The processes by which a spin system returns to its equilibrium state after excitation are called relaxation processes. There are two different types of relaxations, one is longitudinal relaxation also called spin-lattice relaxation usually represented as T_1 and the other is transverse relaxation also called spin-spin relaxation usually represented as T_2 . This section describes in detail about the T_1 and T_2 relaxation processes, mechanisms and experimental methods by which they can be measured. For the most part it is kept brief and the reader can find a more detailed explanation in these text books (71-76).

Longitudinal relaxation processes change the total energy of the spin system by inducing a change in the magnetic quantum numbers m_s . The same amount of energy is absorbed or provided by the environment in order to conserve energy. In general, T_1 is the time constant associated with processes that restore the spin system to equilibrium. T_1 is therefore defined as

$$\frac{dn}{dt} = -\frac{n - n_0}{T_1} \dots \dots \dots \text{Equation 3.20}$$

where n is the population difference between the two energy levels ($m_s=+1/2$ and $-1/2$), and n_0 is n when the system is in equilibrium. The spin system gets excited and builds up magnetization whenever a microwave pulse is applied and when the pulse is switched off, the system lose magnetization and returns to equilibrium as a function of $\exp(-t/T_1)$.

T_1 relaxation is also called as spin-lattice relaxation because it is caused by the coupling of the spin to vibrations of the “lattice”, or environment of the spin. The environment can either be a crystal lattice, the surrounding solvent, or even the protein in which the spin is embedded. In

a system with spin states separated by an energy interval $\Delta E = \hbar\omega_o$, lattice vibration of frequency ω can induce transitions only if ω is in the range of Larmor frequency ω_o . The efficiency of a relaxation process depends strongly on the spectral density, which is a function of frequency distribution, around ω_o . A typical vibration with correlation time T_c has a spectral density function given by a Lorentzian line shape

$$J(\omega_0) = \frac{\tau_c}{1 + \omega_0^2 \tau_c^2} \dots \dots \dots \text{Equation 3.21}$$

The maximum in spectral density and relaxation rate is found when $\omega_o T_c = 1$.

T_2 relaxation does not cause the spin system to lose energy unlike T_1 relaxation. T_2 relaxation or spin-spin relaxation causes loss of coherence, whereas T_1 relaxation leads to loss of magnetization. One process causing transverse relaxation is an energy-conserving flip-flop process of two spins. A spin flip that leads to longitudinal relaxation also destroys coherence, which means that T_1 relaxation can contribute to T_2 relaxation. This indicates that T_2 can be smaller than or equal to T_1 , but never much larger than T_1 . In solids, the network of coupled spins is virtually infinite, so that T_2 is often not well defined (77).

3.2.1 Processes causing spin-lattice relaxation

There are three main processes that transfer energy from a spin to the lattice: the direct process, the Raman process and the Orbach process.

The direct process involves the absorption of a phonon that has a frequency equal to the Zeeman frequency of the spin system. This process depends linearly on temperature, and (for $S=1/2$) depends on the magnetic field to the fourth order. The direct process is often the most

present, the Orbach process is more efficient than the Raman process and has a characteristic temperature dependence

$$\frac{1}{T_1} = \frac{\Delta_{Orb}^3}{\exp(\Delta_{Orb}/k_B T) - 1} \dots \dots \dots \text{Equation 3.23}$$

In which Δ_{Orb} is the energy difference between the ground state and the involved excited state, and k_B is the Boltzman constant. Aside from a possible dependence of the energy of the excited state on the external magnetic field, the Orbach process is independent of magnetic field (77).

The spin-lattice relaxation times at room temperature vary from tens of femtoseconds in lanthanide solutions to nanoseconds in metal ions to microseconds and even milliseconds in organic radicals.

3.2.2 *Processes contributing to Transverse Relaxation*

In practice, T_2 is usually not the dominating process of spin-echo dephasing, many other processes can contribute to echo decay. In some cases competing relaxation processes can cause non-exponential echo decay so that the spin-spin relaxation can no longer be described by a single time constant. The relaxation time is then described by the time it takes for the echo to decay to $1/e$ of its starting intensity. In this dissertation, the term T_2/T_M will be applied to both exponential and non-exponential echo decays.

One of the major processes that contribute to signal decay is spectral diffusion. These are processes that move magnetization through the EPR spectrum. If the EPR spectrum is only partly excited, the magnetization can be shifted out of the detection window, causing a decrease in echo

intensity. Spectral diffusion can be caused by flip-flop processes involving spins that are excited (A spins) and the spins that are not (B spins). Another source of spectral diffusion is reorientation of the molecule on the time scale of the experiment, causing changes in the Larmor frequency of the excited species. The reorientation of the molecule may cause anisotropic relaxation in the spectrum. Cross relaxation is another process that causes transverse relaxation and is closely related to spectral diffusion, although in this case mutual spin flips between unlike spins, such as electrons and nuclei, are involved (77).

A process that can strongly enhance the transverse relaxation is the relaxation caused by dipolar coupling between two paramagnetic species. This special case of spectral diffusion will be discussed in detail in the next section.

The total echo decay is given by the product of the independent relaxation processes. If the relaxation processes are single exponentials, the total transverse relaxation time T_2 is therefore given as the inverse of the sum of the reciprocal relaxation times of the individual involved process (spectral diffusion, sd; and dipolar relaxation, dip).

$$\frac{1}{T_M} = \frac{1}{T_2} + \frac{1}{T_2^{sd}} + \frac{1}{T_2^{dip}} \dots \dots \dots \text{Equation 3.24}$$

The transverse relaxation times vary from femtoseconds in systems with $S > 1/2$ to microseconds in organic radicals.

3.2.3 Dipolar relaxation enhancement

For two unlike coupled spins, in which one relaxes much faster than the other, dipolar coupling manifest itself as a change in the relaxation behavior of the slower relaxing spin. From

time-dependent perturbation theory, it can be shown that a local minimum in the longitudinal relaxation time T_1 of the slow relaxing spin (spin A) occurs when the relaxation rate $K=1/T_{1B}$ of the fast relaxing spin (spin B) equals the Larmor frequency of the slower relaxing spin. Similarly a minimum in the transverse relaxation time of spin A can be found when the relaxation rate K is equal to the dipolar coupling strength Δ_{Dip} between spin A and spin B, in angular frequency units. The T_1 relaxation enhancement measurements are extremely sensitive to distances between paramagnetic centers due to a r^{-6} dependence of Δ_{Dip} , given the T_1 is long enough. In spin systems, with very short T_1 , the transverse relaxation enhancement is an effective way to measure the distance between the two paramagnetic species.

The transverse relaxation enhancement of the slower relaxing spin caused by dipolar coupling to a fast relaxing spin is

$$v(2t) = \left[\left(chR\tau + \frac{W}{R} shR\tau \right)^2 + \frac{A^2(r)}{4R^2} sh^2 R\tau \right] \exp(-2W\tau) \dots \dots \dots \text{Equation 3.25}$$

$$R^2 = W^2 - A^2(r)/4$$

$$A = g_1 g_2 \beta^2 \hbar^{-1} (3 \cos^2(\theta_D) - 1) r^{-3}$$

Here W is the random spin flip frequency of the fast-relaxing spin partner, which is $1/2T_1$.

The dipolar relaxation enhancement has a very specific dependence on $1/T_1$ of the fast relaxing spin. As T_1 is strongly temperature dependent, dipolar relaxation also depends strongly on temperature. T_M relaxation enhancement is a resonance like phenomenon and the maximum T_M relaxation point correspond to a temperature, where the relaxation rate of fast-relaxing spin equals the dipolar coupling between fast and slow relaxing spins. The dipolar coupling strength

also depends on the orientation of θ_D , the angle between the external magnetic field and the vector connecting the two dipolar coupled spins. At some angles the dipolar relaxation will be maximal (where $\theta_D=0$) and at other angles dipolar relaxation will not be seen (where $\theta_D=54.7^\circ$) (77).

3.2.4 *Methods of measuring distance by EPR*

The measurement of dipolar coupling between two spins gives a measure of distance between two spins. As discussed above, the presence of a second spin, spin B changes the EPR frequency of the observed spin, spin A. There are several methods in EPR to determine the strength of the dipolar coupling, hence the distance between two spins.

CW Methods: The dipole-dipole interaction of two coupled spins causes the resonance lines of the observed spin to split in two. Neglecting J and taking only the first secular term of the dipolar Hamiltonian 2.6, the frequency of this splitting (in rad s^{-1}) is given by equation with ν_{Dip} the dipolar splitting in Hz.

$$\omega_{Dip} = 2\pi\nu_{Dip} = \frac{g_A^{eff} g_B^{eff} \beta_e^2}{hr^3} (3\cos^2(\theta_D) - 1) \dots \dots \dots \text{Equation 3.27}$$

When the full EPR line is excited, the split lines display a so-called Pake pattern. This pattern is obtained by summing up all dipolar coupling frequencies resulting from orientations of the molecule where $\theta_D = 0^\circ$ to those where $\theta_D = 90^\circ$, weighted by the probability of the respective orientation given by $\sin\theta_D$. In most cases, the Pake pattern is not resolved due to inhomogeneous line-broadening. The EPR line width of the observed spin plays a major role in determining the distance from dipolar coupling. The dipolar coupling can be undermined if the

exponential-like echo decay and a faster damping of the oscillation. A more detailed explanation about the PELDOR experiment can be found in [Milov et.al., 1984; Larsen et.al., 1993; Martin et.al., 1998] (78-80).

Relaxation Induced Dipolar Modulation Enhancement: In dipolar- coupled systems where one of the spins has a short T_1 there is no need of a pumping pulse to study dipolar interaction. In the relaxation-induced dipolar modulation enhancement (RIDME) experiment the Larmor frequency of the detected spin A is affected by spontaneous spin flips of the coupled spin.

The first $\pi/2$ pulse in the RIDME sequence flips the A spins in to the xy-plane where they start to dephase, creating a polarization grating. The second $\pi/2$ pulse rotates the magnetization into the xz plane where it is stored for a time t . During t , the faster relaxing B spin flips due to T_1 relaxation and so changes the Larmor frequency of spin A. After the A spins have been rotated into the xy plane by the third $\pi/2$ pulse, the coupled spins do not refocus and a decrease in echo intensity is observed. With $\tau \ll T_{1B}$ and (where T_{1B} is T_1 of the B spin), spin flips of the B spins only occur during t and the signal is independent of the particular moment at which the Larmor frequency of spin A has changed. If t is kept fixed and τ is stepped, an echo decay trace is obtained that is modulated by $\cos(\omega_{Dip}\tau)$, similar to the PELDOR signal. Details about this experiment can be found in references (81-83).

Dipolar Relaxation Enhancement: Dipolar relaxation measurements are closely related to the PELDOR and RIDME experiments in that they rely on the dephasing of A spins due to spin flips by B spins to which they are dipolar coupled. Like in RIDME, the B spins are not excited

by an additional microwave pulse, but flip due to T_1 relaxation processes. The echo intensity of the A spins is recorded with a simple Hahn echo sequence as a function of pulse separation time, τ . Changes in the Larmor frequency of spin A occur due to stochastic flips of spin B caused by T_1 relaxation during the time τ between the two pulses. This process is the same as in the case of RIDME, except that in this case the flips of the B spins occur at any time between $t=0$ and $t=2\tau$, causing relaxation enhancement instead of modulation of the echo signal. This complicates the analysis of dipolar relaxation data, and a single measurement no longer suffices to unambiguously obtain all structural parameters. Relaxation measurements over a wide range of temperature will provide the information of distance between two paramagnetic species, given the T_1 of fast relaxing spin is known.

3.3 Experiments used

A major part of this section is summarized from a review article by Hadjilias et al. (84) and was kept brief, the reader can find more detailed explanation in the article. For the past couple of decades, pulsed EPR techniques have proven to be a great tool to measure and characterize the paramagnetic species including metal centers, organic radicals and many proteins. The paramagnetic species interact with the nuclei of the ligands and surroundings to give hyperfine and quadrupole couplings. These hyperfine and quadrupole couplings can be probed to get the information about the structure, bonding, composition and surroundings of the paramagnetic species (84).

The spin couplings provide a wealth of detailed information about the electronic, molecular and chemical structure of the system under investigation if analyzed properly. These spin couplings are well defined for a crystalline sample and are easy to analyze and interpret. But

most EPR or paramagnetic samples are either powder samples or polycrystalline (frozen solution) oriented in multiple directions with respect to the magnetic field. This powder or polycrystalline samples multiple sets of overlapping hyperfine and quadrupole spin couplings, which makes it difficult to analyze and interpret those couplings to the surroundings of the paramagnetic species. The properties of the EPR spectra of powder sample are determined mainly by the symmetry of the g and A tensors, values of their components and the line width. Quadrupole interactions, which are non-zero for nuclei with $I > \frac{1}{2}$, usually have second order shifts in the polycrystalline EPR spectra. In principle the hyperfine and quadrupole couplings are manifested as splitting in the EPR spectra. However, the hyperfine and quadrupole splitting information is lost in most of the paramagnetic samples, due to the low resolution and inhomogeneous broadening in the powdered samples (84).

The information about hyperfine and quadrupole splitting can still be obtained using advance EPR techniques such as Electron Nuclear Double Resonance (ENDOR) and Electron Spin Echo Envelope Modulation (ESEEM) (85). In ENDOR experiment, the nuclear information coupled to the electron spin is obtained by applying both microwave (MW) and radio frequency (RF) pulses on the system and monitor the effect of RF pulses on the EPR intensity of the sample. ENDOR technique combines both EPR and NMR techniques and retains the information of both electron and interacting nuclear spins. The ENDOR experiment is a frequency domain experiment. In ESEEM experiments, the NMR transitions are observed indirectly through the mixing of the frequencies of the semi-forbidden and allowed EPR transitions, which have been coherently excited using short intense MW pulses. In contrast to ENDOR, ESEEM experiment is time domain (84).

ESEEM and ENDOR experiments give complimentary information and the spectral shapes differ from each other. ENDOR gives information about strong hyperfine couplings and ESEEM has information about weak hyperfine couplings. Weak nuclear couplings can also be resolved by pulsed ENDOR experiment using either Mims ENDOR or dead time independent Re-focused Mims ENDOR sequence.

3.3.1 ESEEM experiments:

ESEEM experiments are performed by recording the echo intensity generated by a sequence of resonant microwave pulses, separated by evolution times, i.e., periods where the microwave power is off; the recorded echo-envelope is the time-domain ESEEM signal. In the presence of nuclear spins weakly coupled with the electron spin, the intensity of the echo is modulated at the nuclear transition frequencies of the interacting nucleus (85). The standard one-dimensional ESEEM experiments consist of two, three and four pulse sequences, figure 3.4.

The two-pulse ESEEM experiment was first introduced by Rowan, Hahn and Mims (85). In the two-pulse experiment, figure 3.4, a Hahn echo sequence is applied, the time between first ($\pi/2$) and second (π) pulse being τ . The echo intensity of the primary echo at time τ after second pulse is recorded. The modulation envelope, obtained as τ is incremented, is related to the nuclear transition frequencies within an electron spin manifold. For nuclear spin $I=1/2$, which is the simplest case, the expression for two-pulse ESEEM is

$$E_{2p}(\tau) = \frac{k}{4} \left[2 - 2 \cos(\omega_\alpha \tau) - 2 \cos(\omega_\beta \tau) + \cos((\omega_\alpha + \omega_\beta)\tau) + \cos((\omega_\alpha - \omega_\beta)\tau) \right] \dots \dots \dots \text{Equation 3.29}$$

$$k = 4c^2 s^2$$

where k is the modulation depth and c^2 and s^2 being the transition probabilities of the allowed and semi-forbidden transitions, respectively.

$$I_{allowed} = c^2 \left[\frac{\omega_I^2 - \frac{(\omega_\alpha - \omega_\beta)^2}{4}}{\omega_\alpha \omega_\beta} \right]$$

$$I_{forbidden} = s^2 \left[\frac{\omega_I^2 - \frac{(\omega_\alpha + \omega_\beta)^2}{4}}{\omega_\alpha \omega_\beta} \right]$$

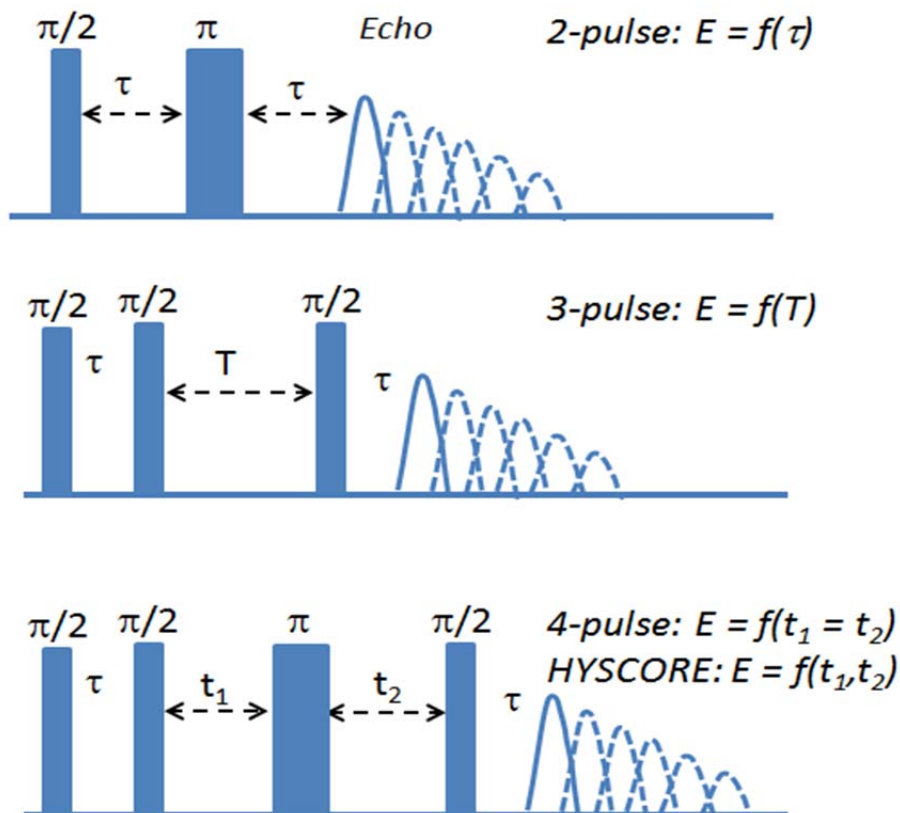


Figure 3.4 ESEEM pulse sequence. A schematic of the pulse sequence for 2-pulse, 3-pulse, 4-pulse and HYSCORE experiments with their respective echoes as a function of time details. See text for more details.

There are few limitations for the two-pulse ESEEM. The 2PESEEM spectrum is difficult to analyze as the modulation has the sum and difference of the basic nuclear transition

frequencies are often broad and weak, that is difficult to resolve. In four-pulse ESEEM, combination peaks appear as narrow features in the spectrum, since orientation-dependent hyperfine interactions are partially refocused. The four-pulse procedure is more advantageous for measuring combination lines than the two-pulse since it is free from phase-memory limitations, but also suffers from τ -dependent blind spots (87). To overcome this problem, a blind-spot free two-dimensional ESEEM method for measuring sum combination-frequencies has recently been developed (93) (84).

3.3.2 *ENDOR experiments*

ENDOR (Electron Nuclear Double Resonance) is a double resonance technique that combines NMR and EPR. The advantage of the ENDOR is that it has the high resolution and nuclear information like in NMR and high sensitivity like in EPR. The ENDOR experiment is performed by monitoring the EPR signal intensity while sweeping a RF (Radio Frequency) pulse to drive the NMR transitions. Double resonance experiments such as ENDOR require more effort than simpler EPR or NMR experiments, but ENDOR gives more insight into the structure, dynamics, and electronic structure of the system. In ENDOR the applied RF pulse will change the observed EPR intensity. The net change in the EPR intensity with the applied RF pulse is the ENDOR intensity (94-96).

The selection rules for EPR transitions are: $\Delta m_S = \pm 1$ and $\Delta m_I = 0$. The energy level transitions that comply to the EPR selection rules for a spin system with $S=1/2$ and $I=1/2$ are labeled as EPR in figure 3.5 with resonant frequencies of: $\nu_{EPR} = \nu_e \pm A/2$. The EPR signal is split into two lines with a separation of A . Most of the times, the resonant frequency for EPR transitions lies in the microwave region. In an EPR spectrum, the nuclear information is lost as

the first order nuclear Zeeman contribution (ν_n) cancels out and, it is not possible to identify the nuclei.

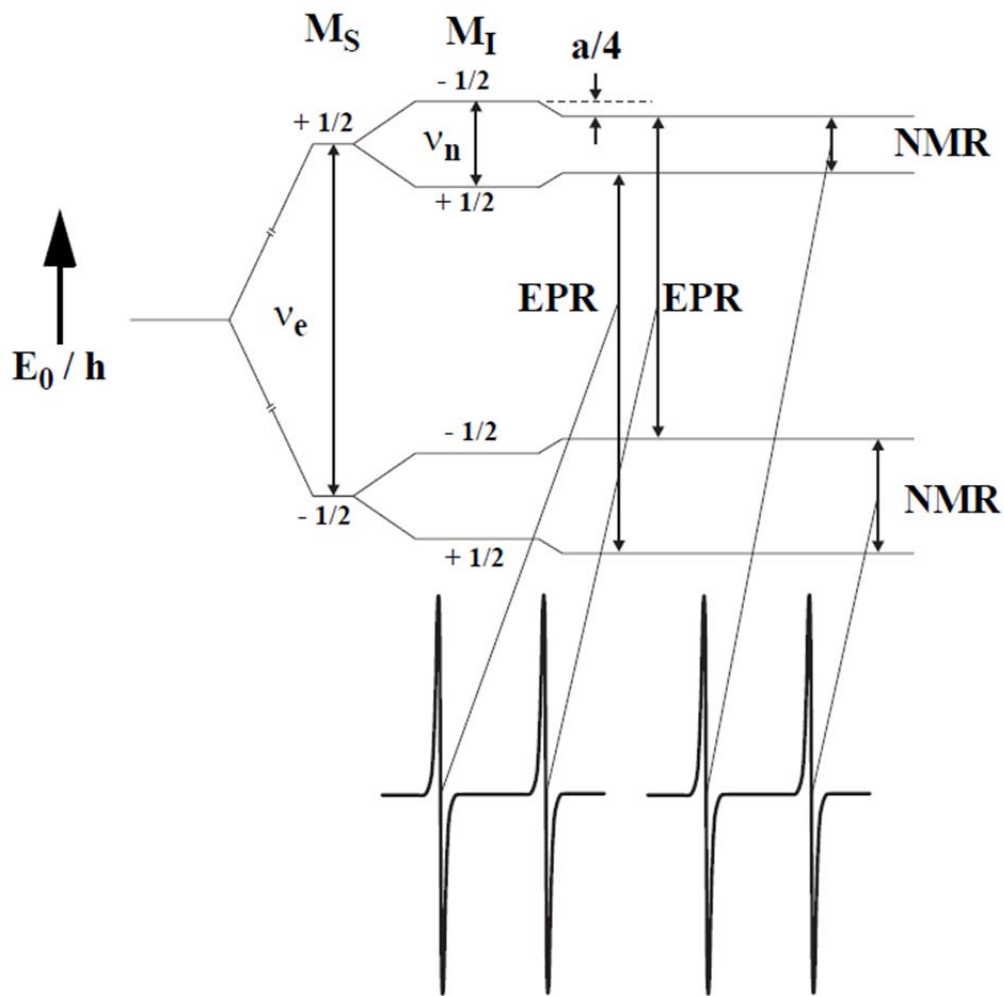


Figure 3.5 ENDOR. Representation of EPR and NMR transitions in a spin system with $S=1/2$ and $I=1/2$.

The selection rules for NMR (and ENDOR) transitions are: $\Delta m_S = 0$, $\Delta m_I = \pm 1$. The energy level transitions that comply to the NMR selection rules for a spin system with $S=1/2$ and $I=1/2$ are labeled as NMR in figure 3.3 with resonant frequencies of: $\nu_{\text{NMR}} = \nu_n \pm A/2$, which

results in two NMR transitions. If $\nu_n > A/2$ and $\nu_{NMR} > 0$, the NMR signal will be centered at ν_n with a splitting of A and if $\nu_n < A/2$, the NMR signals will then be centered at $A/2$ with a splitting of $2\nu_n$. In most experiments the resonant frequency for NMR transitions lies in the radio frequency region. Unlike EPR, the NMR spectrum contains information regarding the nuclear Zeeman interaction (ν_n), which facilitates the identification of the nucleus. Although the NMR experiments is still limited as for assigning the signs to the positive and negative frequencies, hence represented only as absolute values.

If there is a second nucleus interacting with the electron, each of the EPR signals is further split into another pair, resulting in four lines. For N spin $1/2$ nuclei with different hyperfine splitting, 2^N EPR signals with similar intensity will be observed. And for N spin $1/2$ nuclei with identical splitting, only $2N+1$ EPR lines will be observed and the intensity varies as Pascal's triangle progression. The number of EPR lines increases exponentially with the number of nuclei. Many times there are so many signals with small difference in hyperfine splitting that we only observe a single broad peak, as they overlap each other. This phenomenon is called inhomogeneous broadening and all the important information we hoped to obtain from the hyperfine splitting will be lost.

The problem is that each electron is surrounded by a large number of nuclei and the electron is interacting with them all simultaneously. On the other hand if we consider the nuclei, each nucleus interacts with only one electron because there are many more nuclei than unpaired electrons. The electron, which has a spin of $1/2$, will split the NMR lines in two. The interactions between the nuclei themselves are so small compared to the hyperfine interaction that for all practical purposes we can ignore them. If we measure the nuclear splitting directly by an NMR

experiment, we can obtain a much simpler spectrum because for N spin $1/2$ nuclei, we will generally observe 2^N NMR signals instead of the 2^N signals in an EPR spectrum. For N nuclei with identical hyperfine splitting, only 2 NMR signals appear. The information that appeared lost in the EPR experiment (the hyperfine splitting) can still be obtained from an NMR experiment because of the reduction in the number of lines. ENDOR is a successful experiment to resolve the inhomogeneous broadening, but cannot resolve homogenous broadening.

In summary the ENDOR experiment combines the superior resolution from NMR experiment and the high sensitivity of the EPR experiment. We can measure the g_n from and ENDOR experiment and the nuclear information is retained. Although there are still some limitations to ENDOR experiment like it is very complicated and the information regarding the number of nuclei will be lost. The second problem can be overcome by high resolution EPR spectrum and careful simulations.

In pulsed ENDOR experiment the microwave and RF pulses were applied separately and in short time intervals, unlike in CW-ENDOR where both MW and RF pulses were applied at the same time. A set of MW pulses are used to create an echo and are called preparative pulses. These preparative pulses are followed by a mixing time, in which the RF pulse is applied and transfers the m_s spin manifold, if there is any resonant NMR transition. This mixing period is then followed by another set of MW pulses and called as detection pulses, which measure the EPR signal after the mixing time. If the radio frequency hits a nuclear spin transition, the electron spin echo intensity will change and the RF sweep over a certain frequency range results in the ENDOR spectrum.

Pulsed ENDOR spectroscopy has several advantages over the conventional CW-technique:

1. It requires no critical balance of RF power and relaxation times, a condition which has to be met in many cases of CW-ENDOR.
2. It is less susceptible to artifacts as there is no RF and no microwave field applied during the detection period.
3. It gives access to all relaxation times of a spin system (electron T_1 & T_2 , nuclear T_1 & T_2 , cross relaxation).
4. It complements the results obtained from Electron Spin Echo Envelope Modulation (ESEEM).
5. It allows the manipulation of the spin system to observe one particular spin property with high selectivity and sensitivity.
6. The ENDOR effect can be as large as the electron spin echo intensity itself.

The Mims ENDOR technique is based on a stimulated electron spin echo (ESE) sequence, using a two $\pi/2$, preparation pulse sequence to invert the electron spin population, and a final $\pi/2$ pulse after the mixing period to stimulate the ESE for signal detection, see figure 3.6. Between the preparation pulses and the final $\pi/2$ pulse, a RF pulse is used to invert the nuclear spin population, resulting in polarization transfer between the nuclear and electronic transitions in the so called “mixing period.” This results in the actual ENDOR transitions, changes in the intensity of the EPR transition, detected by ESE MW-pulse sequence. The echo intensity is subsequently measured as a function of the RF frequency to give the characteristic ENDOR spectrum.

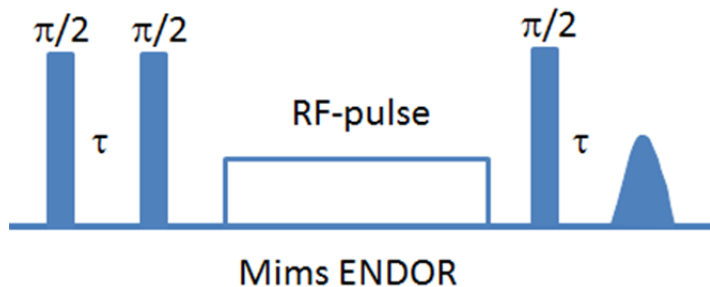


Figure 3.6 Mims ENDOR pulse sequence

In refocused Mims ENDOR experiment (ReMims ENDOR), an additional π pulse is applied after the $\pi/2$ pulse to get the refocused stimulated echo. This technique facilitates the use of small τ values and hence a better ENDOR signals without any blindspots.

The two techniques Davies and Mims ENDOR, are very similar to each other in their implementation. However they are relatively complementary in their results and usefulness. The Mims and ReMims ENDOR technique is most suited to weakly coupled nuclei, with small HFC constants, A , and the Davies ENDOR for those nuclei with relatively large HFC. This simplifies the assignments of strongly and weakly coupled nuclei, as well as the corresponding spectra associated with each of the pulse sequences.

CHAPTER 4

CHARACTERIZATION OF SQ INTERMEDIATE

The cyt *bc₁* complexes enhance energy storage in the form of proton motive force (*pmf*) via the Q-cycle mechanism. The QH₂ is oxidized at the Q_o site by transferring two electrons, one through high-potential chains and the other through the low-potential chain. In the process two QH₂ protons are released into the p-side of the membrane. This bifurcated reaction increases the proton pumping efficiency by transferring 2H⁺/1e⁻ through the high-potential chain, and the second electron recycles back to Q pool at the Q_i site. When a QH₂ is oxidized by one electron a SQ will be formed, and is highly reactive and readily reduces O₂ to superoxide or undergo bypass reactions that are energetically more favored. Under optimal conditions, normal electron flow in the Q-cycle is able to out-compete these bypass reactions. It is still unclear how the cyt *bc* complexes prevent bypass reactions and favor Q-cycle. A good knowledge of the chemistry that occurs at the Q_o site would provide more intuitive in this regard, because this is where a reductant to O₂ is likely to reside.

One of the major problems in the field is that the intermediates at the Q_o site of cyt *bc₁* have not been physically observed or characterized, making it difficult to test various proposed Q_o site models. I was able to trap SQ at the Q_o site in both bacterial and mitochondrial cyt *bc₁* complex and characterize the SQ_o using various pulsed EPR techniques. This chapter is a brief

review about the nature of SQ_o trapped in both bacterial and mitochondrial cyt *bc_L*, its interactions with protein and environment and its implications on the Q-cycle mechanism.

4.1 EPR Experiments:

X-band pulsed EPR measurements were carried out on a Bruker Elexsys-E680 spectrometer with EN4118X-MD4 resonator, DICE ENDOR, a 500 W ENI-500 rf amplifier and an ER4118CF cryostat with ITC503 controller. The 95-GHz experiments were done in our lab on Bruker Elexsys-E680 spectrometer with a Tetraspec W-band microwave bridge. The higher field 235 GHz experiments were done at National High Magnetic Field Laboratory (NHMFL), Tallahassee, Fl.

High-field EPR was used to increase the resolution and get the information about g-anisotropy of SQ radical, and several pulsed EPR techniques like ENDOR and ESEEM at X-band were used to probe the environment of the radical. Echo-detected field-swept EPR spectra were measured by recording the echo intensity from a ($\pi/2$ - τ - π -echo) pulse sequence as the magnetic field was swept. All the pulse experiments described were employed with appropriate phase-cycling schemes to avoid any unwanted signals and correct for baseline. The turning angles of the microwave pulses were nominally $\pi/2$ and π while the time between pulses was τ . One dimensional two-pulse, three-pulse and four-pulse ESEEM experiments were used to measure the echo envelope modulations. In a two-pulse ESEEM experiment, the Hahn echo sequence is used ($\pi/2$ - τ - π - τ -echo) and the intensity of the refocused echo was measured as a function of τ . In the three-pulse experiment ($\pi/2$ - τ - $\pi/2$ - t - $\pi/2$ - τ -echo), the intensity of the simulated echo was measured as a function of time t at a constant time, τ . In the four-pulse ESEEM experiment ($\pi/2$ - τ - $\pi/2$ - t_1 - π - t_2 - $\pi/2$ - τ -echo), the intensity of the echo after the fourth pulse

where ν_N is the NMR or nuclear Zeeman frequency, which is often much greater than A , and ν_{ENDOR} is the ENDOR frequency. The value of the ENDOR frequencies depends on the vector sum of the applied magnetic field and local magnetic field induced on the nucleus by the isotropic and anisotropic hyperfine interactions with electron spin. As a result protons that are at different distance and different orientations have different hyperfine interactions, and the ENDOR frequencies vary slightly, but all lie around proton Larmor frequency (~ 14.5 MHz at X-band).

Electron spin-echo envelope modulation (ESEEM) spectroscopy is also a powerful method to study semiquinones in proteins. It can provide information about the binding partners from the protein or solvent to the radical. Previously this method has been applied to study the stable electron acceptors of the bacterial reaction centers (88, 95), as well as photosystems I and II of higher plants (95, 97). Both two-pulse and three-pulse ESEEM is used to get the information about nearby interacting nuclei, by measuring the modulation. Three-pulse ESEEM has advantages over two-pulse ESEEM, three-pulse ESEEM gives narrower lines in frequency domain spectrum and there is no interference from sum combination frequencies. In a four-pulse ESEEM the nuclear coherences evolve during the two variable time intervals t_1 and t_2 .

$$\omega_\alpha = \omega_I + A/2 + SOS \dots \dots \dots \text{Equation 4.2a}$$

$$\omega_\beta = \omega_I - A/2 + SOS \dots \dots \dots \text{Equation 4.2b}$$

When stepped under the constraint $t_1=t_2=t$, four-pulse ESEEM gives information about basic nuclear frequencies and second order shifts (SOS) corresponding to combination frequencies, which is useful in estimating weak dipolar couplings.

$$E_{4p} = (\omega_\alpha + \omega_\beta)t \dots \dots \dots \text{Equation 4.3a}$$

$$E_{4p} = (2\omega_I + 2SOS)t \dots \dots \dots \text{Equation 4.3b}$$

So any nuclei far away from the unpaired electron has ω_α and ω_β close to ω_I and the second order shifts are too small to resolve, but nuclei that are close have strong second order shifts and the length of shift of the sum frequencies is a measure of second order shifts.

4.3 Results:

4.3.1 CW-EPR

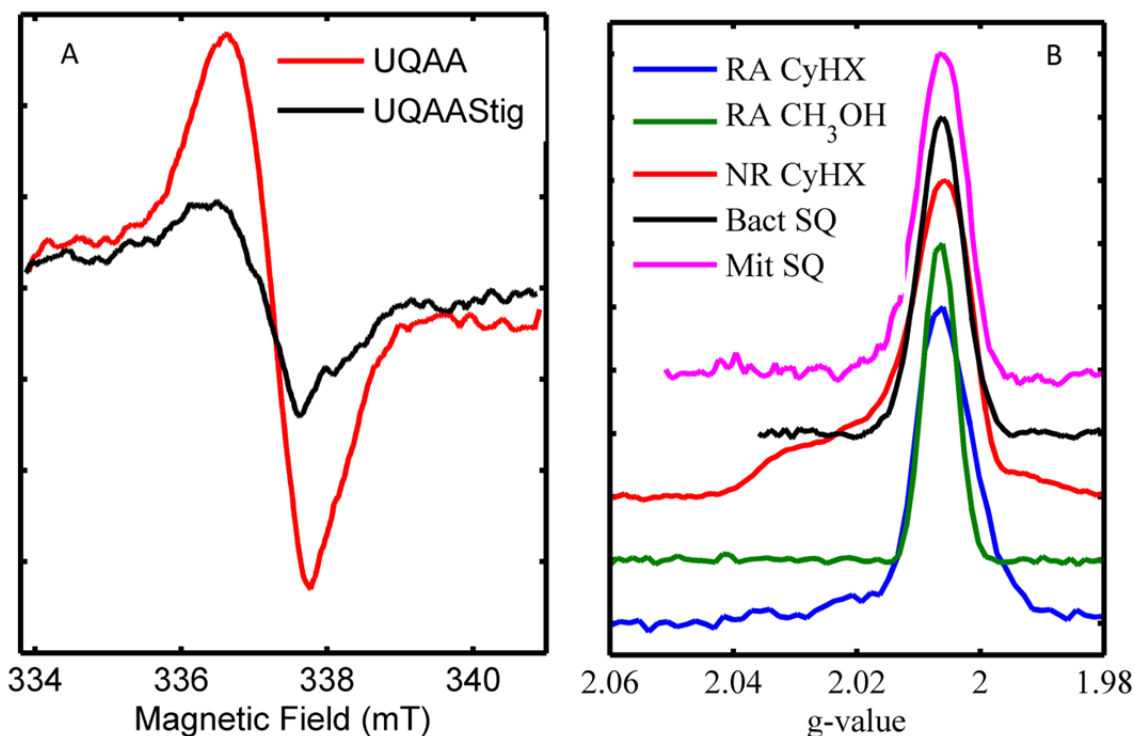


Figure 4.1 (A) CW-EPR of SQ₀. CW-EPR spectra of SQ₀ in mitochondrial cyt *bc*₁ with (red) and without (black) stigmatellin at X-band. Stig was slightly sub-stoichiometric in order to avoid a free radical signal present in many stig solutions. (B) Field swept EPR spectra of SQ radicals in different environment at X-band.

Figure 4.1 (A) is the cw-EPR spectrum of a typical anaerobic, freeze-quench sample containing 15 μM mitochondrial cyt bc_1 from *S. cerevisiae*, 100 μM UQH₂, 80 μM horse heart cyt c and 30 μM antimycin A (AA), with a 7 ms delay between mixing and freezing at 77K. The spectrum contains a single, nearly-symmetric line with g -factor ≈ 2.0044 and peak-to-peak line width of 1.16 mT. The signal is stigmatellin-sensitive and largely disappears when stigmatellin, a Q_o site inhibitor is bound in the Q_o site, red line in figure. 4.1 or when UQH₂ is absent. This signal is very similar to those reported for SQ in the Q_o site of cyt bc_1 from *R. capsulatus*, $g \approx 2.0054$, line width 1.19 mT (50) and $g \approx 2.0040$, line width 1.17 mT (54), yet distinctly broader than the signal from the quinone radical (~ 0.8 mT (98)) in the Q_i site in the absence of AA. In these experiments, AA blocks the Q_i site, preventing formation of SQ there, while preventing reoxidation (via the Q_i site) of the cyt b chain and SQ in the Q_o site after the first 1-2 turnovers. The cyt c prevents complete reduction of the high-potential chain. Stigmatellin blocks the Q_o site and prevents the initial oxidation of UQH₂ to form SQ at the Q_o site. Any residual SQ signal when stigmatellin is bound must be the result of nonenzymatic processes. Figure 4.1 (B) also compares the EPR signal of SQ_o with that of radical anion in different environment. They all have EPR signal at $g=2$ and have similar linewidths. Because it is not possible to differentiate between radical anion and neutral radical at X-band, due to poor Zeeman splitting, high-field EPR measurements would be helpful.

4.3.2 *High field and pulsed EPR*

Figure 4.2 the EPR spectra of UQ10 radical in four different environments at and W-band respectively at 40 K. These are frozen samples and represent the powder pattern with semiquinone in different orientations resulting in line broadening. All the spectra are normalized

to the peak intensity for the ease of comparison. The magnetic field at both X-band and W-band were calibrated with reference to the manganese sample, whose g-values are well documented. Easyspin was used to fit both X-band and W-band EPR spectra (99). The fits for X-band EPR spectra gave an isotropic g-value around 2.0046 with line widths varying from 1.1 to 1.2 mT and lacks

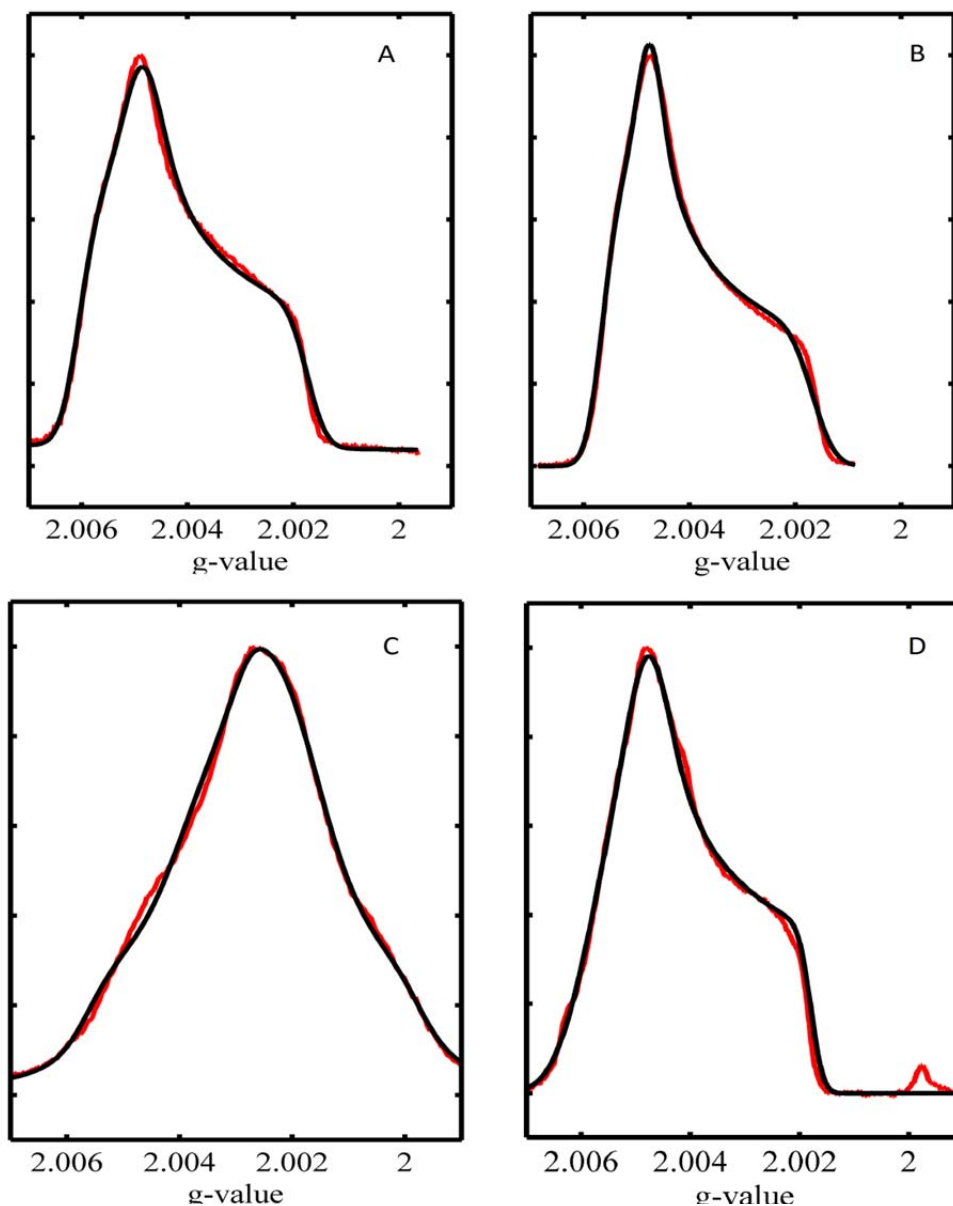


Figure 4.2 HF-EPR of SQ. High-field EPR spectra (Red) and their best fits (Black) of (A) UA radical anion in cyclohexanol, (B) UQ radical anion in cyclohexanol and methanol, (C) UQ neutral radical in cyclohexanol at 95-GHz and (D) bacterial SQ_0 at 235 GHz.

information regarding g -anisotropy due to poor resolution caused by line broadening. A way out of the resolution/line broadening problem is to investigate the radicals at high field such as W-band (95 GHz), where the increased Zeeman interaction should lead to complete separation of spectral features belonging to different g -tensor components.

Table 1 compares of g -values of UQ radicals in different solvents obtained at high field EPR. The high field (95GHz) EPR spectra of UQ radical anion in deuterated cyclohexanol and KOH gave g -values [2.00124 2.00422 2.00574], in protonated cyclohexanol and KOH gave g -values of [2.00171 2.00482 2.00604] and in protonated cyclohexanol with methanol and KOH gave g -values [2.00166 2.00474 2.00571]. The radicals produced in these three solvent are single species and they are similar to the UQ radical anion in isopropanol. Cyclohexanol is used in our work to model the hydrophobic Q_o pocket of *cyt bc₁*. Deuterated cyclohexanol has no protons to interact with the unpaired spin, protonated cyclohexanol is weakly polar but has proton spins that could appear in the ENDOR and the cyclohexanol with methanol has the possibility of forming strong H-bonds from the methanol. The slight differences in the g -values of radicals produced in those three solvents reflect the difference in the environment of the radical. In contrast to the radical anion, the EPR spectra of the radical produced in cyclohexanol and HCl does not give a good fit with single species but with two species. The sample has a mixture of two radical species with g -values [2.00199 2.00247 2.00566] and [1.99897 2.00243 2.00432] and are very different than the g -values of radical anion. The high field EPR spectra (235GHz) of bacterial SQ in the Q_o site of *cyt bc₁* from *R. capsulatus*, gave g -values [2.00147 2.00433 2.00546] and are similar to the UQ radical anion and is much different from the neutral radical. Unfortunately, high field EPR spectrum on mitochondrial SQ_o was not obtained. The high field EPR results

suggests that the bacterial trapped SQ_o is a radical anion and a more sensitive EPR technique, ENDOR is used to support this assignment, compare the bacterial and mitochondrial SQ_o and to probe the difference in the environment of the radical.

Species	g_{xx}	g_{yy}	g_{zz}	g_{iso}	ref
Qi./bc1	2.0062	2.0053	2.0022	2.00457	(100)
QH./quinol oxidase	2.00593	2.00543	2.0022	2.00452	(101)
Qa./bacterial reaction center	2.00649	2.00532	2.0021	2.00464	(102)
UQ10./isopropanol	2.00627	2.00531	2.00213	2.00457	(103)
UQ3./DME/mTHF	2.007	2.00537	2.00202	2.0048	(104)
Qo./bacterial bc1	2.00546	2.00433	2.00147	2.0037533	this work
UQ./d-cyclohexanol	2.00574	2.00422	2.00124	2.00373	this work
UQ./cyclohexanol	2.00604	2.00482	2.00171	2.00419	this work
UQ./cyclohexanol, Methanol	2.00571	2.00474	2.00166	2.0040367	this work
UQN/Cyclohexanol	2.00566	2.00247	2.00199	2.0033733	this work
	2.00432	2.00243	1.99897	2.0019067	this work

Table 1. g-values of quinone radicals.

4.3.3 Pulsed ENDOR

Pulsed ENDOR is used to further characterize the radicals produced chemically, SQ trapped in the protein and to probe the environment of the trapped SQ and chemically prepared radicals. Table 2 is the comparison of the hyperfine coupling values of SQ in protein and UQ radicals obtained chemically. Figure 4.3 and 4.4 are the X-band ENDOR spectra of UQ10 radical at 40K with the fits obtained from Easyspin (99). The fit for radical anion in deuterated cyclohexanol gave four sets of hyperfine coupling values, ([8.5, 4.8, 4.8], [5.95 3.36 3.36], [9.35 5.28 5.28] and [1.789 -1.523 -0.929]), figure 4.3. Three sets of the large coupling values

correspond to the protons of the methyl group in several different conformations. The methyl group is still rotating at this temperature, resulting in high A-strain and broad range hyperfine coupling values. Also the sample was frozen rapidly, leaving the quinone molecule in different conformations and in different orientations, which results in a broad range hyperfine coupling values. After irradiation the samples have been annealed for only 15 sec to remove the solvent radicals. This is not enough time to reach the most stable conformation of semiquinone and there is still a mixture of radicals in different conformations. The methyl couplings, although gave a good fit with three sets of coupling values, it is actually a distribution of coupling values ranging between those given values. The fourth set or smaller coupling values correspond to the protons of methoxy group substituted on the ring. Solvent protons and more distant protons of the phytyl tail of the radical also contribute to the small couplings around the proton Larmor frequency (~15 MHz). There are no large hyperfine coupling values that would be a result of strong hydrogen bonds, such as protons attached to the oxygen of the SQ ring or protons from more polar solvent. This is no surprise as the radical in KOH saturated deuterated cyclohexanol neither forms strong hydrogen bonds with polar solvent molecules nor does it have a hydrogen on the oxygen of the SQ ring, as it is a radical anion.

The fit for radical anion in protonated cyclohexanol, figure 4.3 gave five sets of hyperfine coupling values ([8.5, 4.8, 4.8], [5.95 3.36 3.36], [9.35 5.28 5.28], [4.9 -0.8 -0.8] and [1.789 - 1.523 -0.929]) and are similar to that of radical anion in deuterated cyclohexanol. Three sets (which are actually a distribution) correspond to the protons on the methyl group and the fourth set of values ([4.9 -0.8 -0.8]) correspond to the weak hydrogen bonds between solvent molecules and the oxygen of the SQ ring. The fifth or the smaller HFC values correspond to the protons on

the methoxy group and more distant protons on the phytyl chain. There is an enhancement in the weak hyperfine coupling values, which correspond to the increased contribution from the solvent protons (matrix protons).

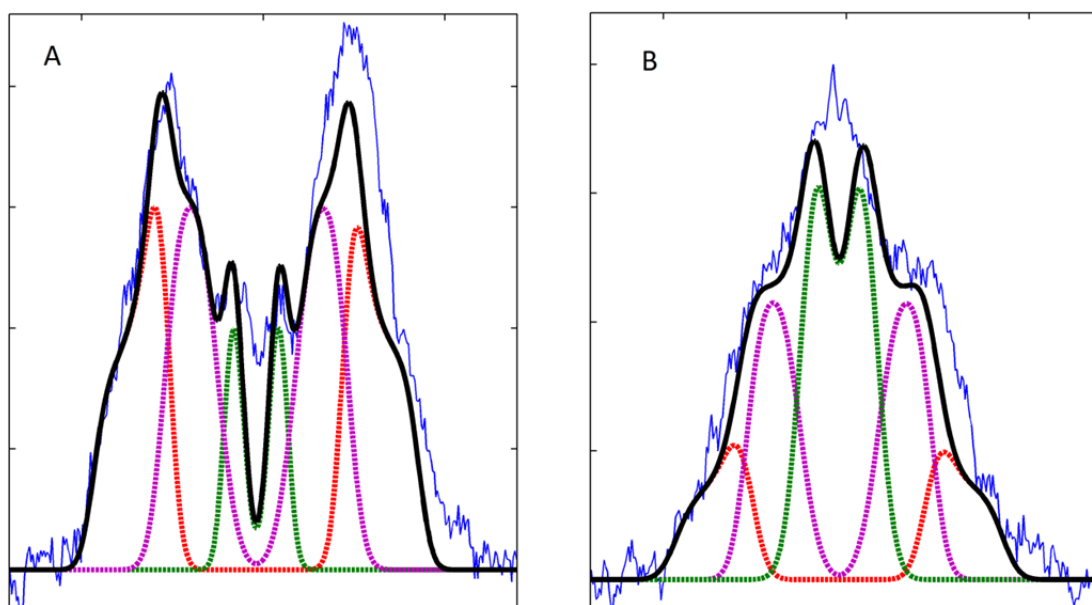


Figure 4.3 ENDOR of UQ Radical anion. Refocused Mims ENDOR spectra of UQ radical anion in deuterated cyclohexanol (A) and protonated cyclohexanol (B). The experimental spectra are in blue and the simulated spectra in black. The dashed lines in different colors represent the simulated spectra from the individual hyperfine coupling values referred in text while the black line is the sum of all the individual simulated spectra.

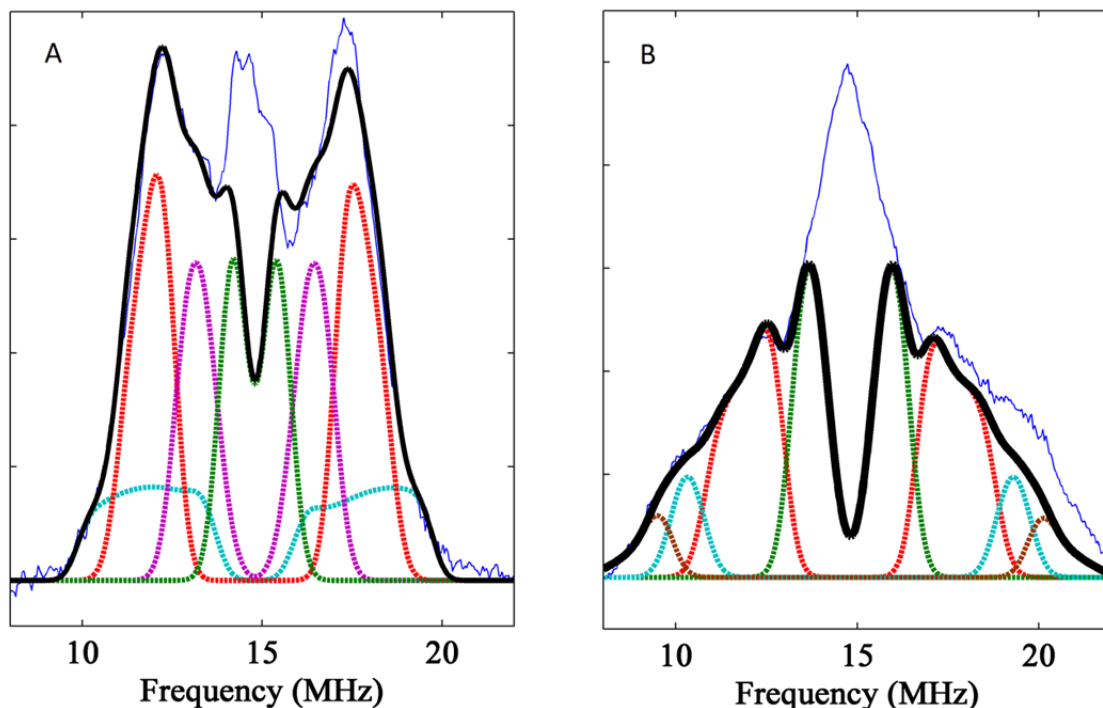


Figure 4.4 ENDOR of UQ neutral radical. Refocused Mims ENDOR spectra of UQ radical anion in methanol (A) and UQ neutral radical in cyclohexanol (B). The experimental spectra are in blue and the simulated spectra in black. The dashed lines in different colors represent the simulated spectra from the individual hyperfine coupling values referred in text while the black line is the sum of all the individual simulated spectra.

The fit for radical anion in methanol and CH_2Cl_2 gave four sets of hyperfine coupling values ([9.35 5.28 5.28], [5.95 3.36 3.36], [1.789 -1.523 -0.929] and [6 -1.33 -1.33]), figure 4.4. Two sets correspond (a distribution) to the methyl protons and third set correspond to the protons on the methoxy group. The fourth set of coupling values [6 -1.33 -1.33] are little large for methylene proton couplings of the tail and could be from the methanol protons hydrogen bonded to the oxygen of quinone.

The solution with HCl has a mixture of two different radicals. They each have a set of hyperfine coupling values that correspond to the methyl protons, protons on the oxygen of SQ ring and methylene protons from tail, figure 4.4. Two sets of large hyperfine coupling values

([14 10.2 9] and [11 -11 -11]), other two sets ([9.5 5.0 5.0] and [5.5 3.3 3.3]) lie in the range of protons of the methyl group. The fifth set ([2.057 -1.193 -0.555]) is from the protons on the methylene group of the tail. The coupling values for neutral radical have not been assigned to particular protons. But they are definitely larger and different from the coupling values obtained from the radical anion. The ENDOR line in the center, around proton Larmor frequency gives a good fit with a number of HFC values rather than a single set as mentioned in the table (5th set). These HFC values correspond to a number of protons that interact to a different extent with the unpaired spin. The ENDOR spectrum in the center has contribution from protons on the methoxy group, protons on the phytyl chain and more distant solvent protons. The neutral SQ radical has a

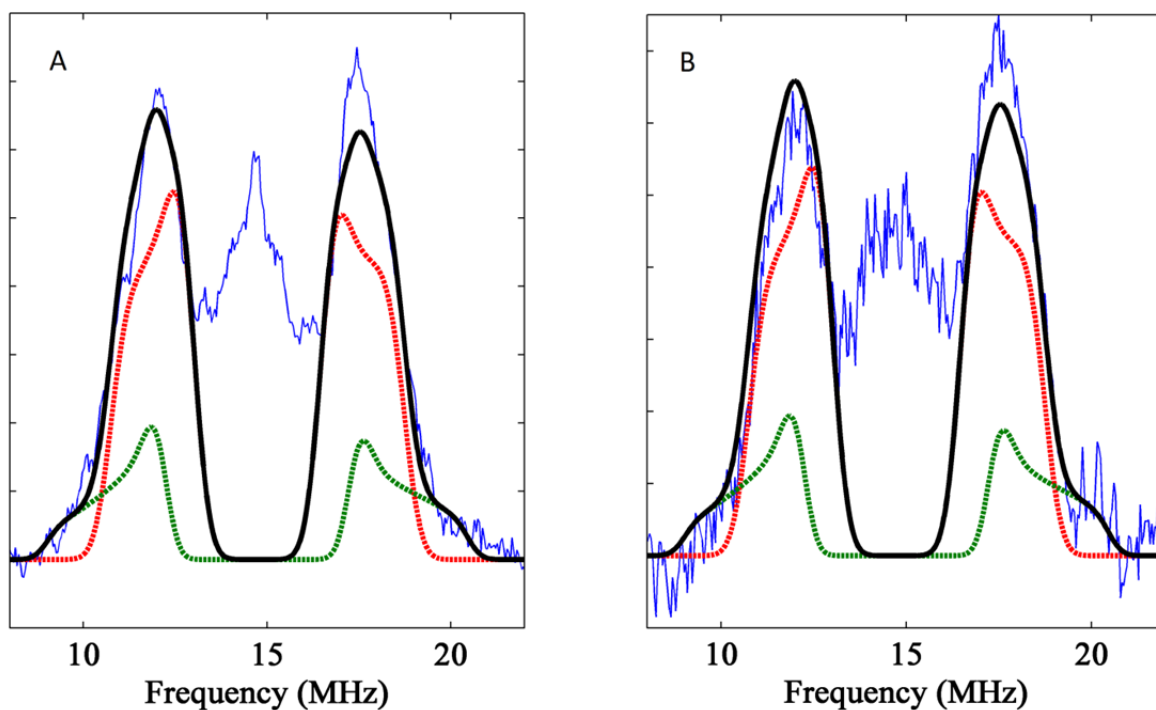


Figure 4.5 ENDOR of SQ₀ in protein. Refocused Mims ENDOR spectra of SQ₀ radical bacterial cyt *bc*₁ (A) and mitochondrial cyt *bc*₁ (B). The experimental spectra are in blue and the simulated spectra are in black. The dashed lines in different colors represent the simulated spectra from the individual hyperfine coupling values referred in text while the black line is the sum of all the individual simulated spectra.

set of large hyperfine coupling values that are not from the protons on the methyl group and are absent in the SQ radical anion.

Species	Aiso	Axial	Rhombicity	Ref
QH ⁻ in Cytochrome <i>bo</i> ₃	9.67	1.55	0.275	(105)
QA ⁻ in Zn-Bacterial Reaction Center	4.63	1.13	0.3	(106)
UQ0 ⁻ /Isopropanol	5.36	1.21	0.25	(104)
UQ3 ⁻ / Isopropanol	6.2	1.4	0	(104)
UQ10 ⁻ / Isopropanol	6.23	1.08	0.15	(107)
UQ0 ⁻ /DME/mTHF	6.03	1.23	0	(104)
UQ3 ⁻ /DME/mTHF	6.13	1.13	0	(104)
UQ10 ⁻ /DME/mTHF	6.03	1.03	0	unpub
UQ10 ⁻ /d-Cyclohexanol	4.44-6.63	0.86-1.35	0	This work
UQ10 ⁻ /Cyclohexanol	4.22-6.63	0.86-1.35	0	This work
UQ10 ⁻ /CH ₃ OH/CH ₂ Cl ₂	4.22-6.63	0.86-1.35	0	This work
SQ ₀ /Bacterial Cyt <i>bc</i> ₁	5.16	1.41	0.25	This work
SQ ₀ /Mitochondrial Cyt <i>bc</i> ₁	5.16	1.41	0.25	This work

Table 2 Hyperfine Coupling Values

The proton ENDOR spectrum of SQ in mitochondrial cyt *bc*₁ consists of a peak centered on the proton Larmor frequency of ~15 MHz from protons of the methoxy groups and from the protein with weak hyperfine couplings to the unpaired electron spin of the SQ, figure 4.5. That peak is flanked by a pair of peaks from protons with stronger hyperfine couplings. The spectrum is quite similar to that of SQ in bacterial cyt *bc*₁. The flanking peaks in both ENDOR spectra are assigned to the three protons of the 5-methyl group in the ubiquinone radical anion, while the weak tails extending 1.5 MHz beyond those peaks are assigned to a single methylene proton of the hydrocarbon tail. The ENDOR spectra from the strongly coupled protons of SQ in Q₀ of mitochondrial and bacterial cyt *bc*₁ are well simulated, using the same hyperfine tensors: (A_x, A_y, A_z) = (8.0, 4.0, 3.5) and (11.5, 5.5, 5.0) for the methyl and methylene protons respectively in

both the mitochondrial and the bacterial *cyt bc₁*. The two methylene protons of the phytyl chain are inequivalent with one large and one small coupling. The HFC value of the methylene proton depends on the dihedral angle between the plane of the SQ head group and the vector connecting C-H of the tail. This indicates that the phytyl tail is twisted out of the plane of the macrocycle of the radical, such that one proton experiences strong coupling (one out of the plane) and the other experiences negligible coupling (one parallel to the plane). The ENDOR results shows that the SQ_o trapped in both the bacterial and mitochondrial *cyt bc₁* are the same species and are in similar environment. These hyperfine couplings lie within the range reported for the ubiquinone radical anion in frozen solutions and in proteins that clearly utilize the ubiquinone radical anion, but it is about 50% smaller than the Q_H in *cyt bo₃* quinol oxidase where a controversial neutral semiquinone form has been suggested.

4.3.4 ESEEM

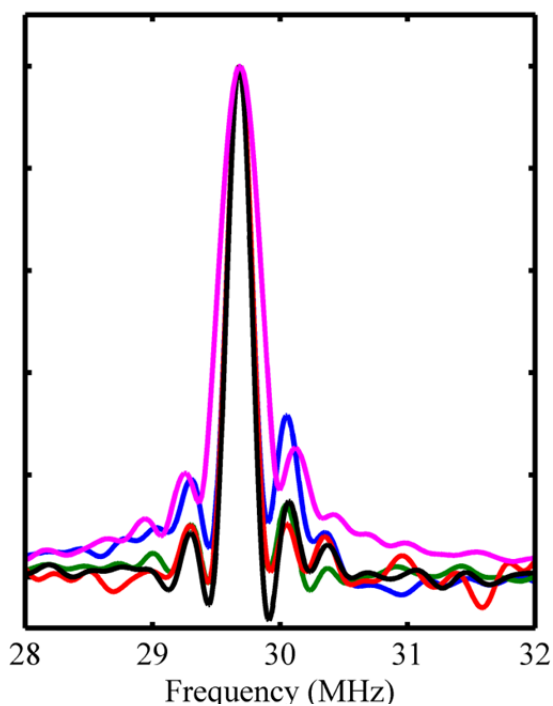


Figure 4.6 Four pulse ESEEM spectra

I searched for interactions between the SQ and protein or water using the pulsed EPR technique known as ESEEM, which is highly effective at characterizing hydrogen bonds and coordination by nitrogens from the protein. Figure 4.6 shows overlaid 4-pulse ESEEM spectrum of SQ in cyclohexanol (red), SQ in methanol (blue), SQ in cyclohexanol with trace of methanol (green), mitochondrial SQ_o (black) and bacterial SQ_o (pink). Protons with small hyperfine

anisotropy, e.g., 5-methyl, produce the strong, symmetric peak at 29.7 MHz while protons that are hydrogen bonded to SQ have a large anisotropy and are shifted 0.3-0.9 MHz to higher frequency and destroy the symmetry of the spectrum. UQ radical anion in cyclohexanol, more sterically hindered solvent, does not have significant hydrogen bonds with the solvent, and is evident from the lack of asymmetry in the spectrum around 30.0 MHz. UQ radical anion in frozen methanol/dichloromethane has hydrogen bonding to the methanol solvent, as shown by an asymmetric spectrum with extra intensity from 29.9-30.3 MHz. The spectrum of mitochondrial SQ₀ in the *S. cerevisiae* and bacterial SQ₀ from *R. capsulatus* are quite symmetric in that region, showing minor, if any, hydrogen bonding. There is no evidence of protons hydrogen bonded to SQ₀ trapped in cyt *bc*₁ unlike in other proteins.

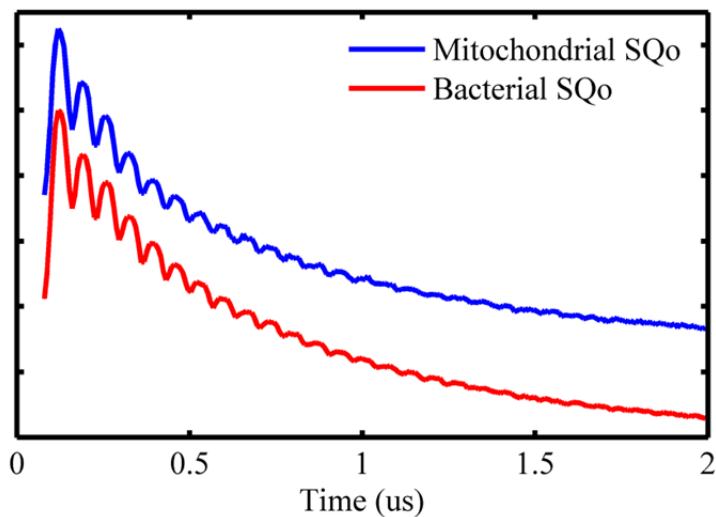


Figure 4.7 Two-pulse ESEEM spectra of SQ₀

The 2- and 3-pulse ESEEM spectra of SQ₀ in both bacterial and mitochondrial cyt *bc*₁ were carefully examined and universally lack the characteristic, low-frequency signals from coordination of SQ₀ to protein Nitrogen found in virtually every other reported SQ-containing protein. Figure

4.7 is the overlaid time-domain 2PESEEM spectrum of SQ₀ trapped in mitochondrial and bacterial cyt *bc*₁. There is no strong low frequency modulation in the time domain spectra and the only modulation is from the protons, and there are no peaks in the range 0-4 MHz where a tightly bound nitrogen could be

seen. The absence of any low frequency modulation suggests that the SQ_o is not coordinated to Nitrogen of either histidine or peptide backbone. The 3-pulse ESEEM is an effective tool to measure any hydrogen bonds between paramagnetic species and the protein. 3-pulse ESEEM spectrum of SQ_o trapped in mitochondrial and bacterial cyt *bc₁*, and lacks the low frequency modulation which suggests that the SQ_o is not hydrogen bonded to nitrogen of either histidine or peptide backbone. These two unexpected observations indicate that SQ is neither coordinated nor bound by nitrogens from sidechains or the peptide backbone of the protein nor are there hydrogen bond to the terminal oxygens.

4.4 Discussion:

4.4.1 Nature of SQ_o and its interaction with protein:

To our knowledge, no crystal structures of cyt *bc₁* complexes have been solved with quinol bound in the Q_o pocket. Most previous work uses the reasonable default assumption that QH₂ binds similarly to stig, which appears in the structures to be strongly hydrogen bonded to the imidazole of H181 of the ISP and the glutamyl of E272 of cyt *b*. (108) The spectroscopic characterization of the anionic trapped SQ_o shows several remarkable features that we propose are related to its function.

The *g*-anisotropy from high field EPR results confirms that the radical trapped in bacterial cyt *bc₁* is a radical anion and not a neutral radical. The lack of large hyperfine couplings in the ENDOR spectrum of SQ in bacterial and mitochondrial cyt *bc₁* also confirms that they are radical anions, trapped in a non-polar pocket. The extremely similar ENDOR spectra of SQ in bacterial and mitochondrial cyt *bc₁* indicate that the SQ species are the same and are in a similar environment. The methyl coupling values of SQ in bacterial and mitochondrial cyt *bc₁* matches

well with the other reported SQ radical anion in different proteins. The ENDOR spectra and 4-pulse ESEEM lack any evidence for hydrogen bonding between SQ and the protein, both in mitochondrial and bacterial *cyt bc₁*. This provides further evidence that the SQ is trapped in a rather non-polar pocket where there is no access for water molecules and where the SQ forms no hydrogen bonds with the protein itself.

Most enzymes are thought to work by stabilizing activated intermediates, and the Q_o site might be thought to stabilize its intermediates including SQ_o and lower the free energy of those intermediates. Indeed this strategy can prevent bypass reactions by making the reaction of SQ_o with O₂, or other oxidants or reductants, energetically uphill process. The SQ is stabilized in many redox enzymes, including the Q_i site of the *cyt bc₁* complexes, the Q_B site of photosystem II and bacterial reaction centers, and the Q_H binding sites of the *cyt bo₃* oxidase. In these examples, the SQ is rendered so stable that it can be readily observed by EPR over extended times, often even under aerobic conditions.

In thermodynamic terms, such stabilization requires tighter binding of SQ_o than Q and QH₂ to the protein and has been confirmed in several proteins, where a stabilized SQ is formed. Dikanov et al., have observed a strong hydrogen bond between Q_H SQ of *cyt bo₃* and a nitrogen donor from protein (109). The Q_B SQ of bacterial reaction center was observed to form multiple hydrogen bonds with the protein. The strongest hydrogen bond is between O₄ (carbonyl) of SQ and His-L190 NH. The SQ was also observed to form hydrogen bonds with Gly-L225 peptide NH, Ser-L223 hydroxyl OH Ile-L224 peptide NH (110).

The 2-pulse and the 3-pulse ESEEM spectra of SQ_o in *cyt bc₁* are highly unusual in their lack of detectable ESEEM from nitrogen or strong H-bonds, indicating that the interactions of

the trapped SQ_o are distinct from those of stig. This lack of strong interactions with the protein is unique among previously-characterized UQ radicals which show prominent ESEEM from amino acid side chain or peptide nitrogens and hydrogen-bonded protons to oxygens of the UQ (111-114).

The lack of H-bonding to the anionic SQ_o implies the following: 1) oxidation of QH₂ occurs in a catalytic complex coordinated with both electron and H⁺ acceptors, allowing the removal of one electron and two protons, forming the SQ anion. A reasonable model for this catalytic complex, proposed earlier, places the QH₂ near the binding position of stig, H-bonded to both H181 and E272; 2) Formation of SQ_o is followed by conformational changes, either moving SQ or protein components, thus breaking potential hydrogen bonds.

Alternatively, it can also imply that the SQ_o in *cyt bc₁* might not be stabilized and even be destabilized. The destabilized SQ can react with oxygen rapidly and form more SO. However the destabilized SQ is more difficult to form and this limits the formation of SO, as the greatest rate of SO production would be expected from a significant concentration of a reasonably reactive SQ rather than a small concentration of highly reactive SQ. Although the destabilized SQ model also limits the overall rate of productive Q-cycle reactions, also suppresses the unwanted bypass reactions.

CHAPTER 5

DETERMINATION OF SQ LOCATION IN CYTOCHROME *bc₁*

The importance and relevance of the SQ depends on its location in cyt *bc₁*. From the ESEEM and ENDOR results it was clear that the SQ_o is negatively charged and is destabilized in the protein. However, it is not clear how the enzyme does that. The knowledge of SQ binding site or the physical location of SQ in the Q_o pocket along with some molecular modeling would help us understand the ‘counterintuitive’ destabilized model. Here is an attempt to identify the physical location of the SQ_o and possible binding sites, by observing the spin relaxation of the SQ_o. The spin relaxation of SQ in the bacterial protein is strongly enhanced by the hemes in the system (53) and this interaction is termed as paramagnetic relaxation enhancement (PRE). I examined this PRE in detail in the mitochondrial cyt *bc₁* because PRE has been a useful probe for measuring distances between spins in proteins (57, 58) including the Fe₂S₂-heme *b_L* distance in cyt *bc₁* by Sarewicz, *et al.* (59), copper ion bound to cyt *b_{6f}* (60), cyt *c* bound to cyt *c* oxidase (61), and spin-labeled metmyoglobin (62).

One of the most sensitive spectroscopic methods that measure the interaction of two paramagnetic centers is to measure the impact of a fast relaxing metal on the relaxation of slow relaxing species. The enhancement of relaxation of slow relaxing species is a resonance like effect and the temperature of maximum rate of relaxation of slow relaxing species is where the

relaxation rate of fast relaxing spin ($1/T_I$) is equal to the dipolar interaction between two paramagnetic species. The higher the maximum $1/T_M$ temperature, stronger is the dipolar strength and smaller the distance between two paramagnetic species. The dipolar relaxation enhancement has a very specific dependence on $1/T_I$ of the fast relaxing spin. As T_I is strongly temperature dependent, dipolar relaxation also depends strongly on temperature. The magnetic interaction between two paramagnetic centers decreases with sixth power as the distance between centers increases. The dipolar coupling also depends on the angle between dipolar vector, connecting two paramagnetic species and external magnetic field (θ_D).

5.1 Enhanced Spin Relaxation of SQ Generated at the Q_o Site.

Cape et al., have measured the effect of added paramagnetic Ni(II) on cw-EPR power saturation to probe the accessibility of SQ species to paramagnetic ions in the aqueous phase of the freeze-quenched samples, to estimate how deeply is the SQ buried in the membrane or protein (50). The CW-EPR saturation recovery measurement is a way to measure the magnetic interactions between two or more paramagnetic species. If a slow relaxing paramagnetic species is near a fast relaxing paramagnetic species, the relaxation rate of slow relaxing species increases, and also the saturation power (amount of MW power to saturate the spins in one state). The freeze-quenched SQ species with only AA has small or no effect on the power saturation when the paramagnetic Ni⁺² was added, whereas the SQ species with both AA and stig showed a prominent increase in power saturation when the paramagnetic Ni⁺² was added. This shows that the SQ generated using AA has no magnetic interactions with Ni and is far and protected from Ni⁺² in aqueous phase, and the small amount of SQ generated using AA and stig has strong interactions with Ni⁺² and is close to the Ni⁺² in aqueous phase. This indicates that the SQ

generated using AA is trapped inside the protein, where there is no access to the aqueous phase, but it could be anywhere in the vast protein.

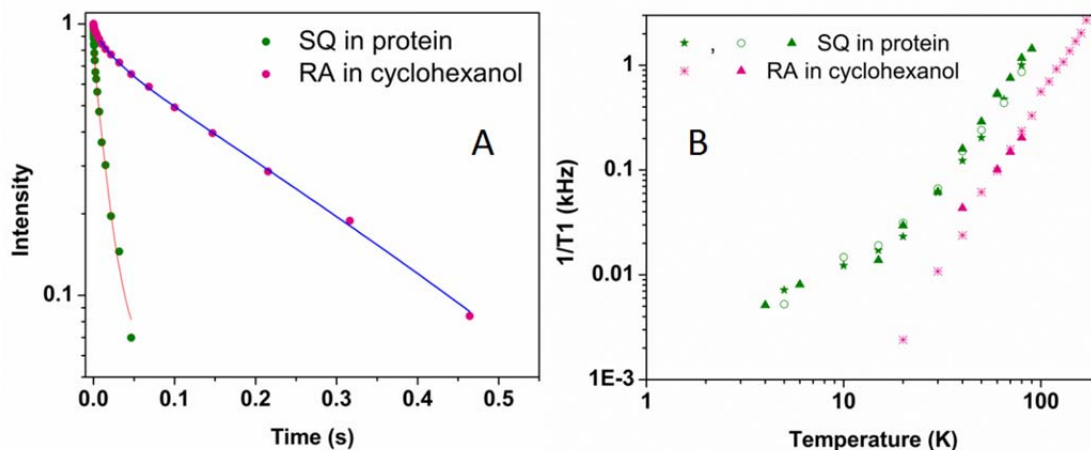


Figure 5.1 T_1 relaxation of SQ radical anion and SQ_0 . Comparison of inversion recovery of SQ_0 in mitochondrial *cyt bc_1* to SQ radical anion in cyclohexanol. Semi-log plot of T_1 relaxation of mitochondrial SQ_0 and UQ radical anion (A) and comparison of effect of temperature on $1/T_1$ on both mitochondrial SQ_0 and SQ radical anion in solution (B).

As a measure to know where the SQ is trapped, a series of pulsed EPR techniques were used which provide a better tool to measure the magnetic interactions between species, on freeze-quenched mitochondrial SQ species in presence of AA of yeast *cyt bc_1*. Same series of experiments were done on chemically prepared SQ species in cyclohexanol and compared to the freeze-quenched SQ species. As a first approach, T_1 relaxation of SQ trapped in mitochondrial *cyt bc_1* and the SQ radical anion in cyclohexanol were measured as a function of temperature using picket fence inversion recovery experiment. Figure 5.1 is the comparison of inversion recovery of SQ in mitochondrial *cyt bc_1* and the SQ radical anion in cyclohexanol as a function of temperature. The SQ in *cyt bc_1* complex recovered fully in 10 μ s, while the SQ radical anion in solution took 100 μ s to recover, 10 times longer than the recovery time for SQ in protein. Figure

5.1A is the semi-log plot of T_1 relaxation. Figure 5.1B shows the effect of temperature on the T_1 relaxation rate, on both SQ in cyt bc_1 and SQ radical anion in solution.

The SQ trapped in mitochondrial cyt bc_1 has much shorter T_1 and high spin relaxation rate at all temperatures than that of SQ radical anion in cyclohexanol, and about 10 times than the relaxation rate of SQ in solution at 40K, which indicates that the SQ in protein has strong magnetic interactions with another fast relaxing paramagnetic species like oxidized heme b_L or reduced Fe_2S_2 cluster because, the low-spin Fe in heme b_L is paramagnetic only when the heme is in oxidized state and the high spin Fe of Fe_2S_2 cluster is paramagnetic when it is in reduced state. This result supports the results of Cape et al., that the SQ trapped in protein in presence of AA is not in the solution and is buried deep inside the protein where it is close enough to the oxidized heme or reduced Fe_2S_2 or both.

There are six hemes and two Fe_2S_2 clusters in the dimeric protein and the SQ could be trapped anywhere in the protein. It is impossible to locate the location of trapped SQ in protein with T_1 measurements. The T_1 relaxation enhancement measurement is very effective tool to measure the distance between two spins, but is very complicated to analyze in our system. For one thing, the heme, Rieske and SQ signals overlap each other in our system making it difficult to measure T_1 of single species. The other reason is that the T_1 is highly dependent on the g-tensor and the orientation of SQ with respect to 'Fe' center, in a powder sample like freeze-quenched bc_1 it is very complicated to analyze the T_1 data. The transverse, T_2 or T_M relaxation measurements give a direct measure of the magnetic dipolar interaction between two paramagnetic species. The enhancement varies with the temperature of the sample because the enhancement depends on the interplay of the dipolar interaction between spins and the

temperature-dependent T_1 and T_2 of the ‘enhancer’ spin. The effect has been used to measure the distance between spins in a number of proteins (57, 58). Sarewicz et al. have studied the interaction between Fe_2S_2 cluster and heme b_L of cyt bc_1 that takes place within the range of 2.6-3.6 nm. They studied Fe_2S_2 head group motion by comparing the temperature dependence of phase relaxation rate of the Fe_2S_2 cluster in native cyt bc_1 complex in presence of various inhibitors to understand the equilibrium distribution of Fe_2S_2 position in cyt bc_1 . The $1/T_M$ of the dithionate reduced bc_1 (which has reduced heme) has monotonic temperature dependence, whereas the ascorbate reduced bc_1 (which has oxidized heme) has a maximum $1/T_M$ at 19K. This shows that the oxidized heme b_L induces PRE on Fe_2S_2 echo decay. Prisner et al., have studied the interaction between two electron transfer proteins, which form a transient protein-protein complex (61). They studied the dipole-dipole interaction between Cu_A of cyt c oxidase heme Fe^{+3} of different cytochromes. The T_M echo of mixture of CcO_{II} with binding cytochromes like horse heart cyt c (c_{hh}) and cyt c_{552} relaxes much faster than mixture of CcO_{II} with a non-binding cyt c_1 . This is because that the distance between the two paramagnetic centers for specifically bound protein-protein complexes is much shorter than the average intermolecular distance between randomly distributed paramagnetic centers. PRE is an effective tool to distinguish binding and non-binding proteins. Kramer et al. studied the effect of redox state of cyt b_{6f} on the two-pulse echo decay of the bound Cu^{+2} (31). The PRE was used to calculate the distance between the cyt f heme and bound Cu^{+2} to locate the Cu^{+2} binding site in cyt b_{6f} , and study the conformational changes that occur at the Q_o site of cyt b_{6f} .

The phase relaxation time (T_M) of SQ has been measured as a function of temperature to calculate the dipolar interaction and distance between SQ and fast relaxing Fe center in protein.

The phase relaxation time of SQ in cyclohexanol was measured and compared to SQ in protein. T_M of SQ in cyclohexanol has a weak dependence on temperature whereas T_M of SQ in protein has strong temperature dependence and has a maximum rate of decay at 35 K (figure 5.2 A). The T_M relaxation of SQ in mitochondrial cyt bc_1 is 10 times the T_M relaxation rate of SQ in cyclohexanol at 40 K. The temperature dependence of $1/T_M$ of SQ in protein is distinctly non-exponential as noted for the analogous enhancement of the Fe_2S_2 cluster by heme b_L (59). Sarewicz et al., has used a stretched exponential function to fit the dipolar decay trace to get the $1/T_M$ term. They got a maximum of $1/T_M$ at 19 K (figure 5.2 B) that corresponds to a distance of 2.64 nm between heme b_L and Fe_2S_2 . When I used a similar stretched exponential function to

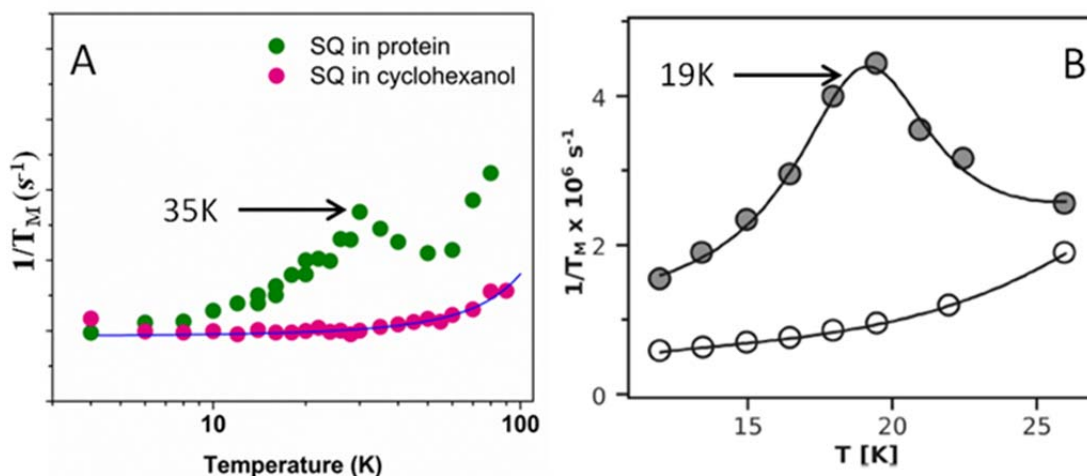


Figure 5.2 T_2 relaxation enhancement of SQ_0 and SQ in solution. Comparison of the temperature dependence of T_2 relaxation rate of (A) mitochondrial SQ_0 and SQ in solution and (B) dithionate-reduced (open circles) and ascorbate-reduced (closed circles) cyt bc_1 .

calculate the $1/T_M$ for SQ trapped in cyt bc_1 , I got a maximum $1/T_M$ at 35 K. As the maximum $1/T_M$ corresponds to a temperature where $1/T_{lf}$ equals the dipolar coupling, the higher temperature of maximum $1/T_M$ indicates a stronger dipolar interaction and a shorter distance between the spins. This suggests that the trapped SQ in cyt bc_1 is at shorter distance from heme

b_L than the Fe_2S_2 , and could be trapped somewhere between heme b_L and Fe_2S_2 . However the stretched exponential fit does not give the accurate dipolar coupling between the spins, a more complex analysis is necessary.

5.2 Analysis of T_M data

The 2P ESE (T_2/T_M) echo decay as a function of temperature was analyzed using a home written MATLAB (the mathworks) program (T_M Dipole) to extract the dipolar interaction and the distance between the two spins. T_M Dipole program calculates the dipolar relaxation enhancement induced by the interaction from multiple fast relaxing spins at any given frequency and field. The code for the T_M Dipole with its subprograms is given in appendix A with detailed explanation at each step. The cyt bc_1 complex has a broad EPR signal composed of several species, ranging from $g \approx 1.5$ to $g \approx 4$. The SQ trapped in cyt bc_1 has a narrow signal at $g \approx 2$ which overlaps the broad background signal of the Rieske, hemes and cavity. This complicates the analysis of the T_2 decay of SQ as there is a signal from background all the time. Fortunately the T_1 relaxation of the background is much faster than that of SQ, which allowed us to measure the T_2 relaxation of the background by pulsing fast and suppressing the SQ signal. The T_2 echo decay of the background was observed to be very different from the T_2 decay of SQ and was temperature independent. But the intensity of the background signal decreased with temperature and was negligible at temperatures above 50 K. The T_2 decay rate of background was similar between samples at all temperatures, but the intensity of background differs from sample to sample. Before using the T_M Dipole to calculate the dipolar enhancement, the temperature dependence of the background was calculated using 2-pulse field-sweep experiment data for each sample and the respective temperature dependence was used in simulation.

The sub program, MakeDecay calculates the dipole relaxation enhancement due to one fast relaxing spin. The cyt *bc₁* complex has multiple hemes and Fe₂S₂ clusters all of which could contribute to the paramagnetic relaxation enhancement. The simulation T_MDipole program can calculate PRE from a single fast relaxing species and as well as multiple fast relaxing species. The simulation program performs the following steps, also shown as a schematic.

First step: T_2 experimental data of SQ at multiple temperatures as well as reference spectrum and background spectrum were imported, phased and normalized per number of averages. The experimental parameters such as temperature, field and frequency at which the T_2 decay was collected, were pulled from the raw datasets. The g -values and the Euler angles of the enhancer spin/fast relaxing spin could be provided.

Second step: The background signal was subtracted from the SQ signal using a temperature dependence previously calculated for the particular sample. The T_1 relaxation rate ($1/T_1$) as a function of experimental temperature was calculated based on the published T_1 of heme from (115).

Step 3: The effective g -value of the fast relaxing spin was calculated using the g -values provided in step 1. The dipolar interaction was pre-calculated for all angles between the dipolar vector and lab field.

Step 4: The dipolar relaxation enhancement was calculated using the dipolar coupling calculated in step 5 using the theory developed by Salikhov (116) and the $1/T_1$ provided in step 2.

The fit program follows the same procedure, adjusting the fit parameters used for calculation of the dipolar coupling in step 4 within the boundaries given by the user to minimize

the chi-square between fits and experimental data. The only adjustable parameters in the program are the distance(s) between slow relaxing spin and the fast relaxing spins(s) and the amount(s) of fast relaxing spin in paramagnetic state that could contribute to the dipolar interaction and $1/T_1$ of fast relaxing spin. These parameters can be varied independent of each other to reduce the chi-square, using a Levenberg-Marquardt least square fitting. The actual chi-square was calculated using the formula below:

$$\chi^2 = \sum_{i=1}^N \left(\frac{y_i - y(x_i)}{\sigma_i} \right)^2 \dots \dots \dots \text{Equation 5.1}$$

5.2.1 Sensitivity of T_M Dipole to distance:

T_M decay is highly temperature dependent and a maximum in $1/T_M$ occurs when the dipolar interaction between two spins equals the $1/T_1$ of fast relaxing spin. For a given distance, $1/T_M$ is maximum at a temperature when Δ_{Dip} equals the $1/T_{1f}$ and is smaller both above and below that resonant temperature. This resonance can be seen as a fold over in T_2 relaxation when plotted as a function of temperature.

Figure 5.3 A-F shows the effect of temperature and $1/T_{1f}$ on the T_M relaxation rate at different distances. Figure 5.3 A, C, E are plots of calculated T_2 relaxation as a function of temperature at a given $1/T_{1f}$ ($1/T_{1f}(\text{KHz}) = 0.0000221 * \text{Temp}^{6.64}$) and a distance of 1 nm (A), 2 nm (C) and 3 nm (E). The maximum relaxation and the fold over occurred between 32 K and 28 K for 1 nm, 28 K and 24 K for 2 nm and 24 K and 20 K for 3 nm. Figure 5.3 B, D, F are plots of calculated T_2 relaxation as a function of temperature at a given $1/T_{1f}$ ($1/T_{1f}(\text{KHz}) = 0.0000221 * \text{Temp}^{7.64}$) and a distance of 1 nm (B), 2 nm (D) and 3 nm (F). Using a $1/T_{1f}$ in which the temperature dependence has been increased by a magnitude does not result in any fold

over in the given temperature and distance range. This shows that the simulation program is extremely sensitive to the $1/T_{1f}$ and most accurate $1/T_{1f}$ should be used to calculate dipolar decay.

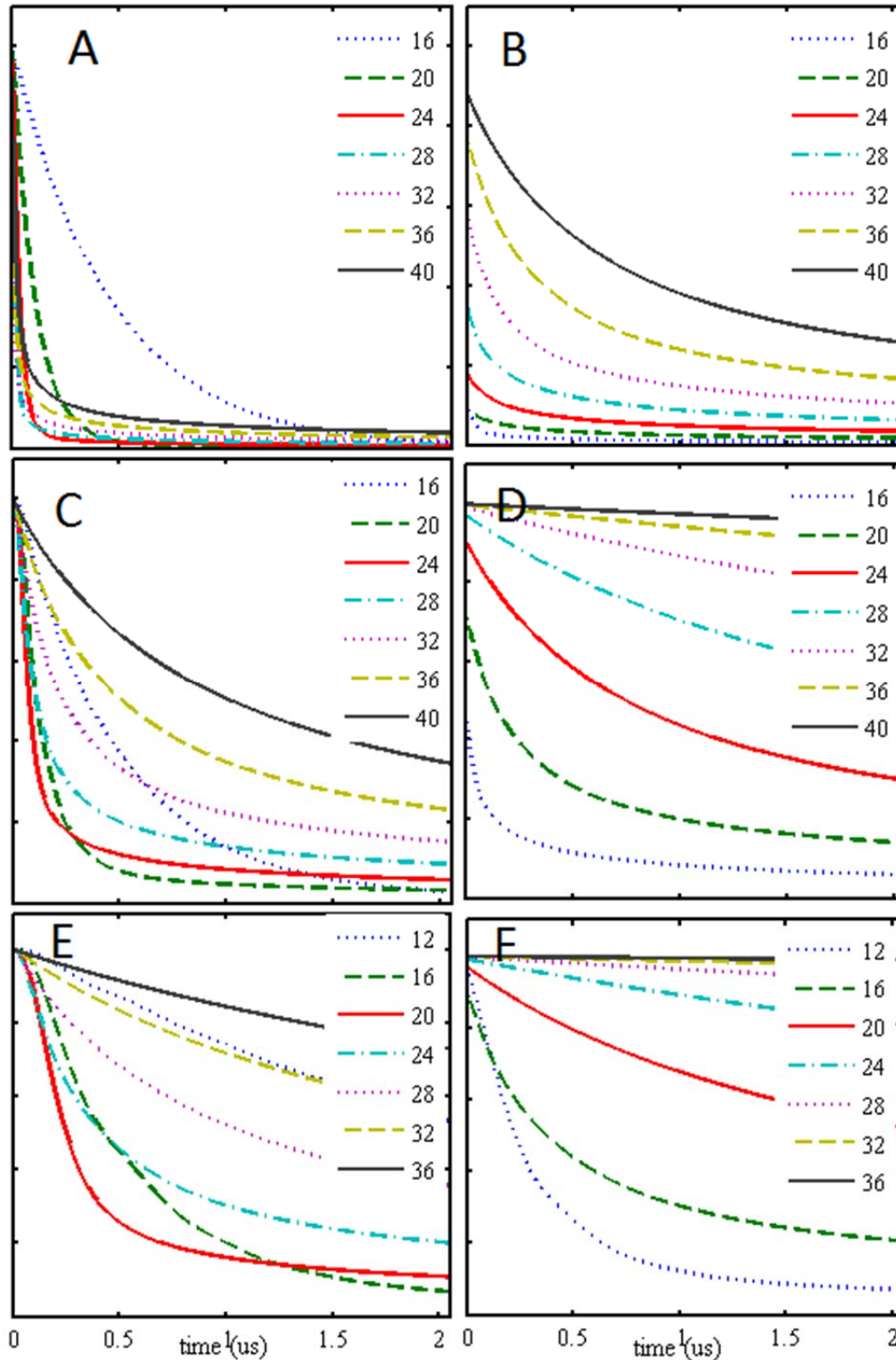


Figure 5.3 Effect of temperature and T_1 on T_2

5.3 Determination of the Location of SQ.

5.3.1 *Determining distance between SQ and Hemes from EPR experiemnts*

These freeze-quenched samples do present two novel aspects in their analysis. The redox or spin states of the hemes and Fe_2S_2 cluster near the SQ are heterogeneous. In addition, the relaxation enhancement of SQ can have contributions from more than one spin centers. Fortunately, both are readily resolved. Each *cyt bc₁* dimer contains six hemes and two Fe_2S_2 clusters and may bind two soluble *cyt c* with additional hemes. Each heme and Fe_2S_2 cluster has a paramagnetic state which interacts with and enhances spin relaxation of any SQ retained in the *cyt bc₁*. Before addition of substrate, the *cyt bc₁* is completely oxidized with all hemes in their paramagnetic state with a single unpaired electron and the Fe_2S_2 cluster in a diamagnetic state with no net electron spin. After rapid freezing, if only one electron had entered the low-potential chain, it could be localized on either of the hemes in the low-potential chain, leaving the other heme with an unpaired electron spin and the potential for enhancing the relaxation of SQ. Similarly, each part of the high-potential chain has some probability to have an unpaired electron spin. SQ trapped in Q_o can have a number of different arrangements of electron spins around it. The overall relaxation of SQ will be the weighted sum of each of those arrangements.

Many of the potential arrangements have more than one electron spin to enhance the relaxation of SQ. Because the spin dynamics of the hemes and Fe_2S_2 clusters are uncorrelated, the enhanced relaxation of SQ is just the product of the enhanced relaxation from each individual heme or Fe_2S_2 cluster. The ability to calculate the relaxation enhancement allows use of least-squares fitting methods to determine the location of SQ in *cyt bc₁* based on its distance to hemes in the complex.

The Fe_2S_2 cluster relaxes much more slowly than the hemes and can make only a negligible contribution to the total relaxation enhancement. The Fe_2S_2 was therefore omitted from the fitting procedure. The hemes from cyt *b*, cyt *c₁* and cyt *c* have overlapping spectra, making it difficult to determine the T_1 of any specific heme in the intact cyt *bc₁*. Fortunately, the T_1 rates for the hemes are within a factor of two above 10 K, which perturbs the fitted distances by $\sim 6\%$, so the T_1 of the heme system that matches well with the cyt *bc₁* is used in the final fitting (115).

The upper limit for relaxation enhancement of T_M is set by the dipolar interaction and occurs roughly at the temperature where the dipolar interaction equals the T_1 rate of the enhancing spin (60). The relaxation enhancement of SQ at each temperature is non-exponential, due in part to the paramagnetic states in each cyt *bc₁*, and could not be described consistently by exponential (60) or stretched-exponential functions (59). Consequently, the T_M relaxation curves for SQ from 4-60 K were fitted taking into account the paramagnetic states in each cyt *bc₁*. The relaxation was measured using quadrature detection which provided an independent measure of experimental noise for each curve and allowed the calculation of a true χ^2 for the goodness of the overall fit.

There are slight off sets in the fits due to the cutoff of part of the decay in the beginning corresponding to the spectrometer dead time. A large portion of dipolar enhanced relaxations takes place in this dead time and hence reduces the echo amplitude. A part of the offset might also be due to the absence of SQ radical trapped in protein, not all of the protein used can trap SQ or have heme and/or ISP in paramagnetic state. Another important contributor for the offset is the orientation of ISP cluster with respect to heme and SQ. The dipolar decay of SQ in protein

not only is affected by the heme distance but also by the orientation of ISP with respect to heme. In frozen samples, the dipolar decay is the sum of decays caused by all orientations like in powder pattern. This is taken in to account in our modeling program by averaging over all possible orientations that are in resonance. Temperature dependence of the echo decay for SQ in solution has no dipolar relaxation enhancement. The decay curves are mono exponential at all temperatures and do not show any pronounced effect with temperature

Exhaustive attempts were made to fit the relaxation enhancement of SQ without success based on interaction with a single heme site with the distance between SQ and the heme, and the fraction of heme in the paramagnetic state as adjustable parameters. The fits failed to give good agreement with the measured SQ relaxation over the full temperature range. The χ^2 values show that the difference between the fit and the observed relaxation enhancement is much more than the experimental noise. This indicates that the relaxation enhancement is produced by interaction with more than one heme.

The relaxation enhancement was fitted based on interactions with two hemes using four adjustable parameters: the distances between SQ and each heme, and the fraction of each heme in its paramagnetic state. The spin states of the two hemes were independent of each other. The best fit with two hemes gave much better χ^2 value. A surface plot and contours of $\Delta\chi^2$ as a function of distance to the two hemes in two different samples, figure 5.4 A, C shows a well-defined global minimum for distances of 1.9 nm and 3.9 nm and with 30% and 30% of the hemes in their paramagnetic state, respectively. These distances are from the center of the unpaired electron spin distribution of SQ to the iron which carries the unpaired electron spin at the center of each heme. The 95% and 99% confidence contours for the distances, figure 5.4 B, D are very

tight and consistent between different samples. Repeated fits with heme T_I values within the observed range gave distances to the hemes that varied ± 0.2 nm, comparable to the size of a quinone or amino acid. The SQ appears to be trapped by rapid freeze-quench in a well-defined location that is 1.65-1.95 nm from the iron of one heme and 2.55-3.00 nm from that of another.

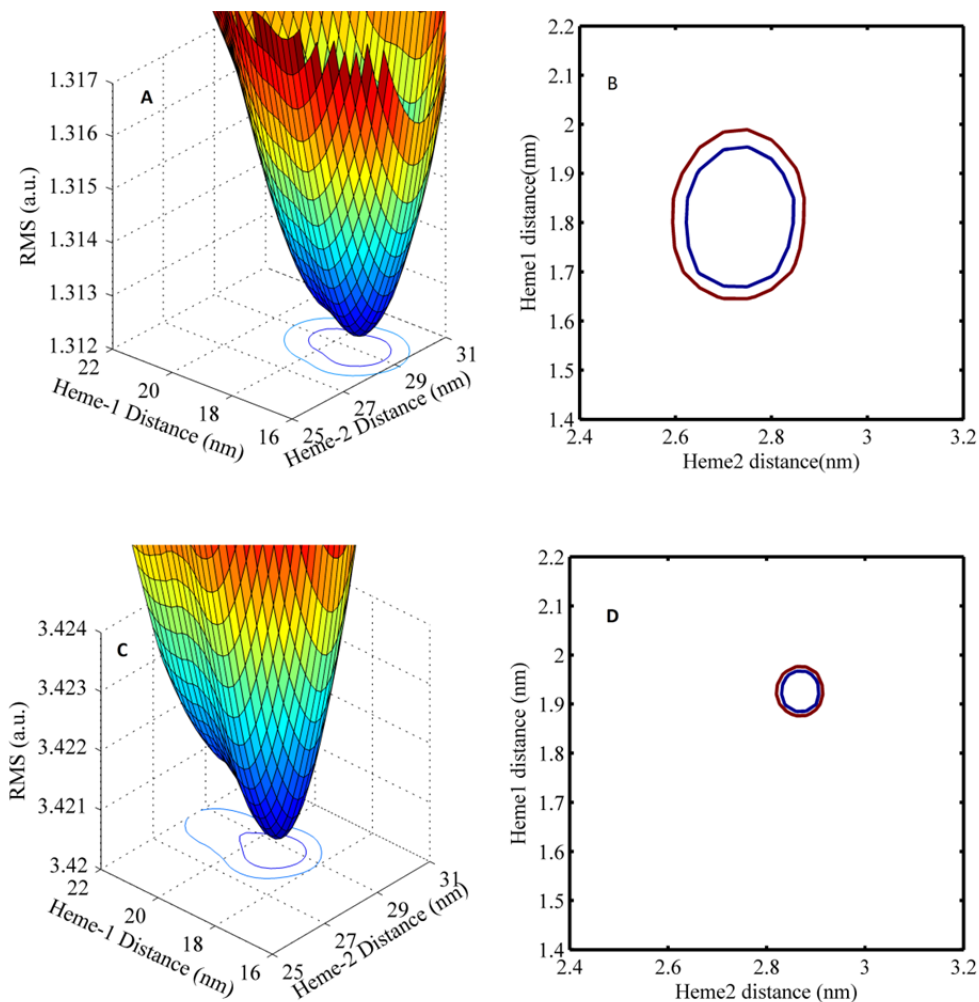


Figure 5.4 Distance constraints of SQ₀ obtained from T₂ data analysis. Plot of χ^2 as a function of distance from two hemes, when 30% of both interacting hemes are paramagnetic in two different samples (A) and (C). Heme 1 is the near heme and heme 2 is the far heme. The χ^2 is calculated from the residuals of experimental data and the fits. (B) and (D) are the 95% (inner line) and 99% (outer line) confidence interval (CI) of the distance between SQ trapped and two hemes, for two different data sets.

All the cyt b_H should be reduced after 10 ms of Q_0 site turnover and thus lack the electron spin, but cyt b_L and/or cyt c_1 could be the source of the PRE. In order to identify potential trapping sites for the SQ we searched for voids in the crystal structure of yeast cyt bc_1 (PDB: 3CX5) consistent with the PRE distance ranges to the two nearest hemes. The only locations meeting these constraints lie in the region of the Q_0 site (figure 5.5) distinct from the binding sites for known inhibitors, such as stig, which binds in the “distal” niche and interacts with the Fe_2S_2 cluster ligands, and myxothiazol or MOA-stilbene, which binds in the “proximal” niche closer to the cyt b_L heme.

For either location, the nearest PRE constraint comes from interactions with the cyt b_L of the same monomer (i.e, the intradimer cyt b_L heme). The second interaction comes from interdimer cyt b_L in one case and from the intradimer cyt c_1 in the other. Although the data at present are unable to conclusively decide between them, the two locations have similar properties and allow us to identify the SQ as the elusive SQ_0 intermediate of the Q Cycle and making the ENDOR and ESEEM results highly relevant to the Q-cycle mechanism.

5.3.2 *Molecular Modeling of the SQ Distance Constraints*

Q-Site Finder (117) was used to fill the void volume of the Q_0 site of the yeast bc_1 atomic coordinates using the crystal structure 3CX5.PDB (118) with methyl ($-CH_3$) probe groups at a grid resolution of 0.9 Å. The resulting methyl-filled Q_0 void coordinates were appended to 3CX5 and written as a PDB file for visualization within VMD (119) EPR distance constraints overlapping with the Q_0 void volume were modeled in VMD using three-dimensional Boolean algebra and displayed volumetrically using the ‘QuickSurf’ representation within VMD.

5.4 Discussion:

5.4.1 *SQ binding sites within Q_o*

When constrained by PRE distances and steric clashes with the proteins, we found two possible SQ_o locations, both located within the Q_o site (figures 5.5 – 5.7). These locations are consistent with our previous observations (53) that 1) the formation of bacterial SQ_o is abolished by binding of stig and 2) SQ_o is isolated from solution .

Either location places SQ_o nearest the intramonomer cyt *b_L* heme, but they differ as to the next nearest heme. Using the distance to the intramonomer cyt *c₁* as a constraint yields a region of possible SQ_o locations, which we call site **I** that partly overlaps the chromone ring of bound stig (figures 5.5 and 5.6 in green). When the distance to intermonomer cyt *b_L* was instead used, site **II** (figures 5.5 and 5.7 in purple) was obtained, away from the region occupied by the chromone ring of stigmatellin and 13 Å from the Fe₂S₂ cluster of Q_o-docked ISP. Cyt *b_H* is reduced by previous turnovers, and thus non-paramagnetic. Sites **I** and **II** are separated by a closest approach of 8 Å, with edge-to-edge separations of 12 and 13.5 Å to heme *b_L* respectively. Using the Moser-Dutton approximation (37), these distances suggest a theoretical SQ_o/*b_L* electron transfer rates of 1 x 10⁶ s⁻¹ for site I and 4 x 10⁴ s⁻¹ for site II, which are in reasonable agreement with those expected or turnover in the uninhibited complex.

These two locations are not mutually exclusive and it is possible that SQ_o is distributed over the two niches. Moreover, either site is compatible with that obtained by EPR analysis of Q_o site occupancy in bacterial *bc₁* mutants where the SQ was proposed to move within Q_o during catalysis (120).

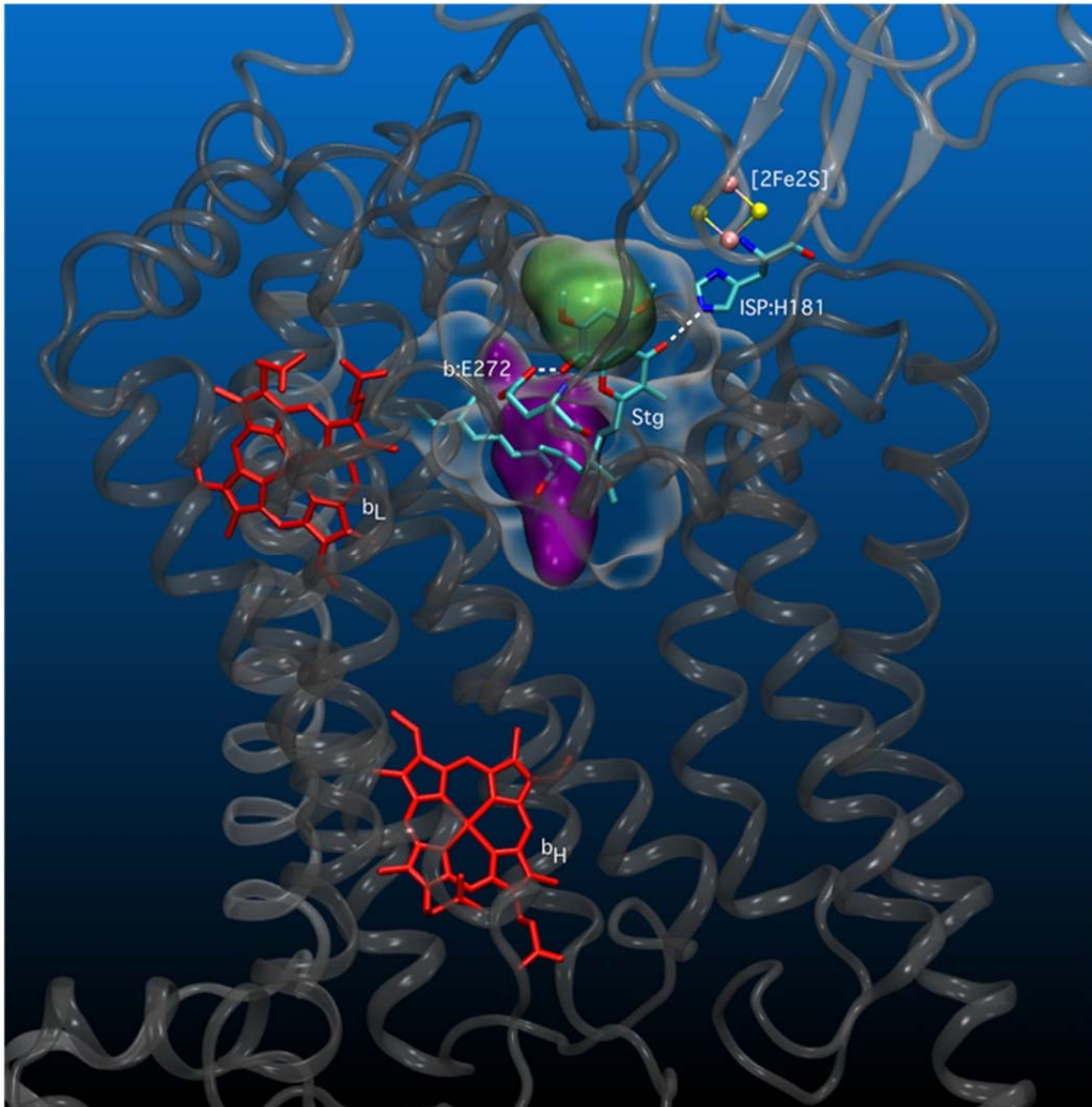


Figure 5.5 Volumetric representation of the SQ binding niches within yeast cytochrome *b*. The polypeptide backbones of cyt *b* and the ISP from one functional monomeric unit of the yeast bc_1 complex (3CX5.PDB, Solmaz and Hunte 2008) are represented in cartoon form in dark- and light grey respectively. The Q_o site volume defined by the b_L (intramonomer) / c_1 (intramonomer) distance constraints (site I) is represented in green, with the volume defined by the b_L (intramonomer)/ b_L (intermonomer) distance constraints (site II) represented in purple. The Q_o void volume is shown as a glass surface. Also shown are hemes b_L and b_H (in red) of cyt *b* and the Fe_2S_2 cluster of the ISP (yellow- and pink CPK). Cyt *b* residue E272 and Fe_2S_2 cluster-ligating ISP residue H181 are represented in stick form. Q_o -bound stigmatellin is labeled 'Stg'.

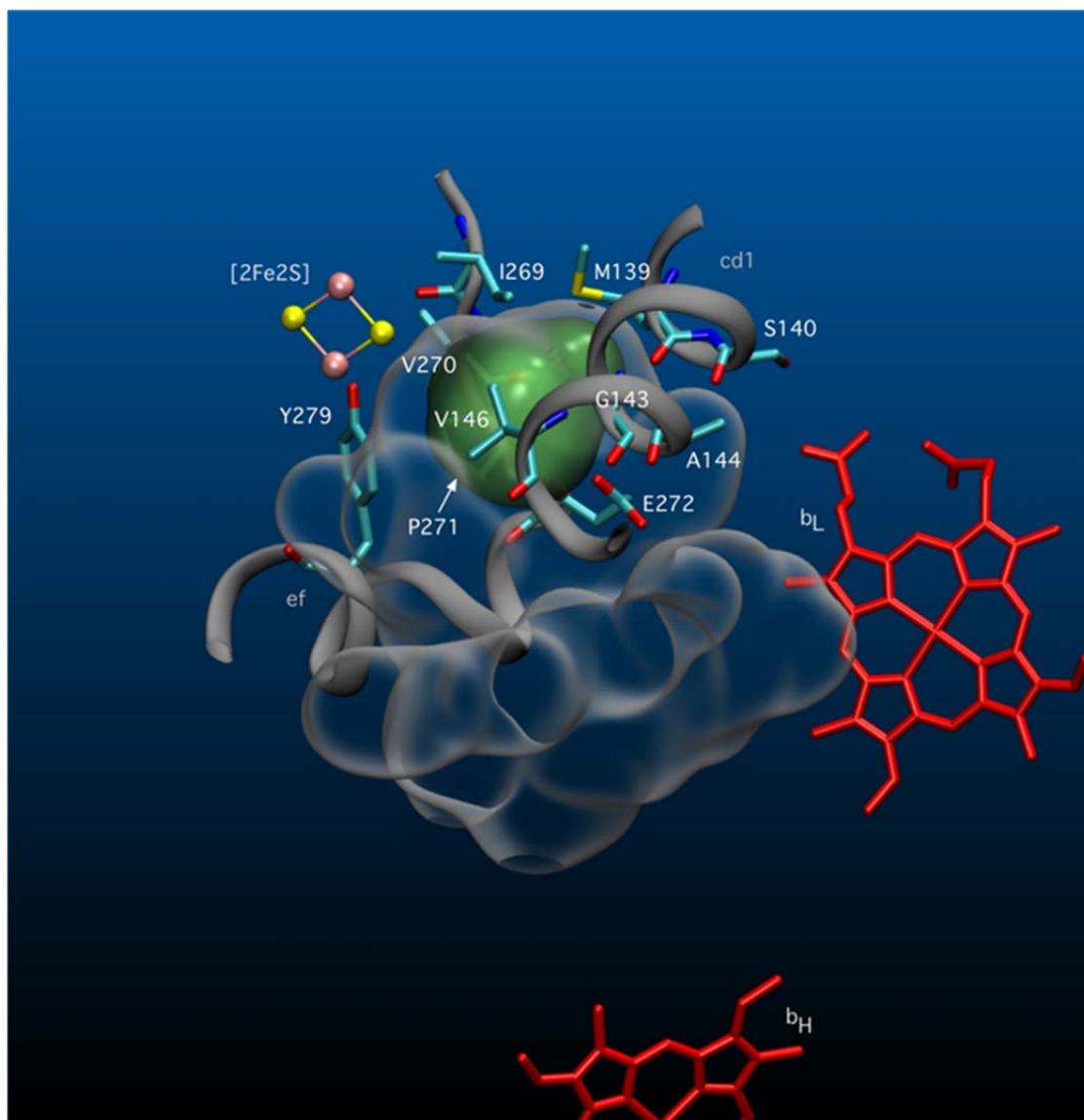


Figure 5.6 Detail of sidechain interactions between yeast *cyt b* (3CX5.PDB) and SQ site I. *Cyt b* residues in close contact ($< 4 \text{ \AA}$) with the Q_o volume defined by the b_L (intramonomer)/ c_1 (intramonomer) distance constraints (in green) are shown in stick form. The Q_o void volume is represented as a glass surface. Partial structures for *cyt b* helices $cd1$ and ef are shown in grey cartoon form, with the ISP Fe_2S_2 cluster in CPK format.

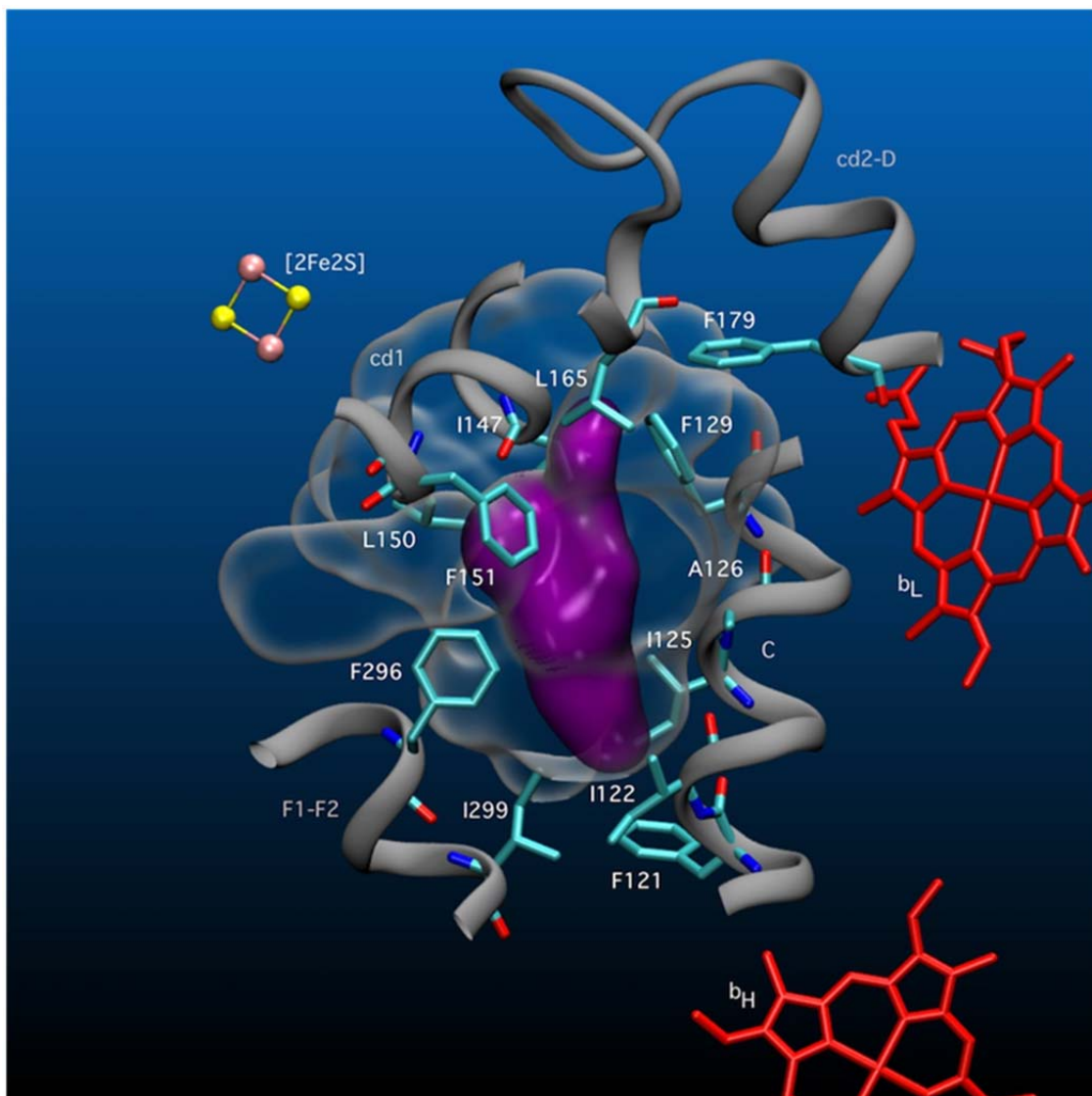


Figure 5.7 Detail of sidechain interactions between yeast cyt *b* (3CX5.PDB) and SQ site II. Cyt *b* residues in close contact ($< 4 \text{ \AA}$) with the Q_o volume defined by the b_L (intramonomer)/ b_L (intermonomer) distance constraints (in purple) are shown in stick form. The Q_o void volume is represented as a glass surface. Partial structures for cyt *b* helix C and the F1-F2 and cd2-D loops are shown in grey cartoon form, with the ISP Fe_2S_2 cluster in CPK format.

The cyt *bc₁* proteins at least two potential hydrogen-bonding groups in the site I, H181 on the

ISP and E272 on cyt *b*. H-bonding of SQ_o to both H181 and E272 would have to be thermodynamically or sterically prevented. Indeed, the ISP is known to pivot around its flexible tether and adopt multiple positions to allow electron transfer from the Q_o site to cyt *c*₁ (16). There is also evidence for intermediate ISP conformations that may alter (sterically and thermodynamically) interactions with Q_o site quinone species (121). The ISP may rapidly adopt a conformation that prevents H-bonding between H181 and SQ_o, allowing SQ to diffuse away. Likewise, the E272 glutamyl sidechain is found in different orientations in different crystal structures (122). In the stig-containing structure from yeast, the glutamyl carboxyl group makes a strong H-bond to the chromone hydroxyl (123), whereas in the famoxadone-containing bovine structure, it has flipped by 150° rotation about its χ^2 dihedral angle (124) and interacts with a potential proton channel within the cyt *b* protein. E272 is similarly rotated in the structure of the HHDBT-inhibited yeast *bc*₁, a compound proposed to mimic a hydroquinone anion. (125).

Aside from peptide backbone amides, site II has no obvious H-bond donors or acceptors. Site II is formed from predominantly hydrophobic, conserved residues from regions of cyt *b* encompassing trans-membrane helix C (residues 122-129), the cd1 helix (147-150) and the F1-F2 loop (296-299). The enthalpic cost of burying the anionic SQ in this non-polar niche (effectively a desolvation penalty) will likely be counterbalanced by entropic factors, i.e. driven by distribution among multiple possible binding conformations that can be accommodated within the niche II volume. This effect could stabilize the anionic SQ_o in a relatively aprotic environment.

5.4.2 **Reactions and Energetics:**

We propose that the unique properties and binding interactions seen for SQ_o are

important for the equally unique role of SQ_o in storing electrochemical energy and avoiding reactive side reactions (126). The data presented here allow us to explore the thermodynamic properties of SQ_o. As discussed previously (23, 53), the trapped SQ_o occurs at low occupancy, of 0.02-0.05 per complex, and assuming local equilibrium is reached among redox transitions and an operating redox potential of about 350 mV versus SHE for the high-potential electron carriers (Fe₂S₂ and cyt *c*), we calculate an effective midpoint potential for the SQ_o/QH₂ ($E_m(\text{SQ}_o/\text{QH}_2)$) between 400 and 450 mV. The extent of the PRE effect imply that about 30% of SQ_o are in Q_o sites containing oxidized cyt *b_L*(3⁺), suggesting an equilibrium constant for sharing electrons between SQ_o/Q and the cyt *b_L*(2⁺/3⁺) couples of about 3, and $E_m(\text{Q}/\text{SQ}_o)$ of about -120 mV. These estimates indicate a highly unstable SQ_o with $\Delta E_m(\text{SQ}_o/\text{QH}_2) - E_m(\text{Q}/\text{SQ}_o)$ of between 520-570 mV. (Highly stable SQ species will have a redox potential for reduction of Q to SQ that is more positive than that for reduction of SQ to QH₂, whereas highly unstable SQ species have the opposite so that reduction of Q to QH₂ is a highly coordinated, n=2, process).

Remarkably, this range for K_S is comparable to that expected for QH₂ in the membrane or in solution ($K_S \sim 10^{-10}$) (127), implying that the SQ_o is destabilized, or at least not stabilized, by interactions with the Q_o pocket. Most SQ species found in enzymes, e.g. at the Q_i site of *bc₁*, the Q_B sites of bacterial reaction centers and photosystem II, the QH₂ oxidation site of bacterial *bo₃*- and *aa₃* quinol oxidases (128, 129) etc., bind SQ considerably more tightly than Q or QH₂, raising K_S (by five- to ten orders of magnitude (130, 131)), allowing reduction of Q or oxidation of QH₂ to proceed by sequential, one-electron transitions. The high K_S for these species is critical for the so-called two electron gating which connects one-electron chemistry of cytochromes or Fe₂S₂ centers with the two-electron chemistry of Q/QH₂ (1). The redox properties of SQ_o more resemble those of the photosystem I phylloquinone, which also appears

destabilized with respect to solution (i.e. with a more reducing Q/SQ⁻ redox potential, to allow electron transfer to the low-potential Fx Fe₄S₄ cluster (132). Similar anionic semiquinone instability has been observed at the Q_B site of the bacterial photosynthetic reaction center following mutation of component arginine residues to non-polar isoleucines (133). The low K_S for SQ_o is consistent with a function in the Q-cycle since a stabilized SQ would not have sufficient reducing power to pass electrons against the electrochemical gradient to the low-potential cyt *b* (23).

Thermodynamically, an unstable SQ_o should also be weakly bound in the Q_o site since specific, tight binding through hydrogen bonds would stabilize the intermediate making it less able to reduce the low-potential chain. The structural data presented here suggests that, because it is charged, SQ_o is kinetically trapped, rather than thermodynamically stabilized, via an “electrostatic cage” of hydrophobic residues surrounding Q_o, providing a structural and mechanistic bases for maintaining SQ_o reactivity but preventing its rapid unbinding and subsequent loss of energy through escape and disproportionation (5).

5.5 Conclusions:

Our results lead us to propose that the *bc₁* complex traps SQ_o as an anionic, destabilized and non-hydrogen bonded intermediate in hydrophobic niches within Q_o. The anionic nature of the SQ intermediate – a result of sidechain-mediated ‘proton stripping’ at Q_o – is critical for favoring the Q-cycle and preventing short-circuiting and other deleterious side reactions (5).

The first electron transfer is accompanied by proton transfer to ISP H181, with the second proton abstracted by cyt *b* E272. The deprotonated SQ anion is then trapped (possibly coordinated) conformational changes in SQ_o intermediates and protein components, consistent

with several proposed models (121, 122, 134). The SQ_0 is trapped without thermodynamic stabilization because the surrounding low dielectric of the Q_0 site forms a hydrophobic “cage” (135).

The destabilized SQ_0 not only conserves sufficient redox energy to reduce *cyt b_L* , but should also diminish the rates of other potential Q-cycle bypass reactions or short circuits (5). The reduction of a SQ anion to Q^{2-} (without proton uptake) should be thermodynamically very unfavorable, preventing the oxidation of previously-reduced *cyt b_L* , a potential Q-cycle bypass reaction (5). Finally, as discussed in Cape et al. (5), the low occupancy of an unstable SQ_0 would also limit the diffusion-limited rate of O_2 reduction, minimizing superoxide production (23).

Overall, we make the (counterintuitive) observation that Nature guides the enigmatic Q-cycle reactions by forming an insulating “reaction chamber” that contains, but does not tightly interact with, the reactive intermediates of the Q-cycle. The chamber has the critical properties of preserving SQ_0 reactivity while removing protons that could lead to deleterious side reactions.

CHAPTER 6

SUMMARY

This chapter will summarize the major contributions of this work and further future studies.

6.1 Summary

As a first step, I was successful in trapping the SQ at the Q_o pocket in mitochondrial cyt *bc₁* complex. This is the very first time in the past 50 years that a SQ_o was ever trapped in mitochondrial cyt *bc₁*. The low concentration and the instability of SQ_o in mitochondrial cyt *bc₁* made it difficult to trap the radical, but if maintained proper conditions it can be trapped. The mitochondrial cyt *bc₁* as discussed earlier has great relevance to the human cyt *bc₁*, rather than the bacterial cyt *bc₁*. Hence the mitochondrial SQ_o will provide a better probe to study the Q-cycle and SO production in human cyt *bc₁* complex.

I was able to characterize the trapped SQ_o using several EPR techniques. The high-field EPR and the ENDOR results confirm that the SQ_o radical trapped in cyt *bc₁* is a radical anion. The 2-pulse and 3-pulse ESEEM confirms that the SQ_o does not form any hydrogen bonds to the nitrogens of amino acid side chains or the peptide backbone. The 4-pulse ESSEM of SQ_o lacks any indication of hydrogen bonding to the protein unlike in other proteins. These results indicate that the SQ_o formed is a radical anion and might not be stabilized or may even be destabilized in the protein, as a more stabilized SQ_o should form strong/weak hydrogen bonds with the protein.

In the destabilized SQ model the rate of formation of SQ_o would be the rate limiting step, which limits both the Q-cycle and the SO production and other unwanted bypass reactions.

As a further step, I was able to determine the physical location of the trapped SQ_o in the mitochondrial cyt *bc₁* complex using dipolar relaxation enhancement technique. The SQ_o appears to be trapped in a well-defined location that is 1.65-1.95 nm from the iron of one heme and 2.55-3.00 nm from that of another. When these distance constraints were applied to the PDB structure, I got two different locations, both in the Q_o pocket. The two locations have similar properties that are relevant to the ENDOR and ESEEM results. The data at present is not sufficient to conclusively decide between those two locations and further studies are necessary to differentiate between those two locations.

Overall, this dissertation makes the counterintuitive observation that Nature guides the enigmatic Q-cycle reactions by forming an insulating “reaction chamber” that contains, but does not interact tightly with, the reactive intermediates of the Q-cycle. The chamber has the critical properties of preserving SQ_o reactivity while removing protons that could lead to deleterious side reactions.

6.2 Future work

An attempt to differentiate between the two SQ_o binding locations and to identify the amino acid residues interacting with QH₂/SQ_o in the Q_o pocket has been started using mass spectrometric experiments. Here is a brief description of the project.

As a first step, and azido labeled UQ was prepared by the Snowden group at University of Alabama, that would mimic the natural substrate UQ. The 5-methyl group of the natural substrate UQ was replaced by the azido (N=N=N) group and is termed as azidoquinone (AZQ). The idea is that the AZQ would bind the protein at the same place as the natural substrate UQ,

and when the AZQ protein mixture is irradiated with long range UV light (350 nm), the AZQ would insert itself into an adjacent amino acid along with releasing N₂. The protein mixture is then subjected to trypsin digest and the fragments would be examined for the bound quinone molecule. The peptide sequence analysis using mass spectrometry would give us the information regarding the surroundings of the UQ when it bound. A careful analysis and comparison of mass spectrometry results with PDB structure would give us the location of UQ bound at the Q_o pocket.

The initial MALDI-TOF on the azido labeled UQ with cyt *bc₁*, showed that the quinone is bound to the cyt *b*, where it should. The further steps trypsin digest and peptide sequencing is in progress.

REFERENCES

1. Nitschke W, Kramer DM, Riedel A, & Liebl U (1995) From naphtho- to benzoquinones — (R)evolutionary reorganizations of electron transfer chains. *Photosynthesis: From Light to Biosphere*, ed Mathis P (Kluwer Academic Publishers, Dordrecht), Vol 1, pp 945–948.
2. Berry EA, Guergova-Kuras M, Huang LS, & Crofts AR (2000) Structure and function of cytochrome *bc* complexes. *Annu. Rev. Biochem.* 69:1005-1075.
3. Schutz M, *et al.* (2000) Early evolution of cytochrome *bc* complexes. *J Mol Biol* 300(4):663-675.
4. Crofts AR (2004) The cytochrome *bc₁* complex: Function in the context of structure. *Annu. Rev. Physiol.* 66:689-733.
5. Muller F, Crofts AR, & Kramer DM (2002) Multiple Q-cycle bypass reactions at the Q_o-site of the cytochrome *bc₁* complex. *Biochemistry* 41:7866-7874.
6. Pereira MD, Herdeiro RS, Fernandes PN, Eleutherio ECA, & Panek AD (2003) Targets of oxidative stress in yeast sod mutants. *Biochimica et Biophysica Acta (BBA) - General Subjects* 1620(1–3):245-251.
7. Jenner P (2003) Oxidative stress in Parkinson's disease. *Ann. Neurol.* 53(S3):S26-S38.
8. Poli G, Leonarduzzi G, Biasi F, & Chiarotto E (2004) Oxidative stress and cell signalling. *Curr. Med. Chem.* 11(9):1163-1182.
9. Emerit J, Edeas M, & Bricaire F (2004) Neurodegenerative diseases and oxidative stress. *Biomedicine & Pharmacotherapy* 58(1):39-46.
10. Rosenberg P (2004) Mitochondrial dysfunction and heart disease. *Mitochondrion* 4(5–6):621-628.
11. Rolo AP & Palmeira CM (2006) Diabetes and mitochondrial function: Role of hyperglycemia and oxidative stress. *Toxicol. Appl. Pharmacol.* 212(2):167-178.
12. Gao X, *et al.* (2003) Structural Basis for the Quinone Reduction in the *bc₁* Complex: A Comparative Analysis of Crystal Structures of Mitochondrial Cytochrome *bc₁* with Bound Substrate and Inhibitors at the Q_i Site†,‡. *Biochemistry (Mosc)*. 42(30):9067-9080.

13. Hunte C, Solmaz S, & Lange C (2002) Electron transfer between yeast cytochrome bc1 complex and cytochrome c: a structural analysis. *Biochimica et Biophysica Acta (BBA) - Bioenergetics* 1555(1–3):21-28.
14. Gao X, *et al.* (2002) The Crystal Structure of Mitochondrial Cytochrome bc1 in Complex with Famoxadone: The Role of Aromatic–Aromatic Interaction in Inhibition†,‡. *Biochemistry (Mosc)*. 41(39):11692-11702.
15. Hunte C, Koepke J, Lange C, Roßmanith T, & Michel H (2000) Structure at 2.3 Å resolution of the cytochrome bc1 complex from the yeast *Saccharomyces cerevisiae* co-crystallized with an antibody Fv fragment. *Structure* 8(6):669-684.
16. Kim H, *et al.* (1998) Inhibitor binding changes domain mobility in the iron-sulfur protein of the mitochondrial bc1 complex from bovine heart. *Proc. Natl. Acad. Sci. U. S. A.* 95(14):8026-8033.
17. Iwata S, *et al.* (1998) Complete structure of the 11-subunit bovine mitochondrial cytochrome bc(1) complex. *Science* 281(5373):64-71.
18. Xia D, *et al.* (1997) Crystal structure of the cytochrome bc(1) complex from bovine heart mitochondria. *Science* 277(5322):60-66.
19. Ding H, *et al.* (1995) Ubiquinone Pair in the Qo Site Central to the Primary Energy Conversion Reactions of Cytochrome bc1 Complex. *Biochemistry (Mosc)*. 34(49):15979-15996.
20. Trumpower BL (1990) The protonmotive Q cycle. Energy transduction by coupling of proton translocation to electron transfer by the cytochrome bc1 complex. *J. Biol. Chem.* 265(20):11409-11412.
21. Crofts AR & Wang ZG (1989) How Rapid Are TheE Internal Reactions of The Ubiquinol-Cytochrome-C2 Oxidoreductase. *Photosynthesis Research* 22(1):69-87.
22. Peter M (1975) The protonmotive Q cycle: A general formulation. *FEBS Lett.* 59(2):137-139.
23. Cape JL, Bowman MK, & Kramer DM (2006) Understanding the cytochrome bc complexes by what they don't do. The Q-cycle at 30. *Trends in Plant Science* 11(1):46-55.
24. Ding H, Robertson DE, Daldal F, & Dutton PL (1992) Cytochrome bc1 complex [2Fe-2S] cluster and its interaction with ubiquinone and ubihydroquinone at the Qo site: a double-occupancy Qo site model. *Biochemistry (Mosc)*. 31(12):3144-3158.

25. Ulrich B (1996) Energy conservation by bifurcated electron-transfer in the cytochrome-bc₁ complex. *Biochimica et Biophysica Acta (BBA) - Bioenergetics* 1275(1–2):41-46.
26. Brandt U & Trumpower B (1994) The Protonmotive Q Cycle in Mitochondria and Bacteria. *Crit. Rev. Biochem. Mol. Biol.* 29(3):165-197.
27. Berry EA & Huang LS (2003) Observations concerning the quinol oxidation site of the cytochrome bc(1) complex. *FEBS Lett.* 555(1):13-20.
28. Darrouzet E, Moser CC, Dutton PL, & Daldal F (2001) Large scale domain movement in cytochrome bc₁: a new device for electron transfer in proteins. *Trends Biochem. Sci.* 26(7):445-451.
29. Stroebel D, Choquet Y, Popot J-L, & Picot D (2003) An atypical haem in the cytochrome b₆f complex. *Nature* 426(6965):413-418.
30. Kurisu GHJLCWA (2003) Structure of the Cytochrome b₆f Complex of OxygenicPhotosynthesis: Tuning the Cavity. *Science* 302(5647):1009-1014.
31. Roberts AG, Bowman MK, & Kramer DM (2004) The Inhibitor DBMIB Provides Insight into the Functional Architecture of the Q_o Site in the Cytochrome b₆f Complex†. *Biochemistry (Mosc).* 43(24):7707-7716.
32. Cooley JW, Roberts AG, Bowman MK, Kramer DM, & Daldal F (2004) The Raised Midpoint Potential of the [2Fe2S] Cluster of Cytochrome bc₁ Is Mediated by Both the Q_o Site Occupants and the Head Domain Position of the Fe–S Protein Subunit†. *Biochemistry (Mosc).* 43(8):2217-2227.
33. Roberts AG, Bowman MK, & Kramer DM (2002) Certain Metal Ions Are Inhibitors of Cytochrome b₆f Complex ‘Rieske’ Iron–Sulfur Protein Domain Movements†. *Biochemistry (Mosc).* 41(12):4070-4079.
34. Schoepp B, Brugna M, Riedel A, Nitschke W, & Kramer DM (1999) The Q_o-site inhibitor DBMIB favours the proximal position of the chloroplast Rieske protein and induces a pK-shift of the redox-linked proton. *FEBS Lett.* 450(3):245-250.
35. Brugna M, *et al.* (1999) Redox Components of Cytochrome bc-type Enzymes in Acidophilic Prokaryotes. *J. Biol. Chem.* 274(24):16766-16772.
36. Osyczka A, Moser CC, & Dutton PL (2005) Fixing the Q cycle. *Trends Biochem. Sci.* 30(4):176-182.
37. Osyczka A, Moser CC, Daldal F, & Dutton PL (2004) Reversible redox energy coupling in electron transfer chains. *Nature* 427(6975):607-612.

38. Muller FL, Roberts AG, Bowman MK, & Kramer DM (2003) Architecture of the Qo Site of the Cytochrome bc₁ Complex Probed by Superoxide Production†. *Biochemistry (Mosc)*. 42(21):6493-6499.
39. Muller F, Crofts AR, & Kramer DM (2002) Multiple Q-Cycle Bypass Reactions at the Qo Site of the Cytochrome bc₁ Complex†. *Biochemistry (Mosc)*. 41(25):7866-7874.
40. Kramer DM, Roberts AG, Muller F, Cape J, & Bowman MK (2004) Q-Cycle Bypass Reactions at the Qo Site of the Cytochrome bc₁ (and Related) Complexes. *Methods Enzymol.*, eds Helmut S & Lester P (Academic Press), Vol Volume 382, pp 21-45.
41. Shinkarev VP, Crofts AR, & Wraight CA (2001) The electric field generated by photosynthetic reaction center induces rapid reversed electron transfer in the bc₁(1) complex. *Biochemistry (Mosc)*. 40(42):12584-12590.
42. Zhang L, Yu LD, & Yu CA (1998) Generation of superoxide anion by succinate-cytochrome c reductase from bovine heart mitochondria. *J. Biol. Chem.* 273(51):33972-33976.
43. Cape JL, *et al.* (2005) The respiratory substrate rholoquinol induces Q-cycle bypass reactions in the yeast cytochrome bc₁(1) complex - Mechanistic and physiological implications. *J. Biol. Chem.* 280(41):34654-34660.
44. Fisher N, Bourges I, Hill P, Brasseur G, & Meunier B (2004) Disruption of the interaction between the Rieske iron-sulfur protein and cytochrome b in the yeast bc₁(1) complex owing to a human disease-associated mutation within cytochrome b. *Eur. J. Biochem.* 271(7):1292-1298.
45. Fisher N & Meunier B (2001) Effects of mutations in mitochondrial cytochrome b in yeast and man. *Eur. J. Biochem.* 268(5):1155-1162.
46. Martin GM & Loeb LA (2004) Ageing - Mice and mitochondria. *Nature* 429(6990):357.
47. Fisher N, *et al.* (2004) Human Disease-related Mutations in Cytochrome b Studied in Yeast. *J. Biol. Chem.* 279(13):12951-12958.
48. Forquer I, Covian R, Bowman MK, Trumpower BL, & Kramer DM (2006) Similar transition states mediate the Q-cycle and superoxide production by the cytochrome bc₁(1) complex. *J. Biol. Chem.* 281(50):38459-38465.
49. Crofts AR, Lhee S, Crofts SB, Cheng J, & Rose S (2006) Proton pumping in the bc₁(1) complex: A new gating mechanism that prevents short circuits. *Biochimica Et Biophysica Acta-Bioenergetics* 1757(8):1019-1034.

50. Cape JL, Bowman MK, & Kramer DM (2007) A semiquinone intermediate generated at the Q(o) site of the cytochrome bc(1)_l complex: Importance for the Q-cycle and superoxide production. *Proc. Natl. Acad. Sci. U. S. A.* 104(19):7887-7892.
51. Cape JL, Bowman MK, & Kramer DM (2005) Reaction intermediates of quinol oxidation in a photoactivatable system that mimics electron transfer in the cytochrome bc(1)_l complex. *J. Am. Chem. Soc.* 127(12):4208-4215.
52. Junemann S, Heathcote P, & Rich PR (1998) On the mechanism of quinol oxidation in the bc₁ complex. *J Biol Chem* 273(34):21603-21607.
53. Cape JL, Bowman MK, & Kramer DM (2007) A semiquinone intermediate generated at the Q_o site of the cytochrome bc₁ complex: importance for the Q-cycle and superoxide production. *Proceedings of the National Academy of Sciences of the United States of America* 104(19):7887-7892.
54. Zhang HB, Osyczka A, Dutton PL, & Moser CC (2007) Exposing the complex III Q_o semiquinone radical. *Biochimica Et Biophysica Acta-Bioenergetics* 1767(7):883-887.
55. Cape JL, Aidasani D, Kramer DM, & Bowman MK (2009) Substrate Redox Potential Controls Superoxide Production Kinetics in the Cytochrome bc Complex. *Biochemistry (Mosc)*. 48(45):10716-10723.
56. Berry EA & Huang LS (2011) Conformationally linked interaction in the cytochrome bc(1)_l complex between inhibitors of the Q(o) site and the Rieske iron-sulfur protein. *Biochimica Et Biophysica Acta-Bioenergetics* 1807(10):1349-1363.
57. Kulikov AV & Likhtenstein GI (1977) The use of spin relaxation phenomena in the investigation of the structure of model and biological systems by the method of spin labels. *Advances in Molecular Relaxation and Interaction Processes* 10(1):47-79.
58. Likhtenshtein GI (2000) Depth of Immersion of Paramagnetic Centers in Biological Systems. *Distance Measurement in Biological Systems by EPR, Biological Magnetic Resonance*, eds Berliner LJ, Eaton GR, & Eaton SS (Kluwer Academic, New York), pp 309-345.
59. Sarewicz M, Dutka Mg, Froncisz W, & Osyczka A (2009) Magnetic Interactions Sense Changes in Distance between Heme b_L and the Iron-Sulfur Cluster in Cytochrome bc₁. *Biochemistry* 48(24):5708-5720.
60. Rao B. K S, Tyryshkin AM, Roberts AG, Bowman MK, & Kramer DM (2000) Inhibitory Copper Binding Site on the Spinach Cytochrome b₆f Complex: Implications for Q_o Site Catalysis. *Biochemistry* 39:3285-3296.

61. Lyubenova S, Siddiqui MK, de Vries M, Ludwig B, & Prisner TF (2007) Protein-protein interactions studied by EPR relaxation measurements: Cytochrome c and cytochrome c oxidase. *Journal of Physical Chemistry B* 111(14):3839-3846.
62. Ulyanov D, Bowler BE, Eaton GR, & Eaton SS (2008) Electron-Electron Distances in Spin-Labeled Low-Spin Metmyoglobin Variants by Relaxation Enhancement. *Biophys. J.* 95(11):5306-5316.
63. Ljungdahl O, Pennoyer JD, Robertson DE, & Trumpower BL (1987) Purification of Highly-Active Cytochrome-BC1 Complexes From Phylogenetically Diverse Species by a Single Chromatographic Procedure. *Biochim. Biophys. Acta* 891(3):227-241.
64. Appleyard RJ & Evans JNS (1993) Solid-State NMR of Glycine in Frozen Solution. *Journal of Magnetic Resonance Series B* 102(3):245-252.
65. Appleyard RJ, Shuttleworth WA, & Evans JNS (1994) Time-Resolved Solid-State NMR-Spectroscopy of 5-Enolpyruvylshikimate-3-Phosphate Synthase *Biochemistry (Mosc)*. 33(22):6812-6821.
66. Abragam A (1961) *Principles of Nuclear Magnetism* (Clarendon Press Oxford, New York).
67. Carrington A & McLachlan AD (1967) *Introduction to Magnetic Resonance* (John Weatherhill Inc.).
68. Gringberg OY & Berliner LJ (2004) *Very High Frequency (VHF) ESR/EPR* (Kluwer Academic/Plenum Publishers).
69. Ernst RR, Bodenhausen G, & Wokaun A (1987) *Principles of Nuclear Magnetic Resonance in One and Two Dimensions* (Clarendon Press Oxford, New York).
70. Berliner LJ, Eaton SS, & Eaton GR (2000) *Distance Measurements in Biological Systems by EPR* (Kluwer Academic/Plenum Publishers, New York).
71. Poole CPJ & Farach HA (1971) *Relaxation in Magnetic Resonance: Dielectric and Mossbauer Applications* (Academic Press, New York/London).
72. Schweiger A & Jeschke G (2001) *Principles of pulse electron paramagnetic resonance* (Oxford University Press Inc., New York).
73. Murphy J (1966) Spin-lattice relaxation due to local vibrations with temperature-independent amplitudes. *Physical Review* 145(1):241.
74. Orbach R & Stapleton HJ (1972) *Electron Spin-lattice relaxation: Electron Paramagnetic Resonance* (Plenum, New York).

75. Weil JA, Bolton JR, & Wertz JE (1994) *Electron Paramagnetic Resonance: Elementary Theory and Practical Applications* (John Wiley & Sons, Inc., New York).
76. Brustolon M & Giamello E (2009) *Electron paramagnetic Resonance: A Practitioner's Toolkit*.
77. Vries Pd (2007) Distance Measurements between Paramagnetic Centers by High-Field EPR Relaxation Experiments. PhD Dissertation (J. W. Goeth University, Frankfurt am Main, Germany).
78. Milov AD, Ponomarev AB, & Tsvetkov YD (1984) Electron Electron Double-Resonance in Electron-Spin Echo - Model Biradical Systems and The Sensitized Photolysis of Decalin. *Chemical Physics Letters* 110(1):67-72.
79. Larsen RG & Singel DJ (1993) Double Electron-Electron Resonance Spin Echo Modulation Spectroscopic Measurement of Electron-Spin Pair Separations in Orientationally Disordered Solids. *J. Chem. Phys.* 98(7):5134-5146.
80. Martin RE, *et al.* (1998) Determination of end-to-end distances in a series of TEMPO diradicals of up to 2.8 nm length with a new four-pulse double electron electron resonance experiment. *Angewandte Chemie-International Edition* 37(20):2834-2837.
81. Kulik LV, Dzuba SA, Grigoryev IA, & Tsvetkov YD (2001) Electron dipole-dipole interaction in ESEEM of nitroxide biradicals. *Chemical Physics Letters* 343(3-4):315-324.
82. Kulik LV, Paschenko SV, & Dzuba SA (2002) 130 GHz ESEEM induced by electron-electron interaction in biradical. *J. Magn. Reson.* 159(2):237-241.
83. Kulik LV & Dzyuba SA (2004) Electron spin echo study of molecular structure and dynamics: New approaches based on spontaneous fluctuations of magnetic interactions. *Journal of Structural Chemistry* 45(2):298-314.
84. Deligiannakis Y, Louloudi M, & Hadjiliadis N (2000) Electron spin echo envelope modulation (ESEEM) spectroscopy as a tool to investigate the coordination environment of metal centers. *Coordination Chemistry Reviews* 204:1-112.
85. Rowan LG, Hahn EL, & Mims WB (1965) Electron-Spin-Echo Envelope Modulation. *Physical Review* 137(1A):A61.
86. Mims WB (1972) Envelope Modulation in Spin-Echo Experiments. *Physical Review B-Solid State* 5(7):2409.

87. Gemperle C, Aebli G, Schweiger A, & Ernst RR (1990) Phase Cycling In Pulse EPR. *J. Magn. Reson.* 88(2):241-256.
88. Schweiger A (1991) Pulsed Electron Spin Resonance Spectroscopy- Basic Principles, Techniques and Examples of Applications. *Angewandte Chemie-International Edition in English* 30(3):265-292.
89. Lee HI & McCracken J (1994) 4-Pulse Electron-Spin Echo Envelope Modulation Studies of Axial Water Ligation to Diaquatetracyanonickelate (III) *J. Phys. Chem.* 98(49):12861-12870.
90. Matar K & Goldfarb D (1994) The Combination Harmonics in 4-Pulse Electron Spin Echo Envelope Modulation of a S=1/2, I=5/2 Spin System Under Orientational Disorder *Journal of Magnetic Resonance Series A* 111(1):50-61.
91. Tyryshkin AM, Dikanov SA, Evelo RG, & Hoff AJ (1992) Properties of The Combination Harmonic in Spectra of Primary Electron Spin Echo Envelope Modulation of Orientationally Selected Disordered Systems Application to Aqua-Oxovanadium Complexes *J. Chem. Phys.* 97(1):42-49.
92. Tyryshkin AM, Dikanov SA, & Goldfarb D (1993) Sum Combination Harmonics in 4-Pulse ESEEM Spectra- Study of The Ligand Geometry in Aqua Vanadyl Complexes in Polycrystalline and Glass Matrices. *Journal of Magnetic Resonance Series A* 105(3):271-283.
93. Van Doorslaer S & Schweiger A (1997) A two-dimensional sum combination frequency pulse EPR experiment. *Chemical Physics Letters* 281(4-6):297-305.
94. Kevan L & Kispert LD (1976) *Electron Nuclear Double Resonance Spectroscopy* (Wiley, New York).
95. Kevan L & Bowman MK (1990) *Modern Pulsed and Continuous Wave Electron Spin Resonance* (Wiley, New York).
96. Mims WB & Peisach J (1989) *Advanced EPR: Applications Biology and Biochemistry* (Elsevier, Amsterdam).
97. Doan PE & Hoffman BM (1997) Making hyperfine selection in Mims ENDOR independent of deadtime. *Chem. Phys. Lett.* 269(3,4):208-214.
98. Kolling DRJ, *et al.* (2003) Exploration of ligands to the Q(i) site semiquinone in the bc(1) complex using high-resolution EPR. *J. Biol. Chem.* 278(41):39747-39754.
99. Stoll S & Schweiger A (2006) EasySpin, a comprehensive software package for spectral simulation and analysis in EPR. *J. Magn. Reson.* 178(1):42-55.

100. MacMillan F, Lange C, Bawn M, & Hunte C (2010) Resolving the EPR Spectra in the Cytochrome bcl Complex from *Saccharomyces cerevisiae* *Applied Magnetic Resonance* 37(1):305-316.
101. Grimaldi S, *et al.* (2003) Asymmetric binding of the high-affinity Q(H)(center dot-) ubisemiquinone in quinol oxidase (bo(3)) from *Escherichia coli* studied by multifrequency electron paramagnetic resonance spectroscopy. *Biochemistry (Mosc)*. 42(19):5632-5639.
102. Vandenbrink JS, *et al.* (1994) Asymmetric Binding of The Primary Acceptor Quinone in Reaction Centers of The Photosynthetic Bacterium *Rhodobacter Sphaeroides* R26, Probed With Q-Band (35 GHz) EPR Spectroscopy *FEBS Lett.* 353(3):273-276.
103. Burghaus O, *et al.* (1993) 3-mm High-field EPR on semiquinone radical anions Q.- related to photosynthesis and on the primary donor P.+ and acceptor QA.- in reaction centers of *Rhodobacter sphaeroides* R-26. *The Journal of Physical Chemistry* 97(29):7639-7647.
104. Nimz O, Lenzian F, Boullais C, & Lubitz W (1998) Influence of hydrogen bonds on the electronic g-tensor and C-13-hyperfine tensors of C-13-labeled ubiquinones - EPR and ENDOR study. *Applied Magnetic Resonance* 14(2-3):255-274.
105. Grimaldi S, *et al.* (2001) QH•- Ubisemiquinone Radical in the bo3-Type Ubiquinol Oxidase Studied by Pulsed Electron Paramagnetic Resonance and Hyperfine Sublevel Correlation Spectroscopy†. *Biochemistry (Mosc)*. 40(4):1037-1043.
106. Lubitz W & Feher G (1999) The primary and secondary accepters in bacterial photosynthesis III. Characterization of the quinone radicals QA(-)center dot and QB(-center dot) by EPR and ENDOR. *Applied Magnetic Resonance* 17(1):1-48.
107. MacMillan F, Lenzian F, & Lubitz W (1995) EPR and ENDOR characterization of semiquinone anion radicals related to photosynthesis. *Magnetic Resonance in Chemistry* 33:S81-S93.
108. Esser L, *et al.* (2004) Crystallographic studies of quinol oxidation site inhibitors: a modified classification of inhibitors for the cytochrome bc(1) complex. *Journal of Molecular Biology* 341(1):281-302.
109. Martin E, *et al.* (2011) Hydrogen Bonding and Spin Density Distribution in the Q(B) Semiquinone of Bacterial Reaction Centers and Comparison with the Q(A) Site. *Journal of the American Chemical Society* 133(14):5525-5537.

110. Martin E, *et al.* (2011) Hydrogen Bonding and Spin Density Distribution in the QB Semiquinone of Bacterial Reaction Centers and Comparison with the QA Site. *J. Am. Chem. Soc.* 133(14):5525-5537.
111. Martin E, Samoilova RI, Narasimhulu KV, Wraight CA, & Dikanov SA (2010) Hydrogen Bonds between Nitrogen Donors and the Semiquinone in the Q(B) Site of Bacterial Reaction Centers. *Journal of the American Chemical Society* 132(33):11671-11677.
112. Yap LL, Samoilova RI, Gennis RB, & Dikanov SA (2007) Characterization of mutants that change the hydrogen bonding of the semiquinone radical at the QH site of the cytochrome bo3 from Escherichia coli. *J Biol Chem* 282(12):8777-8785.
113. MacMillan F, *et al.* (2011) Elucidating mechanisms in haem copper oxidases: The high-affinity Q(H) binding site in quinol oxidase as studied by DONUT-HYSCORE spectroscopy and density functional theory. *Faraday Discuss.* 148:315-344.
114. Dikanov SA, *et al.* (2007) Hydrogen bonds between nitrogen donors and the semiquinone in the Qi-site of the bc1 complex. *J Biol Chem* 282(35):25831-25841.
115. Allen JP, Colvin JT, Stinson DG, Flynn CP, & Stapleton HJ (1982) Protein Conformation From Electron-Spin Relaxation Data. *Biophys. J.* 38(3):299-310.
116. Salikhov KM, Dzuba SA, & Raitsimring AM (1981) The theory of electron spin-echo signal decay resulting from dipole-dipole interactions between paramagnetic centers in solids. *Journal of Magnetic Resonance (1969)* 42(2):255-276.
117. Laurie ATR & Jackson RM (2005) Q-SiteFinder: an energy-based method for the prediction of protein-ligand binding sites. *Bioinformatics* 21(9):1908-1916.
118. Solmaz SRN & Hunte C (2008) Structure of complex III with bound cytochrome c in reduced state and definition of a minimal core interface for electron transfer. *The Journal of biological chemistry* 283(25):17542-17549.
119. Humphrey W, Dalke A, & Schulten K (1996) VMD: visual molecular dynamics. *Journal of molecular graphics* 14(1):33-38- 27-38.
120. Crofts AR, *et al.* (2000) Mechanism of ubiquinol oxidation by the bc(1) complex: different domains of the quinol binding pocket and their role in the mechanism and binding of inhibitors. *Biochemistry* 38(48):15807-15826.
121. Cooley JW, Roberts AG, Bowman MK, Kramer DM, & Daldal F (2004) The raised midpoint potential of the [2Fe2S] cluster of cytochrome bc1 is mediated by both the Qo site occupants and the head domain position of the Fe-S protein subunit. *Biochemistry* 43(8):2217-2227.

122. Berry EA & Huang LS (2011) Conformationally linked interaction in the cytochrome bc(1) complex between inhibitors of the Q(o) site and the Rieske iron-sulfur protein. *Biochimica et biophysica acta* 1807(10):1349-1363.
123. Hunte C, Koepke J, Lange C, Rossmann T, & Michel H (2000) Structure at 2.3 Å resolution of the cytochrome bc(1) complex from the yeast *Saccharomyces cerevisiae* co-crystallized with an antibody Fv fragment. *Structure with Folding and Design* 8(6):669-684.
124. Gao X, *et al.* (2002) The Crystal Structure of Mitochondrial Cytochrome bc1 in Complex with Famoxadone: The Role of Aromatic-Aromatic Interaction in Inhibition. *Biochemistry* 41(39):11692-11702.
125. Palsdottir H, Lojero CG, Trumpower BL, & Hunte C (2003) Structure of the Yeast Cytochrome bc1 Complex with a Hydroxyquinone Anion Qo Site Inhibitor Bound. *Journal of Biological Chemistry* 278(33):31303-31311.
126. Cape JL, Bowman MK, & Kramer DM (2006) Understanding the cytochrome *bc* complexes by what they don't do. The Q-cycle at 30. *Trends in Plant Science* 11:46-55.
127. Mitchell P (1976) Possible molecular mechanisms of the protonmotive function of cytochrome systems. *Journal of theoretical biology* 62(2):327-367.
128. Ingledew WJ, Ohnishi T, & Salerno JC (1995) Studies on a stabilisation of ubisemiquinone by *Escherichia coli* quinol oxidase, cytochrome bo. *European journal of biochemistry / FEBS* 227(3):903-908.
129. Yi SM, Narasimhulu KV, Samoilova RI, Gennis RB, & Dikanov SA (2010) Characterization of the Semiquinone Radical Stabilized by the Cytochrome aa3-600 Menaquinol Oxidase of *Bacillus subtilis*. *Journal of Biological Chemistry* 285(24):18241-18251.
130. Hägerhäll C, *et al.* (1999) An *Escherichia coli* mutant quinol:fumarate reductase contains an EPR-detectable semiquinone stabilized at the proximal quinone-binding site. *The Journal of biological chemistry* 274(37):26157-26164.
131. Gunner MR, Madeo J, & Zhu Z (2008) Modification of quinone electrochemistry by the proteins in the biological electron transfer chains: examples from photosynthetic reaction centers. *Journal of bioenergetics and biomembranes* 40(5):509-519.
132. Shinkarev VP, Vassiliev IR, & Golbeck JH (2000) A kinetic assessment of the sequence of electron transfer from F(X) to F(A) and further to F(B) in photosystem I: the value of the equilibrium constant between F(X) and F(A). *Biophys J* 78(1):363-372.

133. Cherepanov DA, *et al.* (2000) Reduction and protonation of the secondary quinone acceptor of *Rhodobacter sphaeroides* photosynthetic reaction center: kinetic model based on a comparison of wild-type chromatophores with mutants carrying Arg-->Ile substitution at sites 207 and 217 in the L-subunit. *Biochimica et biophysica acta* 1459(1):10-34.
134. Crofts AR, *et al.* (1999) Mechanism of ubiquinol oxidation by the bc(1) complex: role of the iron sulfur protein and its mobility. *Biochemistry (Mosc)*. 38(48):15791-15806.
135. Shinkarev VP (2006) Ubiquinone (coenzyme Q10) binding sites: low dielectric constant of the gate prevents the escape of the semiquinone. *FEBS letters* 580(11):2534-2539.

APPENDIX

Appendix A.1

```
function setup_T2_fitting
% This routine pulls in experimental data
%If VTU was not used it is necessary to manually put the
% temperatures in fit parameters

[reference,exppar]=loadreference;
[reference2,exppar2]=loadreference;
% Pull experimental parameters from reference
assignin('base','exppar',exppar);
spectra=loadspectra;

assignin('base','reference',reference);
assignin('base','reference2',reference2);
assignin('base','spectra',spectra);

% Loads in the reference
function [reference,exppar]=loadreference
[filename,pathname] = uigetfile('*.DTA','Load Reference Spectrum');%
% Some nifty tricks for multiple files at a time
if ischar(filename)==1 || iscell(filename)==1
    if
        ischar(filename)==1;file=filename;
    else
        file = cell2mat(filename(n));
    end
    [~, name] = fileparts(file);
    Importd = brukerimport(fullfile(pathname,file));
    File = strep(file, 'DTA', 'DSC');
    Title = fullfile(pathname,file);
    if
        isvarname(name)==0
            name = genvarname(name); %#ok<NASGU>
    end

% Assignin('base',name,importd); %saves data to workspace
importd{1} = importd{1};
importd{2} = importd{2};
reference = importd;
```

```

% Build exppar from .dsc file
Desc = textread(title,'%s');
Desc = strtrim(desc);
Indx = findstring(desc,'MWFQ');
Freq = str2double(desc{indx+1})/10^9; % Frequency of experiment
Indx = findstring(desc,'CenterField');
Field = str2double(desc{indx+1}); % Field of experiment
Indx = findstring(desc,'AVGS');
N = str2double(desc{indx+1});
reference{5} = N; % Number of averages
indx = findstring(desc,'shot');
H = str2double(desc{indx-5});
reference{6} = H; % Number of shots per average
exppar = [length(importd{1}) % Number of time points
importd{1}(2)-importd{1}(1) % Time increment
importd{1}(1) % Starting time tau
field % Field of experiment
freq]; % Frequency of spectrometer

```

```

end
return

```

```

% Load in remaining spectra
function spectra=loadspectra
[filename,pathname]=uigetfile('*.DTA','Load Spectra','MultiSelect','on');
% Some nifty tricks for multiple files at a time
if ischar(filename)==1 || iscell(filename)==1
    if
        ischar(filename)==1;num=1;
    else
        num=numel(filename);
    end
for
    n=1:num
    if
        ischar(filename)==1;file=filename;
    else
        file=cell2mat(filename(n));
    end
    [~,name] = fileparts(file);
    importd=brukerimport(fullfile(pathname,file));
    importd{1}=importd{1};
    importd{2}=importd{2};
end

```

```

if
length(importd{1})~=length(importd{2})
continue
end

% Importd=esephase(importd);

File = strep(file, 'DTA', 'DSC');
Title = fullfile(pathname,file);
Desc = textread(title,'%s');
Indx = findstring(desc,'STMP');
spectra{n,1} = file; %#ok<*AGROW>
if
    indx~ = 0
    temp = str2double(desc{indx+1});
    spectra{n,2} = temp;
end
spectra{n,3} = importd{1};
spectra{n,4} = importd{2};
indx = findstring(desc,'AVGS');
N = str2double(desc{indx+1});
spectra{n,5} = N;
indx = findstring(desc,'shot');
H = str2double(desc{indx-5});
spectra{n,6} = H;
if
    isvarname(name)==0
    name = genvarname(name); %#ok<NASGU>
end
% Assignin('base',name,importd); %saves data to workspace
end
return

function data=brukerimport(filename)
% Output is a cell with components of the dimensions of the data.
fid = fopen(filename,'r','s');
rawbin = fread(fid,inf,'real*8=>double');
filename = strep(filename, 'DTA', 'DSC');
% Reads in the description file for manipulation
desc=textread(filename,'%s');
desc=strtrim(desc);
fclose('all');
% Converts the dataset to complex data if necessary.
indx=findstring(desc,'IKKF');

```

```

if
    strmatch(desc{indx+1},'CPLX')==1
    rawdata=zeros(length(rawbin)/2,1);
    for
        i=1:length(rawbin)/2
            rawdata(i,1)=complex(rawbin(2*i-1),rawbin(2*i));
        end
    elseif
        strmatch(desc{indx+1},'REAL')==1
        rawdata=rawbin;
    end

```

% Build y axis

```

Indx = findstring(desc,'XPTS');
Dim = str2double(desc{indx+1});
Xmin = str2double(desc{indx+3});
Xrange = str2double(desc{indx+5});
Dx = xrange/(dim-1);
Datax = xmin:dx:xmin+(dim-1)*dx;

```

% Check for multidimensions

```

indx=findstring(desc,'ZTYP');

```

```

if
    strmatch(desc{indx+1},'IDX')==1
    % Needed to handle 3 dimensional data, not sure when this is going
    % to be necessary but just in case included this here.

```

```

    elseif
        strmatch(desc{indx-1},'IDX')==1
        dim=sqrt(length(rawdata));
        rawdat=zeros(dim,dim);
        for i=1:dim
            for j=1:dim
                rawdat(j,i)=rawdata(i+(j-1)*dim);
            end
        end

```

```

    end
    % Build second axis label
    indx=findstring(desc,'YPTS');
    dim=str2double(desc{indx+1});
    xmin=str2double(desc{indx+3});
    xrange=str2double(desc{indx+5});
    dx=xrange/(dim-1);
    datay=xmin:dx:xmin+(dim-1)*dx;
    data={datax',datay',rawdat};

```

```

elseif

```

```

    strmatch(desc{indx-3},'IDX')==1
    data={datax',rawdata}];
end

```

% Used to parse the .DSC file

```

function indx = findstring(tab,str)
for
    indx=1:length(tab)
    matches = strfind(tab{indx},str);
    if(~isempty(matches))
        return;
    end;
end;
    indx=0;
return;

```

% Phases the ESEEM

```

function spec = esephase(spec)
    % Phases and normalizes Bruker styled ESEEM time data
    data=spec{2};
    pa=angle(data);
    % Average phase weighted by amplitude
    ap=((pa'+pi)*abs(data))/sum(abs(data))-pi;
    Z = data.*exp(-1i*ap); % Adjust the phase
    % Normalize per shot
    spec{2}=complex(real(Z)/(N*H),imag(Z)/(H*N));
return

```

Appendix A.2

```
function [T2data]=T2_fit(spectra,reference,reference2,exppar)

% The inputs spectra, reference, and exppar are generated using
% the m-file setup_T2_fitting
% This routine prepares the experimental data and passes the
% results to the various fitting routines.

% Prompt for input of the reference temperature and the number
% of points desired to be truncated
prompt = {'Reference Temperature:', 'Number of Points to Truncate:',
         'Number of Points to Truncate:'};
dlgtitle = 'Required Input';
def = {'10','15','0'};
answer = inputdlg(prompt,dlgtitle,1,def);
reftemp=str2double(answer(1));

% Truncate the front
trunc = str2double(answer(2));
% Truncate the back
truncb = str2double(answer(3));
% Fix exppar to include the truncated points
% Fix the number of time points
exppar(1)= exppar(1)-trunc-truncb;
% fix the start time
exppar(3)= exppar(3)+exppar(2)*trunc;

% Define the time vector
time=exppar(3):exppar(2):exppar(3+exppar(2)*exppar(1)-exppar(2));

% Sort by temperature as this ordering varies by system
spectra = sortrows(spectra,2);

% Define the temperature vector
T = cell2mat(spectra(:,2));

% Preallocate various arrays
expdata=zeros(size(spectra{1,4},1)-trunc-truncb,size(spectra,1));
expdatawithBKG = zeros(size(spectra{1,4},1)-trunc-
                       truncb,size(spectra,1));
noise=zeros(size(spectra{1,4},1)-trunc-truncb,size(spectra,1));
rms = zeros(size(spectra,1),1);

% Generate a vector of 1/T1 values in units of KHz
% Heme protein from reference
```

```

% If you want to use a different T1, you have to do it here
R1(1,:) = 0.0000221 * T.^6.64;
refR1(1) = 0.0000221 * reftemp^6.64;

%% Setup the reference
% Phase the reference spectrum and temporarily store in data
% Reference to account for ESEEM and "other" decays

ref1 = esephase(reference{1,2}(1+trunc:size(reference{1,2},1)-truncb));
ref1 = data/(reference{5}*reference{6});

% ref2 is the background contribution to the decay and modulation
% approximate equation generated using Qtiplot
ref2 = esephase(reference2{1,2}(1+trunc:size(reference{1,2},1)-truncb));
BKG = ref2/(reference2{5}*reference2{6});

% Temperature dependence of background amplitude
amp = @(k)(55/7000)*(939.8/k+31258.68/k^2-84843/k^3);

% Combine the two components to produce the reference and rescale
ref = (ref1 - BKG * amp(reftemp));

%% Pull the experimental data from the input cell and stores in expdata
for
    i = 1:size(spectra,1)
        % First it is necessary to phase and normalize
        data = esephase(spectra{i,4}(1+trunc:size(spectra{i,4},1)-truncb));
        data = data/(spectra{i,5}*spectra{i,6});
        expdatawithBKG(:,i) = (data);
        % Account for the background contribution to the intensity
        % Data is stored columnwise in expdata after correction for
        % background contribution
        expdata(:,i) = (data - ref2 * amp(T(i)));
        % Calculate the noise
        noise(:,i) = imag(data);
        % Calculate the rms of the noise for later use
        rms(i) = sqrt(sum(noise(:,i).^2)/expvar(1));
    end

T2data.reference = ref;
T2data.expdata = expdata;
T2data.expdatawithBKG = expdatawithBKG;
T2data.rms = rms;

```

```

T2data.R1=R1;
T2data.refR1=refR1;

T2data.exppar=exppar;
T2data.time = exppar(3,1):exppar(2,1):exppar(3,1)+exppar(2,1)*(exppar(1,1)-1);
assignin('base','T2data',T2data);

```

function

```

spec = esephase(data)
% Calculate the phase angle by maximizing the real part
pfun=@(pa)(-sum((imag(data)*sin(pa)+real(data)*cos(pa))));
ap = fminbnd(pfun,0,2*pi);
% Apply the phase shift to the data
Z = data.*exp(-1i*ap);
spec=Z;

```

return

Appendix A.3

```

function [residualmap, cellresidual, Ph]=resmap_2center(T2data)

```

```

% The inputs spectra, reference, and exppar are generated using
% the m-file setup_T2_fitting
% Experimental data fit the model:
% fit(T,r)=(ref.*((1-a)+a*Et_T(r))./((1-a)+a*Et_ref(r)));
% This routine generates a grid of a and r values and calculates
% the residuals at each point and sums over the temperature
% Adjusted to use MakeDecay.m rather than T2_decay.m

```

```

% Pull in variables and setup constants
% Pull relevant information from T2data structure
ref=T2data.reference;
expdata=T2data.expdata;

```

```

R1=T2data.R1;
refR1=T2data.refR1;
exppar=T2data.exppar;

```

```

% Using a spiral, enables to use a single value for the angles
% need minimum 500 points for non-isotropic g
simpar=180*5;

```

```

% If using two distances this enables to use two different T1's.

```

```

if
length(refR1)>1
refR1a=refR1(1);

```

```

R1a=R1(1,:);
refR1b=refR1(2);
R1b=R1(2,:);
else
    refR1a=refR1;
    R1a=R1;
    refR1b=refR1;
    R1b=R1;
end

% Grid out the temperatures and distances
% Range to be calculated for r
% da - short range interaction
da=1:1:50;
% db - long range interaction
db=1:1:50;

tdgrida = cell(length(da),length(R1a));
drefa = cell(length(da));

dkFun = MakeDecay(exppar,simpar);

for
    i=1:length(da)
        % dkFun uses the parameters stored in the handles system and input
        % R1 and r values to calculate the decay, in this case the reference
        % decay
        Etr1=dkFun(refR1a(1), da(i));
        drefa{i}=Etr1;
        % loop over temperature
        for
            j=1:length(R1a)
                Et1 = dkFun(R1a(j), da(i));
                tdgrida{i,j}=Et1;
            end
        end

tdgridb = cell(length(db),length(R1b));
drefb = cell(length(db));

for
    i=1:length(db)
        % dkFun uses the parameters stored in the handles system and input
        % R1 and r values to calculate the decay, in this case the reference

```

```

% decay
Etr1=dkFun(refR1b(1), db(i));
drefb{i}=Etr1;
% loop over temperature
for
j=1:length(R1b)
Et1 = dkFun(R1b(j), db(i));
tdgridb{i,j}=Et1;
end
end

%% Calculate the residuals
Chisq = zeros(length(da),length(db));
Ph = cell(size(chisq));
% Loop of d1 - short range interaction
cellresidual=cell(size(chisq));
for
h=1:length(da)
% Loop over d2 - longrange interaction
for
i=1:length(db)
% Define start point [phc phd]
startpoint =sqrt[0.45 0.4];
model = @(parameters)Pfit(parameters,drefa,tdgrida,h,drefb,
tdgridb,i,ref,expdata);
estimates = LMFnlsql(model, startpont);
residuals = Pfit(estimates,drefa,tdgrida,h,drefb,
tdgridb,i,ref,expdata);
Ph{h,i} = estimates.^2;
cellresidual{h,i}= residuals(:);
% chi squared
chisq(h,i) = residuals(:)*residuals(:);
end
end

% Plot map, the chi-square map as a function of both distances
surfc(db/10,da/10,chisq)
xlabel('long range interaction')
ylabel('short range interaction')
residualmap{1,1} = db;
residualmap{1,2} = da;
residualmap{1,3} = chisq;
% assignin('base','Ph',Ph);

```

```

assignin('base','residuals',cellresidual);
assignin('base','residualmap',residualmap);

```

```

function resid=Pfit(parameters,drefa,tdgrida,h,drefb,tdgridb,i,ref,
    expdata)
Pha = parameters(1)^2;
Phb = parameters(2)^2;
Sbkg = ref./(((1-Pha)+Pha*drefa {h}).*((1-Phb)+Phb*drefb {i}));
% Loop over temperature
Resid = zeros(size(expdata));

for
    k = 1:size(expdata,2)
        fit= Sbkg.*((1-Pha)+Pha*tdgrida {h,k}).*
            ((1-Phb)+Phb*tdgridb {i,k});
        ss1 = real(fit)*real(fit);
        ss2 = real(expdata(:,k))*real(fit);
        amp = ss2/ss1;
        fittedcurve = amp*fit;
        residual = (fittedcurve-expdata(:,k));
        rms = sqrt(sum(imag(residual).^2)/length(residual));
        resid(:,k) = residual/rms;
    end
resid=real(resid(:));
return

```

Appendix A.4

```
% This routine generates the confidence interval values from the  
% residualmap.
```

```
d2 = residualmap{1,1};  
d1 = residualmap{1,2};  
residual = residualmap{1,3};  
minres = min(min(residual));
```

```
figure(4)  
conf = zeros(length(d1),length(d2));  
v = [((min(min(residual)))+6.17) ((min(min(residual)))+9.21)];  
contour(d2/10,d1/10,residual,v);
```

Appendix A.5

MakeDecay function

```

function [ Tm_decay ] = MakeDecay( expar, simpar )

% expar - Experimental parameters contains time values(ns),
% field (T) and frequency (GHz).
% simpar - Simulation parameters: N number of points on the spiral
% Returns Tm_Decay which is a function to calculate the dipolar decay
% function.
% Tm_decay (T1i, r)
% T1i - Inverse of T1 of the fast-relaxing spin in ms.
% r - distance between spin centers in Å.
% Returns a vector with the relaxation function for each value of tau
% This is a function that sets up the calculation of the phase memory
% decay due to modulation of the dipolar interaction between the
% (assumed isotropic) observed radical and a fast relaxing center with
% anisotropic g-factor.
% The formulae are based on Dzuba, Raitsimring and Salikhov.
% The relaxation is integrated over a sphere by summing at points
% lying on a spiral on the unit hemisphere.
% Both spins must have S=1/2.
% N can be small if g of the fast-relaxing spin is isotropic.
% These functions are optimized for least squares fitting of
% experimental data taken at multiple temperatures under
% identical conditions.
% Included E.D.Saff spiral of evenly spaced theta and phi orientations

% Define variables that are the same for an entire set of
% calculations.
% Persistent N Ntau tau theta ct st phi cp sp Ar3 ; %
% Get parameters from expar

Ntau = expar( 1, 1 ); % number of time points
Tinc = expar( 2, 1 ); % time increment (ns)
Ts = expar( 3, 1 ); % starting tau value (ns)
B0 = expar( 4, 1 ); % Field of measurement (T)
Freq = expar( 5, 1 ); % measuring frequency (GHz)

% Get parameters from simpar
N = simpar(1); % number of points on spiral

% Calculate theta and phi for the N points (orientations on the spiral
% on the unit hemisphere at which to calculate relaxation; then
% calculate the sin and cos of theta and phi

```

```

[theta phi] = Spiral( N );
ct = cos( theta );
st = sin( theta );
cp = cos( phi );
sp = sin( phi );

% Calculate vector of 2*tau values;
taud = 2* (Ts : Tinc : Ts + Tinc*(Ntau-1));

% Various intermediate parameters

ge = 714.48 * Freq/B0; % effective g value at observation
Dc = 81.557; % dipolar/g^2 at 1 Angstrom in GHz radians
if
    size( expar, 2 ) == 1
        % isotropic g same as observed spin
        % the dipolar splitting matrix; needs to be divided by r^3
        g2 = ge * ge;
        aar3 = g2 * Dc/2.*[-1. 0. 0.; 0. -1. 0.; 0. 0. 2. ];
    else
        % Anisotropic g get g principal values
        gx = expar( 1, 2 );
        gy = expar( 2, 2 );
        gz = expar( 3, 2 );

        if
            size( expar, 2 ) == 2
                % Slight g anisotropy, use Maryasov average
                g2 = gx*gx + gy*gy + gz*gz;
                gmav = sqrt( g2 / 3 );
                % the dipolar splitting matrix;
                % needs to be divided by r^3
                aar3 = ge*gmav*Dc/2.*[-1. 0. 0.; 0. -1. 0.; 0. 0. 2. ];
            else
                % use full g matrix, but first load the Euler angles and
                % rotate g matrix into dipolar frame
                % diagonal g^2 matrix
                g2d = [gx*gx 0 0; 0 gy*gy 0; 0 0 gz*gz];
                % Euler angle alpha
                euA = expar( 1, 3 );
                euB = expar( 2, 3 );
                euC = expar( 3, 3 );
            end
        end
    end

```

```

% Rotation Matrices: about z, then y', then z''
rA = [cos(euA) sin(euA) 0.;
      -sin(euA) cos(euA) 0.;
       0.      0.      1.];
rB = [cos(euB) 0.      -sin(euB);
      0.      1.      0.;
      sin(euB) 0.      cos(euB)];
rC = [cos(euC) sin(euC) 0.;
      -sin(euC) cos(euC) 0.;
       0.      0.      1.];

% g^2 rotated into dipolar frame
g2 = rC*rB*rA*g2d*rA'*rB'*rC';
% the dipolar splitting matrix;
% needs to be divided by r^3
aar3 = ge*g2*Dc/2.*[-1. 0. 0.; 0. -1. 0.; 0. 0. 2.];

end    % anisotropic g
end    % aar3 calculation

% Set up and pre-allocate vectors for D*r^3 and D^2*r^6

Dr3 = zeros( N, 1 );

for
    i = 1 : N      % Can't seem to vectorize
    Tr = [ cp(i)*st(i) sp(i)*st(i) ct(i) ];
    if
        size( expar, 2 ) == 3
        Dr3(i) = (Tr * aar3 * Tr') / sqrt( Tr * g2 * Tr' );
    else
        Dr3(i) = (Tr * aar3 * Tr');
    end
end

%*****
% Initialization is over, so return the function handle that will
% then calculate the relaxation function for a given distance and T1;
% NB: it is vital not to alter any of the persistent values defined
% above
%*****

```

```

Tm_decay = @DecayFun;

function [Et, time] = DecayFun( T1i, r )

% T1i - Inverse of T1 (1/T1 or R1) of the fast-relaxing spin in ms
% r - distance between spin centers in Angstrom
% Returns a vector with the relaxation function for each value of tau

% calculate spin flip rate in GHz
W = T1i/2. *10^(-6);
Wsqr = W * W;

% Make local vectors
D = Dr3 / r^3;
Dsqr = D.* D;
ew = exp( -W * taud );

% Get indices of R^2 positive, negative and zero
inR = ( Wsqr > Dsqr );
inI = ( Wsqr < Dsqr );
inZ = ( Wsqr == Dsqr );

Etr = zeros( 1, Ntau );
DRsqr = Dsqr ( inR );
if
    isempty ( DRsqr ) == 0 % Some R^2 > 0
    Rsqr = Wsqr - DRsqr; % Always positive
    Rreal = sqrt( Rsqr );
    % Build result
    Etr = -sum( DRsqr ./ Rsqr ) .* ew;
    Etr = Etr +...
        W/2*(((W-Rreal)./Rsqr)*exp(-(W+Rreal)*taud) +...
            ((W+Rreal)./Rsqr)' * exp( -(W-Rreal) * taud ) );
end

% Tidy up and remove temp vectors
clear DRsqr Rsqr Rreal;

Eti = zeros( 1, Ntau );
DIIsqr = Dsqr ( inI );

if
    isempty ( DIIsqr ) == 0 % Some R^2 < 0
    Rsqr = DIIsqr - Wsqr; %Should be positive as calculated
    Rimag = sqrt( Rsqr ); % So this is real (-i*sqrt

```

```

% Build result
Eti = sum( DIsq ./ Rsq ); % Rsq is actually -R^2
Eti = Eti +...
    W * ((Rimag./Rsq)' * sin( Rimag * taud ) -...
        (W./Rsq)' * cos( Rimag * taud ) );
Eti = Eti.* ew;
end

% Cleanup
clear Disq Rsq Rimag;

Etz = zeros( 1, Ntau );
L = length( Dsq(inZ) );

if
    L == 0 % Some R^2 == 0
    Etz = L * ew.* (1 + W*taud + (Wsq/2)*taud.*taud);
end

Et = ((Etr + Eti + Etz) / N)'; % normalized
time = taud/2';

% Claenup
clear Etr Eti Etz;
end % end of DecayFun
end % end of Makedecay

```